Beyond imaging with coherent anti-Stokes Raman scattering microscopy

Thèse

Steve Bégin

Doctorat en physique
Philosophiæ doctor (Ph.D.)

Québec, Canada

Résumé

La microscopie optique permet de visualiser des échantillons biologiques avec une bonne sensibilité et une résolution spatiale élevée tout en interférant peu avec les échantillons. La microscopie par diffusion Raman cohérente (CARS) est une technique de microscopie non linéaire basée sur l'effet Raman qui a comme avantage de fournir un mécanisme de contraste endogène sensible aux vibrations moléculaires. La microscopie CARS est maintenant une modalité d'imagerie reconnue, en particulier pour les expériences *in vivo*, car elle élimine la nécessité d'utiliser des agents de contraste exogènes, et donc les problèmes liés à leur distribution, spécificité et caractère invasif. Cependant, il existe encore plusieurs obstacles à l'adoption à grande échelle de la microscopie CARS en biologie et en médecine : le coût et la complexité des systèmes actuels, les difficultés d'utilisation et d'entretient, la rigidité du mécanisme de contraste, la vitesse de syntonisation limitée et le faible nombre de méthodes d'analyse d'image adaptées.

Cette thèse de doctorat vise à aller au-delà de certaines des limites actuelles de l'imagerie CARS dans l'espoir que cela encourage son adoption par un public plus large. Tout d'abord, nous avons introduit un nouveau système d'imagerie spectrale CARS ayant une vitesse de syntonisation de longueur d'onde beaucoup plus rapide que les autres techniques similaires. Ce système est basé sur un laser à fibre picoseconde synchronisé qui est à la fois robuste et portable. Il peut accéder à des lignes de vibration Raman sur une plage importante (2700–2950 cm^{-1}) à des taux allant jusqu'à 10 000 points spectrales par seconde. Il est parfaitement adapté pour l'acquisition d'images spectrales dans les tissus épais. En second lieu, nous avons proposé une nouvelle méthode d'analyse d'images pour l'évaluation de la structure de la myéline dans des images de sections longitudinales de moelle épinière. Nous avons introduit un indicateur quantitatif sensible à l'organisation de la myéline et démontré comment il pourrait être utilisé pour étudier certaines pathologies. Enfin, nous avons développé une méthode automatisé pour la segmentation d'axones myélinisés dans des images CARS de coupes transversales de tissu nerveux. Cette méthode a été utilisée pour extraire des informations morphologique des fibres nerveuses dans des images CARS de grande échelle.

Abstract

Optical-based microscopy techniques can sample biological specimens using many contrast mechanisms providing good sensitivity and high spatial resolution while minimally interfering with the samples. Coherent anti-Stokes Raman scattering (CARS) microscopy is a nonlinear microscopy technique based on the Raman effect. It shares common characteristics of other optical microscopy modalities with the added benefit of providing an endogenous contrast mechanism sensitive to molecular vibrations. CARS is now recognized as a great imaging modality, especially for *in vivo* experiments since it eliminates the need for exogenous contrast agents, and hence problems related to the delivery, specificity, and invasiveness of those markers. However, there are still several obstacles preventing the wide-scale adoption of CARS in biology and medicine: cost and complexity of current systems as well as difficulty to operate and maintain them, lack of flexibility of the contrast mechanism, low tuning speed and finally, poor accessibility to adapted image analysis methods.

This doctoral thesis strives to move beyond some of the current limitations of CARS imaging in the hope that it might encourage a wider adoption of CARS as a microscopy technique. First, we introduced a new CARS spectral imaging system with vibrational tuning speed many orders of magnitude faster than other narrowband techniques. The system presented in this original contribution is based on a synchronized picosecond fibre laser that is both robust and portable. It can access Raman lines over a significant portion of the high-wavenumber region (2700–2950 cm^{-1}) at rates of up to 10,000 spectral points per second and is perfectly suitable for the acquisition of CARS spectral images in thick tissue. Secondly, we proposed a new image analysis method for the assessment of myelin health in images of longitudinal sections of spinal cord. We introduced a metric sensitive to the organization/disorganization of the myelin structure and showed how it could be used to study pathologies such as multiple sclerosis. Finally, we have developped a fully automated segmentation method specifically designed for CARS images of transverse cross sections of nerve tissue. We used our method to extract nerve fibre morphology information from large scale CARS images.

Contents

List of Tables

List of Figures

~~*A mon amour!*~~
~~*A mes deux amours!*~~
A mes trois amours!
...
(Ca fait trop longtemps que je suis aux études)

It ends tonight.

— Neo

Remerciements

Pour commencer, je voudrais remercier mon fantastique directeur de thèse le professeur Daniel Cote avec qui j'ai eu l'honneur de travailler pendant toute ces années.

Je tiens aussi à dire un gros merci à tout les membres du groupe avec qui j'ai eu un plaisir immense a collaborer.

Finalement, un merci tout special à l'amour de ma vie pour tout le support et l'inspiration qu'elle a su m'apporter pendant toutes ces années.

Avant-propos

Cette thèse de doctorat comporte trois articles scientifiques publiés dans deux revues renommées ainsi qu'un quatrième soumis pour publication. Les travaux présentés dans ces articles ont été réalisés entièrement lors de mes études de doctorat en physique au Centre de recherche de l'Institut universitaire en santé mentale de Québec (CRIUSMQ) sous la supervision du professeur Daniel Côté. Nous allons, dans cette section, spécifier l'apport de travail que j'ai effectué pour chacun de ces articles.

Voici la liste des articles découlants de cette thèse :

1. **Bégin, S.**, Bélanger, E., Laffray, S., Vallée, R., and Côté, D. C. (2009). In vivo optical monitoring of tissue pathologies and diseases with vibrational contrast. Journal of Biophotonics, 2(11), 632–642
2. **Bégin, S.**, Burgoyne, B., Mercier, V., Villeneuve, A., Vallée, R., and Côté, D. C. (2011). Coherent anti-Stokes Raman scattering hyperspectral tissue imaging with a wavelength-swept system. Biomedical Optics Express, 2(5), 1296-1306.
3. **Bégin, S.**, Bélanger, E., Laffray, S., Aubé, B., Chamma, E., Bélisle, J., Lacroix, S., De Koninck, Y. and Côté, D. C. (2013). Local assessment of myelin health in a multiple sclerosis mouse model using a 2D Fourier transform approach. Biomedical Optics Express, 4(10), 2003–2014.
4. **Bégin, S**, Dupont-Therrien, O., Bélanger, E., Daradich, A., Laffray, S., De Koninck, Y. and Côté, D. C. (2014). Automated method for the segmentation and morphometry of nerve fibres in large scale CARS images of spinal cord tissue. Biomedical Optics Express, 5(12), 4145-4161.

Tout d'abord, la première publication présentée dans cette thèse (chapitre 2) est un article de revue publié en 2009 dans le *Journal of Biophotonics*. L'objectif premier de cet article est de dresser un état des lieux sur les techniques de microscopie *in vivo* peu envahissantes basées sur l'effet Raman. En particulier, ce manuscrit traite des applications en imagerie et en spectroscopie dans le but d'observer les tissus vivants dans le cadre de blessures ou de maladies. En tant qu'auteur principal, j'ai fait la revue de la littérature et effectué la rédaction de l'article. La contribution principale de mes collègues se trouve au niveau de la révision

à l'exception de E. Bélanger qui a aussi contribué aux figures à partir de ses travaux de recherche et rédigé la version préliminaire de la section couvrant les applications de l'imagerie CARS au domaine biomédical. L'excellence de notre travail a été remarqué par le comité de rédaction et cet article fut mentionné dans la rubrique *Editor's Choice*. Finalement, l'insertion de cet article comme second chapitre de ma thèse lui confère le rôle de revue de la littérature en lien avec mon projet de recherche.

L'article suivant, présenté au chapitre 3, a été publié dans le journal *Biomedical Optics Express* en 2011. Cet article est le fruit d'un partenariat très étroit avec la compagnie *Genia Photonics*. J'ai participé à la conception d'un nouveau système laser et collaboré de façon constante avec mes collègues de Genia Photonics (B. Burgoyne, V. Mercier et A. Villeneuve) au développement et au raffinement de notre prototype. J'ai aussi fait le développement complet du système de microscopie, élaboré le système d'acquisition et réalisé toutes les expériences menant à la publication de l'article. Finalement, j'ai effectué la rédaction de l'article. Ces travaux ont conduit au développement et à la commercialisation d'un nouveau système de lasers à fibre pour la microscopie et la spectroscopie CARS ainsi qu'à l'obtention d'un brevet (Villeneuve, A. ; Burgoyne, B. ; Côté, D. ; **Bégin, S.** Spectrometer. U.S. Patent 8,625,091, January 7, 2014.). Le professeur R. Vallée a participé à la révision du manuscrit.

L'article présenté au chapitre 4 a été publié dans le journal *Biomedical Optics Express* en 2013. Cette publication est le résultat d'une collaboration entre plusieurs membres du groupe Côté dans le cadre d'un projet relatif à l'étude de la sclérose en plaque. Les travaux qui y sont présentés portent sur une nouvelle méthode d'analyse d'image visant à mesurer localement l'organisation des axones myélinisés dans la moelle épinière. Les expériences de laboratoire ont été effectué par E. Bélanger, S. Laffray, B. Aubé et E. Chamma. Pour ma part, j'ai développé la totalité de la méthode d'analyse a l'exception de l'algorithme permettant de passer d'un volume 3D à une image 2D qui a été développé par J. Bélisle. J'ai aussi effectué tout le travail d'analyse ainsi que l'écriture de l'article. Les professeurs S. Lacroix et Y. De Koninck ont participé au niveau de la révision de l'article.

Finalement, le chapitre 5 présente un article qui a été publié dans le journal *Biomedical Optics Express* en 2014. Les travaux qui y sont présentés portent sur une méthode d'analyse d'image ayant pour but la segmentation automatique de fibres nerveuses dans des images CARS de moelle épinière en coupe transverse. J'ai dévelopé la totalité de la technique d'analyse et analysé l'ensemble du jeu de données d'images. O. Dupont-Therrien a collaboré surtout au niveau conceptuel par d'innombrables discussions et de façon plus concrète au developpement de certaines routines d'analyse. Les expériences de laboratoire on été réalisé par E. Bélanger, S. Laffray et A. Daradich. Le professeur Y. De Koninck a participé au niveau de la révision de l'article.

Chapter 1

Introduction

1.1 Principles and applications of coherent anti-Stokes Raman scattering

Ask the right questions, and nature will open the doors to her secrets.

— Sir Chandrasekhara Venkata Raman

In a digital image, contrast generally refers to the difference in grey level that makes the representation of an object distinguishable. In microscopy, contrast also refers to a mechanism by which an image is created and an object of interest (molecule, cell, etc.) distinguished from others. Optical microscopy relies on a large variety of contrast mechanisms such as reflectance, fluorescence, and vibrational contrast in order to see different things. Vibrational contrast offers intrinsic chemical selectivity based on the vibrational frequencies of the molecules already present in the samples under study. This can be achieved through infrared spectroscopy (absorption), Raman spectroscopy (inelastic scattering) or several derived techniques. While all these techniques have their merits (and limitations), this section will focus on a technique derived from spontaneous Raman scattering: coherent anti-Stokes Raman scattering (CARS). It will outline the basic concepts of CARS imaging and spectroscopy necessary to understand the four chapters that make use of CARS microscopy.

1.1.1 Spontaneous Raman scattering

The Raman effect is a form of scattering where a photon interacts with a molecule by exciting it from some initial energy state to a virtual state. The molecule relaxes back from the virtual state to a different rotational or vibrational state and emits a photon whose wavelength is shifted compared to the initial photon. A Stokes shift occurs when the photon leaves some energy behind and an anti-Stokes shift when the emitted photon takes some energy from the molecule. The processes are illustrated in Fig. 1.1 a). The Raman shift (Ω), usually reported

in wavenumber (cm^{-1}), is related to the initial (λ_0) and final (λ_1) photon wavelength by the following relationship:

$$\Omega = (\frac{1}{\lambda_0} - \frac{1}{\lambda_1}) \tag{1.1}$$

Used as a probe, the Raman effect is useful since it provides information specific to the vibrations of the molecular bonds under study. Careful examination of a Raman spectra can lead to the identification of species present in a sampled volume. It is this amazing ability for intrinsic chemical specificity that made Raman spectroscopy such a widely used technique. For instance, Fig. 1.1 b) shows a collection of Raman spectra from a live cell acquired with a confocal microscope [Puppels et al., 1990].

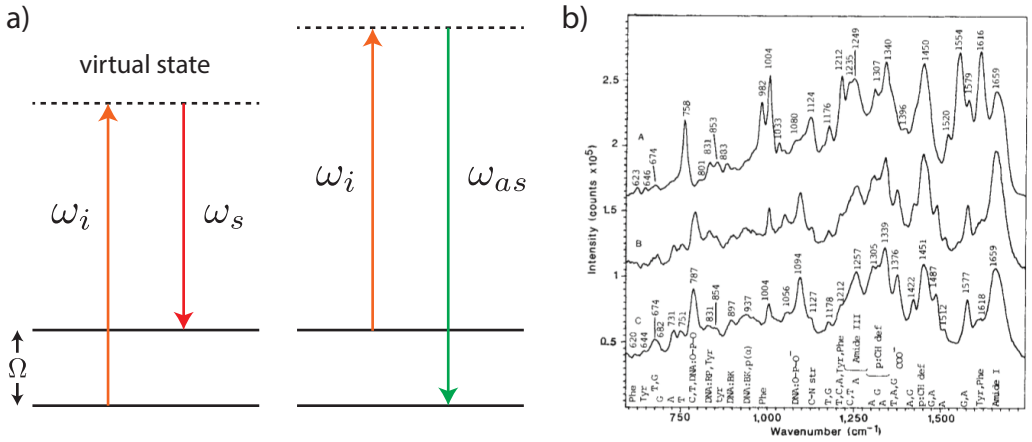

Figure 1.1 – a) Spontaneous Raman energy diagram. The inelastic scattering of incident radiation (ω_s) results in either (left) red-shifted emission (ω_s) or (right) blue-shifted emission (ω_{as}). b) Example of Raman spectra from a live cell showing the wealth of molecular information in the vibrational spectrum [Puppels et al., 1990].

Yet, despite its unique capabilities, spontaneous Raman is also fundamentally limited. The Raman effect as an optical effect is extremely weak, with photon conversion efficiencies typically ranging from 10^{-7} to 10^{-15} in tissue [Tuchin, 2007]. Moreover, it is often plagued by the overwhelming fluorescence background from the samples. Therefore, it necessitates high laser power (typically > 100 mW), long integration times of 100 ms to 1 s per pixel, and a significant amount of post-processing [van Manen et al., 2005].

1.1.2 CARS microscopy

Coherent anti-Stokes Raman scattering can be used to obtain much stronger signals while retaining the same chemical selectivity. First reported in 1965 [Maker and Terhune, 1965], CARS was later introduced as a contrast mechanism for microscopy [Duncan et al., 1982]

and is now recognized as a great imaging modality, especially for *in vivo* experiments. Here is a quick summary of its many advantages:

1. There is no need for exogenous contrast agent since the signal comes from the molecular vibrations of the sample.
2. CARS is more sensitive than spontaneous Raman scattering by orders of magnitude, enough to permit video-rate imaging [Evans et al., 2005].
3. Intrinsic three-dimensional capability from the nonlinear nature of the process [Zumbusch et al., 1999a].
4. The anti-Stokes signal is blue-shifted with respect to the excitation lasers, away from the presence of one-photon autofluorescence.
5. Penetration depth of up to $\sim$ 400 μm with the use of near-infrared excitation wavelengths

Signal generation

The CARS signal is generated by the nonlinear interaction of two or three laser beams with a sample via a four-wave-mixing process (Fig. 1.2 a)). It involves three incident laser pulses at the pump (ω_p), Stokes (ω_s), and probe ($\omega_{p\prime}$) frequencies, interacting simultaneously with the sample. We note that in practice, the pump and probe beams are usually supplied by the same laser beam and will be referred to as the pump beam for simplicity. When the difference between the frequency of the pump beam (ω_p) and the Stokes beam (ω_s) matches the frequency of a Raman active molecular line, a strong anti-Stokes signal is generated at $\omega_{as} = 2\omega_p - \omega_s$ in a direction determined by the phase-matching conditions (Fig. 1.2 b)). As well, the oscillators are coherently driven by the excitation fields, providing a signal that can be orders of magnitude stronger ($\sim 10^5$) than signals from spontaneous Raman scattering [Tolles et al., 1977a].

The anti-Stokes field, comes from the coherent superposition of the microscopic dipoles driven by the pump (E_p) and Stokes (E_s) fields, generating the macroscopic third-order polarisation ($P^{(3)}(\omega_{as}) \propto \chi^{(3)} E_p^2 E_s$) at the anti-Stokes frequency. The proportionality constant $\chi^{(3)}$ is the complex nonlinear optical susceptibility of the material. From this equation, the anti-Stokes signal intensity can be derived [Tolles et al., 1977a],

$$I_{as} = \left(\frac{4\pi^2 \omega_{as}}{n_{as} c^2}\right) |3\chi^{(3)}|^2 I_p^2 I_s z^2 \left(\frac{sin(\Delta k\, z/2)}{(\Delta k\, z/2)}\right)^2 \tag{1.2}$$

where I are the laser intensities, $\Delta k = |\vec{k_{as}} - (2\vec{k_p} - \vec{k_s})|$ is the wavevector mismatch and z is the length over which the beams are mixed through the sample. $k_i = 2\pi/\lambda_i$ is known as the wavevector.

Close examination of equation 1.2 reveals some key characteristics of the CARS signal. First, the nonlinear intensity dependence grants the CARS signal intrinsic three-dimensional sectioning. The anti-Stokes signal is proportional to the square of the number of vibrational oscillators since it depends on $|\chi^{(3)}|^2$. The phase matching condition is realised when Δk is close to zero which maximizes conversion efficiency (the sinc function) for a length of path z. For low-pressure medium (gases), this is readily achieved over moderate path length, but in condensed media (*e.g.* biological sample), the phase matching is achieved if the beams ($\vec{k_p}$ and $\vec{k_s}$) are crossed at the phase matching angle θ (Fig. 1.2 b)). Then, the anti-Stokes signal is generated in the forward or backward (epi) directions. The first demonstration of CARS as a contrast mechanism for microscopy used a configuration where the laser beams were non-collinear [Duncan et al., 1982]. This microscope, however, was extremely difficult to align, had a poor spatial resolution and a low sensibility. Many years later, Zumbusch et al. [1999a] realised that by utilising a high numerical aperture microscope objective (NA > 0.6), the phase matching condition was relaxed, enabling the use of a regular scanning microscope configuration with collinear beams.

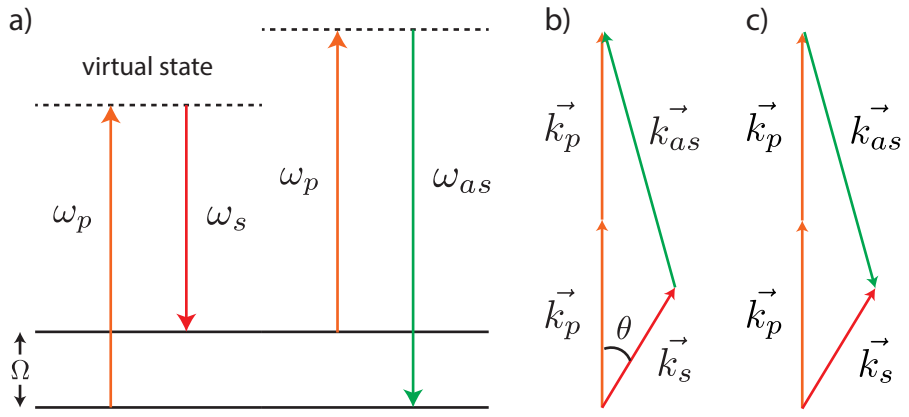

Figure 1.2 – a) CARS energy diagram. The anti-Stokes signal (ω_{as}) is generated by the nonlinear interaction of a pump (ω_p) and a Stokes (ω_s) field with a Raman active molecular vibration (Ω). Phase matching condition for b) forward-generated and c) backward-generated CARS is achieved if the beams ($\vec{k_p}$ and $\vec{k_s}$) are crossed at the phase matching angle θ.

Nonlinear optical susceptibility

The complex nonlinear optical susceptibility has two terms, a non-resonant ($\chi^{(3)}_{NR}$) and a resonant ($\chi^{(3)}_{R}$) component:

$$\chi^{(3)} = \chi^{(3)}_{NR} + \frac{\chi^{(3)}_{R}}{\Delta - i\Gamma} \tag{1.3}$$

where the detuning parameter ($\Delta = \omega_p - \omega_s - \Omega$) depends on the centre frequency (Ω) of

a Raman line with bandwidth Γ. equation 1.3 implies that when the frequency difference between the pump and the Stokes fields coincides with the frequency of a molecular vibration of the sample ($\Delta = 0$), the CARS signal is strongly enhanced. As the CARS intensity is proportional to $|\chi^{(3)}|^2$, the intensity of the anti-Stokes signal can be written as:

$$I_{as}(\Delta) \propto |\chi^{(3)}_{NR}|^2 + |\chi^{(3)}_{R}(\Delta)|^2 + 2\chi^{(3)}_{NR}\, Re\, \chi^{(3)}_{R}(\Delta) \tag{1.4}$$

where where $Re\,\chi^{(3)}_R$ is the real part of resonant term of $\chi^{(3)}$. The first term of equation 1.4 is independent of the Raman shift, which implies that multiple coherently additive contributions to $\chi^{(3)}$ can lead to the resonant contribution being masked by other non-resonant contributions. As well, the nonresonant contribution introduces an offset that gives CARS microscopy images a background. The second term contains only resonant information. The third term represents a mixed contribution which leads to a spectral redshift of the maximum CARS response and a negative dip at the blue end of the spectral line. All contributions are plotted independently as a function of the detuning parameters in Fig. 1.3 a) and together in Fig. 1.3 b).

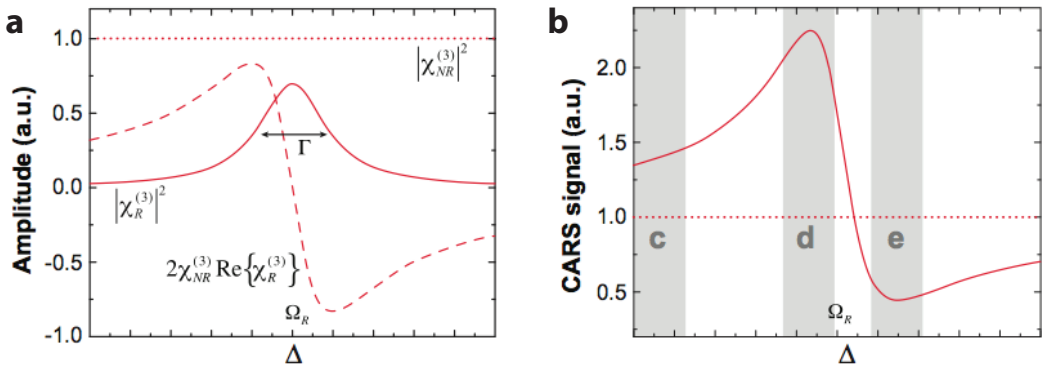

Figure 1.3 – a) Three contribution from the $|\chi^{(3)}|^2$ to the CARS signal as a function of the detuning parameter Δ. The purely resonant term (solid line), the nonresonant background term (dotted line), and the mixing term (dashed line). b) The total CARS signal (solid line) with nonresonant background contribution (dotted line). The region highlighted in **c** shows the presence of a nonresonant signal off resonance. While the regions in **d** and **e** indicate the redshift and blue dip respectively. Figure from [Evans and Xie, 2008].

Radiation pattern

The radiation pattern of the CARS signal comes from the coherent addition of the radiation from an ensemble of coherently induced Hertzian dipoles. It depends mainly on four parameters: 1) the size and 2) shape of scatterers, 3) the local environment, and 4) the nature of the oscillators (their nonlinear susceptibilities) [Cheng et al., 2002c]. A single oscillating dipole generates signals equally in both the forward and epi-direction (Fig. 1.4 a)) and a

plane of dipoles will generate a similar but more directional pattern from the coherent addition of the dipole intensities (Fig. 1.4 b)). As the sample thickens, constructive interference happens in the forward direction and destructive interference happens in the backward direction (Fig. 1.4 c)) until no epi-CARS signal is generated when many dipoles populate the focal spot (Fig. 1.4 d)).

This would seem to be a major problem for microscopy experiments involving thick tissue where the CARS signal would be generated in the forward direction only, away from detectors. Fortunately, a useful epi-directed CARS signal has been reported [Cheng et al., 2001b] and three mechanisms have been identified to explain its existence. With the first one, objects smaller than $\lambda_p/3$ will generate an epi-CARS signal due to incomplete destructive interference [Volkmer et al., 2001]. Secondly, sharp discontinuities in $\chi^{(3)}$ will act as infinitely small objects and generate a backward-propagating anti-Stokes signal [Cheng et al., 2002c]. Finally, with the third and most useful (at least in thick tissue) mechanism, the photons that are initially forward-propagating are redirected in the backward direction by multiple scattering events (Fig. 1.4 e)) [Evans et al., 2005]. Turbid samples containing many local changes in their index of refraction (most biological tissues), make this process particularly efficient.

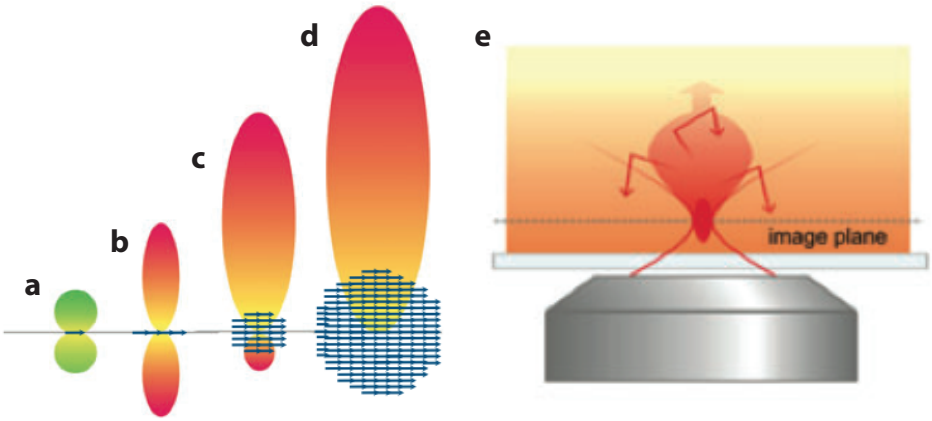

Figure 1.4 – CARS radiation pattern as a function of scatterer size. a) A single oscillating dipole generates equal signal in both forward and epi-direction. b) A single plane of dipoles generates a similar but more directed pattern from the coherent addition of all dipole contributions. c) Destructive interference weakens the epi-directed signal in thicker samples until d) only a strong forward signal is generated. e) Turbid material will efficiently redirect the forward-generated CARS signal back towards the objective. Figure adapted from [Evans and Xie, 2008].

Light sources

The development of new laser light sources has greatly helped progress in CARS microscopy, especially the introduction of picosecond tunable pulsed laser systems operating in the near infrared (NIR).

NIR sources have many advantages for CARS microscopy. First, they help minimize the nonresonant contribution to the CARS signal, which happens when the pump wavelength is near the peak of a two-photon resonance. By minimizing these two-photon interactions, NIR sources help provide images with better signal-to-noise ratios. As well, the penetration depth of CARS microscopy is generally limited by scattering which is very important in biological tissue samples. Because the CARS signal has a nonlinear intensity dependence, scattering in the sample leads to a loss of laser intensity as well as an increase in focal spot size [Beaurepaire et al., 2001]. By minimizing scattering, NIR sources help alleviate this problem. Finally, NIR sources also minimize multiphoton absorption-induced photodamage, one of the main source of sample damage [Fu et al., 2006]. However, NIR sources also have two non-negligible drawbacks. The first is their lower spatial resolution, on the order of 350 nm. Secondly, the anti-Stokes signal, generated at wavelengths higher than the excitation beams, can be difficult to acquire with standard detectors.

Because of the nonlinear nature of the CARS process, pulsed laser system are an essential part of the CARS arsenal. But what is the effect of pulse duration on the signal generation? Since CARS is a nonlinear process, it would be tempting to think that shorter is better. As it happens, the answer is slightly more complex. On one hand, the intensity of the anti-Stokes signal depends on the term $I_p^2 I_s$ (equation 1.2) meaning that shorter pulses will generate a stronger CARS signal. On the other hand, the resonant term of the nonlinear optical susceptibility depends on the detuning parameter (Δ) and the Raman linewidth (Γ) (equation 1.3). Since lasers do not have infinitely thin linewidth, there is some amount of detuning even for a perfect combination of excitation wavelength (in terms of wavelength difference). For example, a transform-limited 100 fs pulse in the near-infrared has a spectral width of about 150 cm^{-1} while a 7 ps pulse of the same wavelength has a spectral width of about 2 cm^{-1}. As well, typical Raman linewidths are on the order of 10 to 20 cm^{-1} in the fingerprint region (500–2000 cm^{-1}) and several tens of cm^{-1} in the high-wavenumber region (2400–3800 cm^{-1}). Therefore, femtosecond (fs) pulses are generally ill suited for the excitation of narrow Raman lines since only a fraction of their spectral components can be used for the resonant signal generation, while all components are involved in the nonresonant signal generation. This can lead to an overwhelming nonresonant background. In that sense, picosecond (ps) sources offer more versatility since their linewidth is usually narrower than the Raman linewidth, even in the fingerprint.

To this day, the most popular laser system for CARS microscopy consists of a broadly tunable picosecond OPO synchronously pumped by the second-harmonic (532 nm) output of a mode-locked Nd:YVO_4 laser. The wavelength of the OPO signal and idler are continuously tunable, making it possible to cover the whole range of chemically important vibrational frequency (200–3600 cm^{-1}) when used in conjunction with the main 1064 nm output from the Nd:YVO_4 laser. Moreover, the pulse trains are intrinsically synchronized and need only to

be overlapped in space and time. This reduces the complexity and enhances the robustness of CARS microscopy systems.

For more details about CARS microscopy, a comprehensive literature review is presented in chapter 2.

1.1.3 CARS spectral imaging

Spectral imaging stems from the combination of spectroscopy and imaging to attain both spatial and spectral information from an object. A spectral image contains the complete or partial spectrum of a sample at each point in the imaging plane. Spectral images are three-dimensional data cubes constituted of a series of two-dimensional images ($I_{x,y}$) for each value of (λ) (Fig. 1.5 a)). Unlike regular images where each pixel stores a grayscale or RGB value, a spectral image is made of spectral pixels that contain the entire measured spectrum at a spatial point. Inversely, for every fixed value of λ, there is a corresponding 2-D grayscale image. As an example, a CARS spectral image of a skin sample incubated in DMSO is presented as a mosaic in Fig. 1.5 b).

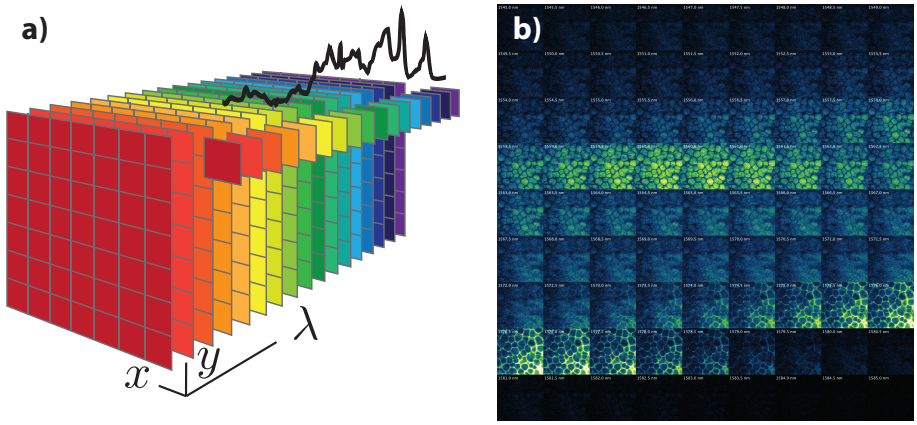

Figure 1.5 – a) Spectral images are made from a series of two-dimensional grayscale images ($I_{x,y}$) for every spectral value (λ), *i.e.* every pixel contains a complete spectrum. b) Example of a spectral image from the skin of a mouse ear incubated in DMSO. The CARS signal from the lipid compartmentalized in the adipocytes shows up first around 2849 cm^{-1} (halfway in the montage) and then the signal from the lipophobic DMSO around 2914 cm^{-1} (towards the end of the montage).

Spectral imaging methods have long been used in such diverse fields as astronomy [Perley et al., 1989], remote sensing [Goetz et al., 1985], archaeology [Liang, 2012], food quality control [Gowen et al., 2007] and medical imaging [Lu and Fei, 2014] to name only a few. In microscopy however, it is only recently that spectral imaging has started to make an appearance in applications such as live cell visualization [Zimmermann et al., 2003] and cytomics [Ecker et al., 2004], cancer research [Barber et al., 2003] and fluorescence microscopy [Haraguchi et al., 2002].

Its ability to identify the chemical composition of samples while retaining some context with the spatial information has made spectral imaging one of the fastest-growing techniques in biophotonics. In practice however, acquiring a complete spectrum or even only a few wavelengths for each point sample can be a difficult task depending on the microscopy technique. In CARS microscopy, the strict requirements regarding the excitation and detection have limited the rate of progress. In this section, we will review the various schemes for CARS spectral imaging and highlight their strengths and limitations. CARS spectral imaging methods can be loosely grouped in two families: broadband and narrowband approaches.

Broadband CARS spectral imaging

Broadband CARS spectral imaging aims to excite several Raman lines simultaneously, usually with a narrowband laser coupled with a broadband source. The narrowband laser determines the inherent spectral resolution of the measurement, and the broadband laser determines the spectral width of the generated CARS spectrum. This is illustrated in Fig. 1.6 where the broadband Stokes beam (ω_s) is coupled with the narrowband pump beam (ω_p) to allow the simultaneous excitation over a wide range of Raman shifts (Ω), generating a wideband anti-Stokes signal (ω_{as}).

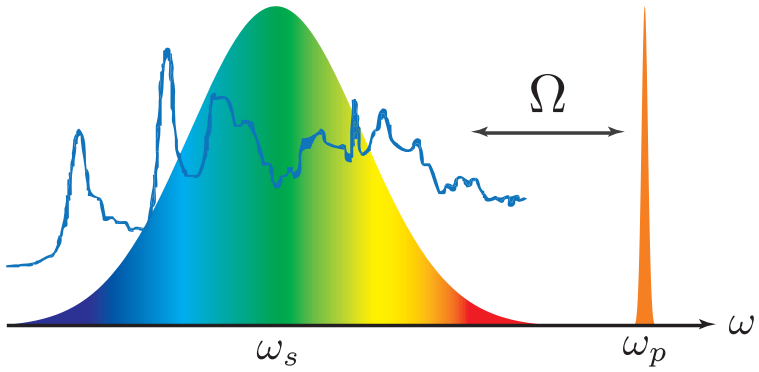

Figure 1.6 – Broadband CARS spectral imaging methods allow the simultaneous excitation of several Raman lines. In this example, the narrowband pump beam (ω_p) is coupled with broadband Stokes beam (ω_s) to simultaneously excite the underlying Raman lines.

The earliest CARS spectral imaging efforts relied on the use of a narrowband picosecond pump beam combined with a broadband femtosecond Stokes beam to acquire CARS spectra in the high-wavenumber region [Cheng et al., 2002b] or across a 180 cm^{-1} wide window tunable from 0–4000 cm^{-1} [Müller and Schins, 2002].

Another approach utilizes a single femtosecond laser as the light source for both the pump and Stokes pulses. This method has the advantage of not requiring laser synchronization. To do that, the bandwidth of one femtosecond beam must be reduced. This can be accomplished

by introducing a filter in the beam to select a small part of the spectrum from one pulse, effectively converting the femtosecond pulse into a picosecond pulse [Kee and Cicerone, 2004]. As well, the pulse can be dispersed by a pair of prisms or gratings and then a physical slit inserted into the dispersed beam to remove a small portion of the spectral bandwidth [Knutsen et al., 2004]. Finally, a third way to accomplish this is to introduce a linear chirp in one of the pulse. The temporal overlap of normal fs pulses with much longer pulses (ps) will act as a temporal gate to use only a fraction of the available bandwidth [Knutsen et al., 2006, Onorato et al., 2007].

Because the pulse bandwidth from common femtosecond lasers is limited to about $\sim$150 cm^{-1}, there are several approaches relying on the generation of supercontinuum to provide a wider spectral coverage (>2500 cm$-$1). Supercontinuum can be generated by injecting ultrashort pulses in a tapered nonlinear fibre [Kee and Cicerone, 2004], a photonic crystal fibre [Kano and Hamaguchi, 2005a,b] or a ultra-high numerical aperture silica fibre with a nearly pure GeO_2 core [Petrov and Yakovlev, 2005]. The most important drawback of supercontinuum based methods is that while they can cover a wide spectral range, they suffer from a lower intensity per spectral unit which is reflected in longer acquisition times when compared to methods using transform-limited fs pulses.

While broadband methods seem to have a major advantage in terms of efficiency, generating CARS spectra by exciting several Raman lines simultaneously actually comes at a price. Current broadband methods typically utilize CCD based spectrometers which have long readout times, limiting their acquisition speed. As well, spectrometers cannot efficiently collect the backscattered light off thick samples because they require a slit to resolve the spectra. In such a case, the problem becomes one of conservation of etendue resulting in very poor collection efficiency in tissue where diffusion is important. These two factors currently limit pixel dwell times to the 10 ms range [Parekh et al., 2010, Okuno et al., 2010].

Although broadband CARS spectral imaging is superior in its analytical capabilities and information content compared to CARS imaging, the associated dwell times are presently more than four orders of magnitude longer. As a result, the usefulness of broadband CARS spectral imaging is fairly limited, especially when working with living specimen or thick turbid samples.

Narrowband CARS spectral imaging

The general principle of narrowband CARS spectral imaging is to encode the frequency of the probed Raman shift in time (Fig. 1.7). This has for direct consequence to remove the need for a spectrometer to resolve the different wavelengths of the CARS spectra. Instead, it becomes possible to use faster, more sensitive detectors such as PMTs, which are ubiquitous in CARS imaging experiments. Moreover, because of their large etendue, such detectors are

better suited for the detection of epi-directed signals from thick tissue samples. As such, narrowband CARS spectral imaging methods might help bridge the gap between imaging and spectral imaging, especially for experiments involving thick tissue or live animal, or even clinical applications.

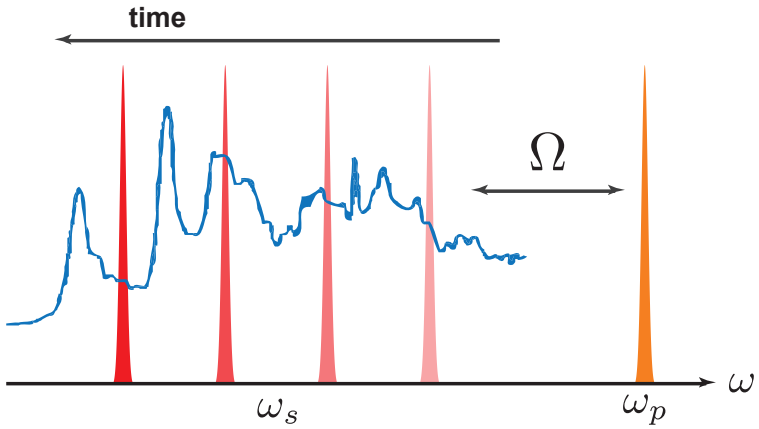

Figure 1.7 – Narrowband CARS spectral imaging methods probe Raman vibrations sequentially over a range of Raman shifts. In this example, the wavelength of the narrowband Stokes beam (ω_s) changes with time to excite the underlying Raman lines.

Perhaps the easiest, or at least most obvious, method to accomplish this consists in using a tunable narrowband source for one of the beams. Using what is now known as the workhorse of CARS microscopy, an optical parametric oscillator (OPO) pumped by the second harmonic of a Nd:YVO_4 picosecond laser, Lin et al. [2011] have acquired spectral images by manually scanning the wavelength of the OPO. The limited spectral range of their experiment, ~200 cm^{-1} in the CH stretching vibrational range (2790–3070 cm^{-1}), proved sufficient to observe compositional variations in the meibomian gland lipids of mice. Others demonstrated similar systems with a marginal improvement in scanning speed but a significant one in usability by automatically adjusting the wavelength of the OPO. In the first instance, the temperature of the LBO crystal in the OPO was adjusted automatically (taking ~10 s) to acquire CARS spectral images over the range 900–3150 cm^{-1} [Brustlein et al., 2011]. In the second instance, only the angle of the OPO intracavity Lyot filter was adjusted automatically, thereby yielding further gain in speed and spectral resolution at the cost of scanning range. Using this system, CARS spectral images were acquired over the range 2880–3020 cm^{-1} with 2 cm^{-1} intervals at a rate of ~4 s per frequency [Garbacik et al., 2012]. Since then, researchers have found that the tuning speed could be greatly improved from several seconds per wavelength to ~100 ms with the use of an electro-optical modulator in the OPO cavity [Kong et al., 2013].

Spectral focusing was initially devised as a way to improve spectral resolution in CARS microscopy experiments using broadband fs pulse [Hellerer et al., 2004, Rocha-Mendoza

et al., 2008]. By controlling the degree of chirp in the fs pulses, the effective Raman resolution is controlled and it was possible to achieve Raman spectral resolution quite comparable ($\sim$8 cm^{-1}) to that achieved with transform-limited ps pulses. Moreover, this method supports rapid tuning of the Raman resonance by changing the time delay between chirped pump and Stokes pulses [Onorato et al., 2007, Pegoraro et al., 2009] and has been used to acquire CARS spectral images [Chen et al., 2011]. The method is illustrated by plotting the instantaneous frequency of the pulses as a function of time (Fig. 1.8). In Fig. 1.8 a), the spectral resolution ($\Delta\Omega$) is poor since the pulses have unmatched chirp while in Fig. 1.8 b), matched chirp pulses result in an improve spectral resolution. We can also see that spectral tuning is achieve by changing the time delay between the pulses.

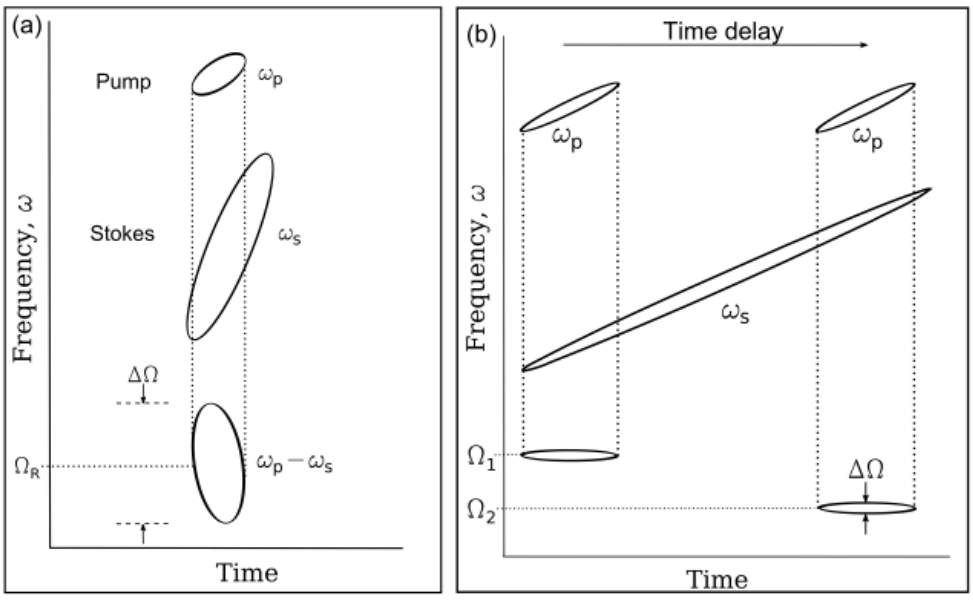

Figure 1.8 – CARS spectral imaging with spectral focusing. In this time-frequency plot, the pump and Stokes pulses are shown as ellipses and the spectral resolution of the CARS process $\Delta\Omega$ is determined by the total height of the ellipse $\omega_p - \omega_s$. The spectral resolution is poor when large bandwidth pulses have unmatched chirps (a) but much improved with narrow instantaneous bandwidths pulses with matched chirp. Figure from [Pegoraro et al., 2009].

The main advantages of spectral focusing methods lie in their use of readily available laser sources whose beams can be easily modified to accommodate the experiment as well as in the control over important parameters such as spectral resolution and bandwidth, and their intrinsic compatibility with other nonlinear modalities (two-photons microscopy, second-harmonic generation). However, since spectral tuning is achieved by changing the relative time delay between the two pulse trains, the spectral tuning speed is limited by the requirement to mechanically move a mirror. Nonetheless, the utility of the method is proven by the numerous reports that have been published in recent years.

Another method uses a Stokes beam based on a mode-locked Ti:Sapphire laser with an acousto-optic tunable filter (AOTF) in the cavity for high speed wavelength tuning (wavelength switch within ∼0.1 ms). The AOTF is an electronically tunable optical bandpass filter whose centre wavelength can be rapidly tuned over a large spectral region by changing the frequency of the driving radio signal. Using this method, CARS spectral imaging was demonstrated first over a limited range ((∼50 cm^{-1})) [Hashimoto et al., 2010], but then over a much wider range (400–2150 cm^{-1} and 1600–3300 cm^{-1}) [Hashimoto et al., 2012]. On top of their fast scanning rate and wide tuning range, AOTF also have the significant capability of operating in random access. This last feature can help shave significant time by acquiring images only in spectral regions of interest as was demonstrated by rapidly switching between 2100 cm^{-1} and 2850 cm^{-1}, the Raman vibration of deuterated and nondeuterated stearic acids respectively [Cahyadi et al., 2013].

More recently, a method based on two laser frequency combs demonstrated the capability to measure complete spectra over a wide bandwidth and with high resolution on a single photodetector [Ideguchi et al., 2013]. Using this novel method, the authors were able to record CARS spectral images ranging from 200–1200 cm^{-1} with a spectral resolution of 4 cm^{-1} at a rate of 12 μs/spectra. However, with their current system design, the total acquisition time was limited by the waiting time between successive spectral acquisitions (∼20 ms). The authors believe that further system development should help overcome this limitation.

1.2 Image analysis

If you torture the data long enough, nature will confess.
— Ronald Harry Coase

Image processing and analysis encompasses a wide variety of techniques. On one hand, image processing tasks generally aim to enhance images by modifying digital images properties such as contrast, brightness, noise, and illumination. On the other hand, image analysis techniques usually strive to extract information by identifying and measuring features and structures revealed by the images. As the principal means of acquiring scientific data from images, methods falling in the latter category often endeavour to reduce an image to some measurable quantity that can then be used for description, comparison, or classification.

The aim of this section is to present a variety of image analysis techniques related to the extraction of quantitative information from digital microscopy images. More specifically, I will cover the basics of image segmentation, object measurements, and image processing in the Fourier domain.

1.2.1 Segmentation

Image segmentation is one of the most important task in digital image analysis, but also one of the most challenging. It is the process of partitioning an image into non-overlapping regions (segments) corresponding to different objects. This transformation aims to simplify an image by changing its representation to something more meaningful and easier to quantify. Once the segments are isolated, the objects can be measured, classified, and analysed.

In human vision, image segmentation takes place effortlessly. It is such a trivial task that most of us do not realise it is happening continuously in our life. Whether we are doing complex tasks such as driving a car: avoiding obstacles, looking for pedestrian or signs or a simple thing such as reaching for a glass of water. Processing digital images on a computer, by comparison, is a laborious, almost impossible task. The images need to be separated in regions representing the objects of interest by grouping pixels sharing some computed properties such as grey level or texture. This is even more difficult in biological images which are often plagued with noise, have limited resolution, and where the objects have ambiguous boundaries.

Because of the importance of segmentation in image analysis, a great variety of segmentation methods have been proposed covering a wide range of applications: machine vision and robotics, objects detection, pattern recognition (faces, fingerprints), biomedical imaging, and microscopy. Generally, the different approaches may not yield exactly the same results, especially when the exact location of object boundaries is subject to interpretation. In such cases, the result from different segmentation algorithms can be combined to produce an improved segmentation. In this section, I will present an overview of the basic segmentation methods as well as a few more specialized techniques. This is not a comprehensive survey of all available methods, but rather an overview of the methods relevant to the work that has been done in this thesis.

Region-based segmentation

Region-based methods attempt to partition an image by grouping pixels that are similar with respect to certain properties such as intensity, texture, or colour. With a region-based approach, each pixel in an image is assigned to a particular label and connected sets of pixels with the same label will form the regions.

A region is a set of connected pixels that are adjacent or touching. This definition of a region is related to an important concept: the connectivity of pixels in a digital image. In a two-dimensional image, there are two rules of connectivity. When only laterally adjacent pixels (up, down, right, left) are considered to be connected, we have “4-connectivity”. If diagonally adjacent pixels are added, then we have “8-connectivity”.

Grey-level thresholding is the simplest way to accomplish the segmentation of an image.

First, a range of intensities in the image (threshold) is defined, than the pixels within this range are classified as the objects of interest (foreground) and the other pixels rejected to the background. The resulting image is usually stored as a binary (or two-level) image and displayed using black and white to distinguish the regions. A grey-level thresholding operation can be described as

$$BW(x,y) = \begin{cases} F, & \text{if } I(x,y) \geq T \\ B, & \text{if } I(x,y) < T \end{cases} \tag{1.5}$$

where $BW(x,y)$ is the segmented image resulting from applying the threshold T to the original image $I(x,y)$. F and B are the foreground and background labels respectively. For cases where the objects of interest are defined by a low grey-level on a high grey-level background, simply inverting the image would unable the use of this formulation for the segmentation.

Multiple ranges of grey-level can be defined in the image to generate a multi-level segmented image. As well, if the objects are differentiated from the background by some other property (texture, colour, etc...), a simple conversion of that property to grey-level would unable the use of thresholding.

Grey-level thresholding is an essential region-based technique that is especially useful for images containing solid, well defined objects on a contrasting background. It is simple to compute and, provided the threshold is chosen correctly, always succeeds in defining objects with closed, connected edges separating regions of uniform, but different, grey levels. The threshold level is usually chosen from the image intensity histogram. Because that choice can have a direct impact on the segmented objects boundary positions and sizes, and therefore affect the values of any subsequent object measurement, the threshold value must be chosen carefully. The effect of varying the threshold value on the segmentation result is demonstrated in Fig. 1.9.

One of the first limitation of grey-level thresholding becomes apparent when working on images where the background grey level and the objects-background contrast vary within the image. In such cases, holding the value of the threshold constant throughout the image is unlikely to produce good results since a value that works well in an image area may not be such a good choice in another area. Adaptive thresholding methods have been developed to better handle such variations by using a threshold that slowly varies with the position in the image. One way to achieve this consists in partitioning an image into non-overlapping blocks whose histograms are then analysed to choose threshold values. Once this is done, a thresholding surface is created by interpolating the threshold values over the entire image.

Exploring threshold values manually is most useful since it gives the user a sense of the spatial distribution of the grey levels in the image. Manually choosing the threshold value (or

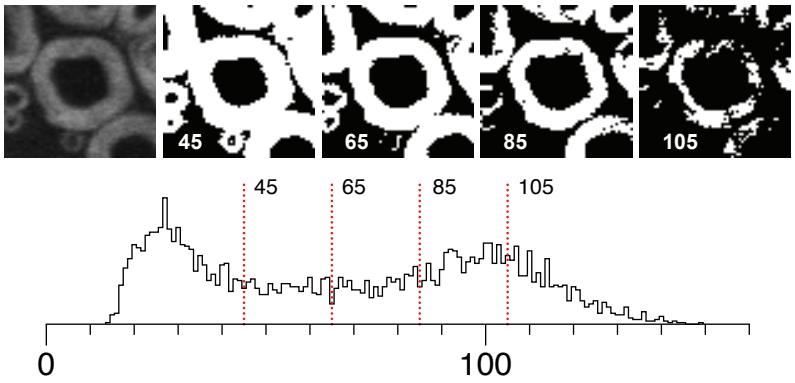

Figure 1.9 – Application of different threshold level to a CARS microscopy image from a transverse section of mouse spinal cord showing the myelin surrounding the axons. From left to right, the original image and the segmented images thresholded at grey levels of 45, 65, 85 and 105 respectively. The bottom panel shows the histogram of the original image with the threshold levels indicated in red.

values) for the final segmentation however, should be avoided for several reasons: it takes time, it does not allow automatic processing and wrong threshold choices will lead to errors in subsequent analysis. Nowadays, many algorithms have been developed for automatically determining the threshold value. For instance, the simplest method locates the peaks in the histogram and sets the threshold either midway, or at the minima between them. Each method makes a different assumption about the image histogram and the best way to divide it into parts. A good comprehensive survey of techniques is available in Sezgin and Sankur [2004].

Ultimately, histogram-based region segmentation methods have a fundamental limitation because histograms describe only the distribution of grey levels without any spatial context. Region-growing and Split-and-merge methods tackle this limitation by harnessing the spatial information contained in the image. Where region-growing aims to group adjacent pixels or small regions together using homogeneity as the main criterion for merging, split-and-merge uses similar homogeneity criteria but differs in the direction of their application (top-down approach). Because they utilize several image parameters simultaneously to determine the final objects shapes, these methods often produce good segmentation results at the cost of being generally computationally more expensive than simpler methods.

Edge-based segmentation

Edge-based segmentation techniques aim to extract object boundaries directly from the images by: 1) locating the edge pixels in the image, and 2) linking adjacent edge pixels into a boundary. Edges are associated with points in an image where the intensity values change sharply, which usually occurs at the objects boundaries.

Edge detection refers to the process of identifying and locating sharp discontinuities in an image. It is often preceded by a pre-processing stage (smoothing, noise filtering). There are several methods to detect edges in two-dimensional images and most of them can be categorized as gradient-based or Laplacian-based methods. While gradient-based methods look for maxima in the first derivative of the image, Laplacian-based methods search for zero-crossings in the second derivative of the image. The difference between most methods lies in the type of pre-processing applied to the image as well as the in the computation of the edge strength.

Edge detection operators are usually implemented as convolution templates. The convolution of a particular template with the image results in an image of the edge strength. For instance, the horizontal and vertical templates for the famous Sobel edge-detection operator are applied to the grey-scale image $I(x, y)$

$$\mathbf{G}_x = \begin{bmatrix} 1 & 0 & -1 \\ 1 & 0 & -1 \\ 1 & 0 & -1 \end{bmatrix} * I(x, y), \ \mathbf{G}_y = \begin{bmatrix} 1 & 1 & 1 \\ 0 & 0 & 0 \\ -1 & -1 & -1 \end{bmatrix} * I(x, y) \tag{1.6}$$

where the $\mathbf{G}_x$ and $\mathbf{G}_y$ are the results of the convolution to find the horizontal and vertical edges. The edge strength is then given by the gradient magnitude

$$\mathbf{G} = \sqrt{\mathbf{G}_x^2 + \mathbf{G}_y^2} \tag{1.7}$$

An example of the application of the Sobel operator to a CARS image of a transverse section from the spinal cord of a mouse is shown in Fig. 1.10. On the left side, the figure shows the original image where the contrast is given by the myelin lipid content and on the right side, the gradient magnitude from the Sobel filter.

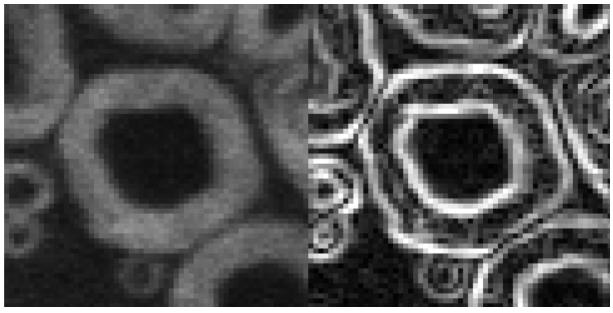

Figure 1.10 – Application of the Sobel edge operator to a CARS microscopy image from a transverse section of mouse spinal cord showing the myelin surrounding the axons. The original image is on the left and the gradient magnitude is on the right.

Edge-based methods work well in images with good contrast between object and background. However, noisy images with smooth transitions and low contrast as is the case in optical microscopy are challenging. Moreover, robust edge linking is often not a trivial task, even when the edge detection step is successful, especially with complex images.

Watershed segmentation

Watershed image segmentation methods usually interpret grey-level images as a topographic surface where high intensity denotes peaks, and low intensity denotes valleys. A region surrounding a closed ridge line is considered as a partitioned region, and its properties are related to the way the surface is derived from the input image.

To identify the ridge lines, the first step consists to fill the local minima with different labels considered to behave like water. As the water level is raised, barriers are built to prevent different labels from merging. The process is illustrated in Fig. 1.11. Once the surface is completely submerged, those barriers form the segmentation result [Beucher and Lantuejoul, 1979].

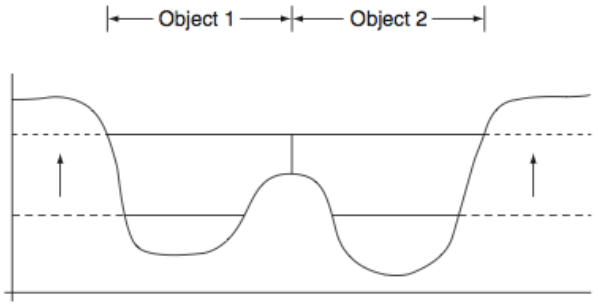

Figure 1.11 – One-dimensional illustration of the watershed segmentation process. The initial threshold level segmenting the image into the proper number of objects (two) is raised gradually, allowing the boundaries to expend but not to merge.

Most watershed methods differ in the way the three-dimensional surface is interpreted from an image. They seldom rely on the original grey level image, preferring instead to interpret the image of the gradient magnitude as elevation information. However, because the gradient is very sensitive to noise and small fluctuations in grey level, using the gradient image directly can lead to over-segmentation. The result is often greatly improved with the use of smoothing filters on the gradient image or by using markers associated with the object or with the background.

Finally, watershed is often used in conjunction with other segmentation methods to separate touching objects in binary images. An example is shown in Fig. 1.12 where two touching circles need to be separated. The surface is created from the distance transform of the binary image and the watershed line separates the touching circles.

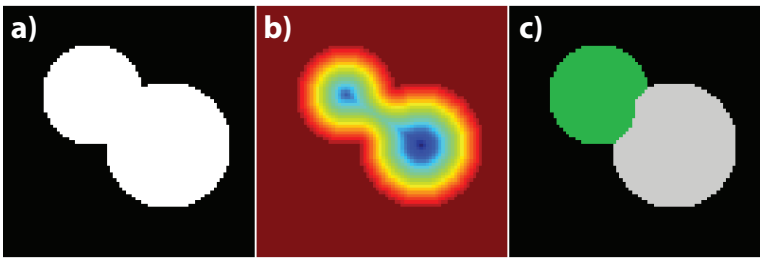

Figure 1.12 – Application of the watershed technique to separate touching objects. a) Binary image of two touching circular features. b) The distance transform of the binary image is computed and c) the watershed line separates the touching circles.

Active contour methods

Active contour is a framework aiming to find a closed contour for delineating a target object [Kass et al., 1988]. The contour detection problem is formulated as an optimization method, *i.e.*, it tries to compute the best contours from several possible contours according to certain criteria. Active contours methods are renowned for their reliability at providing reasonable contours to features with ambiguous boundaries or even for noisy images.

The idea behind active contours (snakes) is to start with an initial guess which is then moved by image forces towards the feature boundaries. They are usually expressed as an energy minimization process where the target is a minimum of a properly formulated energy functional. The energy functional includes image properties like edge magnitude as well as properties that control the way the curve bends and stretches. In this way, the solution represents a compromise between the internal forces designed to keep the model smooth during the deformation process, and the external forces defined to move the model towards an object boundary or some other features within the image. Active contours are called snakes when an explicit parametric representation of the curve is used $(\mathbf{v}(s) = ((\mathbf{x}(s), (\mathbf{y}(s))$. The snake energy functional is then

$$E_{snake} = \int_{s=0}^{1} E_{int}(\mathbf{v}(s)) + E_{im}(\mathbf{v}(s)) + E_{con}(\mathbf{v}(s))\,\mathrm{d}s \tag{1.8}$$

where E_{int}, E_{im} and E_{con} represent the contour internal energy, image energy, and constraint energy. The constraint energy is there to allow higher level information to control the snake evolution and is used only in advanced active contour methods. The process then aims to find a set of point $\mathbf{v}(s)$ that minimizes eq. 1.8

$$\frac{\mathrm{d}E_{snake}}{\mathrm{d}\mathbf{v}(s)} = 0 \tag{1.9}$$

Most active contour methods are distinguished in the way the various parameters control-

ling the snake's behaviour are defined. For example, the original formulation of the image energy included contributions from lines, edges, and terminations

$$E_{im} = w_{line}E_{line} + w_{edge}E_{edge} + w_{term}E_{term} \tag{1.10}$$

where E_{line}, E_{edge}, and E_{term} denote their respective energy, and w_{line}, w_{edge}, and w_{term} the related weighting coefficients. In this formulation, the line energy is usually set to the image intensity while the edge energy comes from the application of an edge detection operator and the rarely used terminaison energy is related to the curvature of level image contour. As well, the snake's internal energy is usually defined by the sum of the first- and second-order derivatives around the contour

$$E_{int} = \alpha(s)\left|\frac{\mathrm{d}\mathbf{v}(s)}{\mathrm{d}s}\right|^2 + \beta(s)\left|\frac{\mathrm{d}^2\mathbf{v}(s)}{\mathrm{d}s}\right|^2 \tag{1.11}$$

The first-order differential measures the elastic energy due to stretching and the second-order differential the curvature energy resulting from bending. The values of the weighting coefficients α and β are chosen to control the shape that the snake aims to attain.

Methods based on parametric active contours (snakes) have the advantages of being robust to image noise as well as gaps in feature boundaries, but this framework also restricts the adaptability of the boundaries to the point where splitting or merging of parts is not allowed. To solve this problem, another form of active contours called level sets (or geometric active contours) have been introduced to handle topological changes more naturally [Osher and Sethian, 1988]. Level set methods aim to find the contour shape without parameterizing it. In this framework, by finding the zero level set of a function, the curve description becomes implicit [Sethian, 1999]. The zero level can be visualized as a slice in a three-dimensional surface (Fig. 1.13). As the contour evolves, the surface is sliced at different level, allowing it to split or merge.

As an extension of the active contour model, the level set framework can deal with multiple contours but is generally less robust to boundary gaps, difficult to implement, and computationally inefficient [Suri et al., 2002]. Despite these shortcomings, level set methods have gained a significant amount of traction and several implementations have been published. One of the most popular level set technique called *active contour without edges* was introduced by Chan and Vese [2001] based on the energy functional developed by Mumford and Shah [1989]. Their model is different from others in that it avoids using gradient information, favouring instead regional image statistics. Doing so helps avoid boundary leakage which can cause it to collapse. Also, it tends to work well in images with features having weak

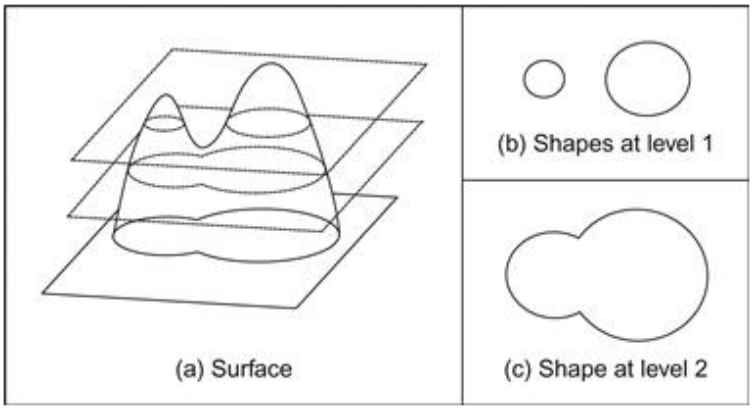

Figure 1.13 – a) The contour evolution is handled by slicing a surface at different levels. This enables the contour shape to split (b) or merge (c). Figure from Nixon and Aguado [2012].

or diffuse boundaries, it is more robust to noise and can address problems related to the initialization. An example of the application of the Chan-Vese algorithm is given in Fig. 1.14.

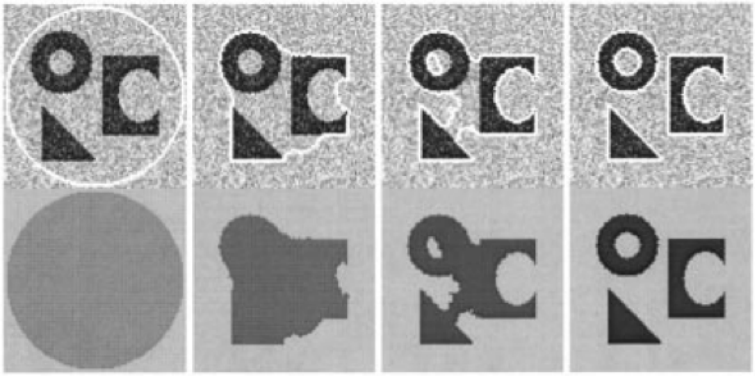

Figure 1.14 – The level set method *active contour without edges* can detect multiple objects from a noisy image. The evolution of the contour is ordered from left to right. Figure from Chan and Vese [2001].

1.2.2 Objects measurements

In section 1.2.1, we discussed segmentation methods for extracting features from digital images. In this section, the discussion will focus on ways to obtain quantitative measurements from the segmented objects. While the specific motivations for performing object measurements are strongly related to the application, the basic objective remains to provide some level of objectivity and quantification to the description of the various features that populate an image.

Object measurement methods are used to compute properties such as area, perimeter, average grey level, and shape to describe object morphology. These measurements can then eas-

ily be incorporated in statistical analysis or used to discriminate between objects or measure their level of similarity. Objects measurements can be classified as geometric measurements when the objects are treated as binary objects or intensity measurements when the pixels grey levels are considered.

Geometric measurements

A binary object can be described in terms of its geometric properties. Some of the most common properties include size, shape, and position relative to a frame of reference.

Lets first consider the function $I(x, y)$ describing an object on a M×N binary image resulting from some previous segmentation

$$I(x,y) = \begin{cases} 1, & \text{if } (x,y) \text{ is part of the object} \\ 0, & \text{otherwise} \end{cases} \tag{1.12}$$

where x and y are indices in the image coordinate space.

The size of an object is usually described in terms of its area and perimeter. For a binary image, the area of an object is simply defined as the sum of all its "on" pixels

$$A = \sum_x \sum_y I(x,y) \tag{1.13}$$

Once the area of an object has been measured, it is frequently expressed in terms of its equivalent circular diameter because it provides a convenient linear measure of the object size irrespective of its shape

$$D_{eq} = \sqrt{\frac{4A}{\pi}} \tag{1.14}$$

The perimeter of a feature is well defined in the continuous real space but that is not the case in a digital image. Because of the discrete spatial arrangement of pixels, perimeter measurement is normally biased and ultimately, the perimeter value depends on whether a pixel is treated as a point or a little square [Hetzner, 2008]. For this reason, there are several methods to measure the perimeter. The simplest way to estimate the perimeter of an object is to count boundary pixels: *i.e.* pixels with a value of "1" that have at least one neighbouring pixel with a value of "0". By this definition, the determination of the boundary pixels depends on the interpretation of connectivity which was introduced in section 1.2.1.

Another useful set of size properties comprises the area and perimeter of the convex hull and of the minimum bounding box. Both properties are computed in the same way while considering the convex hull of the object or its minimum bounding box instead of the object itself. The convex hull of an object can be conceptualized as the shape formed by a rubber

band stretched around it. The minimum bounding box is defined as the smallest box within which the object can be contained.

The minimum and maximum Feret diameters (or calliper diameters) are also considered useful size descriptors. The Feret diameter is the distance between two parallel lines tangent on either side of the object. The minimum and maximum Feret diameters are found by considering all possible angles.

An object can also be defined by its position and orientation relative to some frame of reference. The position is usually given by the object centroid (x_c, y_c) computed as

$$\begin{aligned} x_c &= \frac{1}{A} \sum_x \sum_y x\, I(x,y) \\ y_c &= \frac{1}{A} \sum_x \sum_y y\, I(x,y) \end{aligned} \tag{1.15}$$

The orientation of the object can be measured by computing the axis of least inertia. This axis is defined such that the sum of the squares of the distance of each pixel to the axis is minimized. It can be calculated using

$$\tan(2\theta) = \frac{2 \sum_x \sum_y\ x\, y\, I(x,y)}{\sum_x \sum_y\ x^2\, I(x,y) - \sum_x \sum_y\ y^2\, I(x,y)} \tag{1.16}$$

where θ gives the orientation of the axis of least inertia relative to the x-axis.

Shape features are another type of geometric measures frequently used to describe objects and in tasks such as object recognition and object comparison. Some of the most popular shape descriptor are dimensionless ratio invariant to translation, rotation, and scaling, that are defined from some size parameters. Since there are hundreds of ways that these can be combined, we will only consider some commonly used shape parameters.

The form factor, also called the circularity, is typically used to define the regularity of an object and takes a maximum value of 1 for a circle. The reciprocal value of the form factor, usually called the roundness is also sometimes used. The form factor is defined from the area A and perimeter P as

$$\text{Form factor} = \frac{4\pi A}{P^2} \tag{1.17}$$

Another property used to characterize the regularity of an object is the compactness. It is defined using the area A and the maximum Feret diameter D_{max} as

$$\text{Compactness} = \frac{\sqrt{4A/\pi}}{D_{max}} \tag{1.18}$$

The solidity and the convexity are two shape descriptor related to the object convex hull. The solidity is given by the proportion of the pixels in the convex hull (A_{conv}) that are also in the

object

$$\text{Solidity} = \frac{A}{A_{conv}} \tag{1.19}$$

The solidity equals 1 for an object with a concave boundary and is smaller than 1 for an object possessing a convex boundary. The convexity is similarly defined as

$$\text{Convexity} = \frac{P_{conv}}{P} \tag{1.20}$$

The extent is given by the proportion of the pixels in the bounding box that are also part of the object. It is computed as

$$\text{Extent} = \frac{A}{A_{boundingbox}} \tag{1.21}$$

Another set of shape descriptors is derived from their moments [Hu, 1962]. Image moments provide a global description of a shape by describing the arrangement of the pixels within it. The moment of order $(p + q)$ of a function $I(x, y)$ describing a discrete image is defined as

$$m_{pq} = \sum_x \sum_y x^p y^q I(x, y) \Delta A \tag{1.22}$$

where ΔA is the area of a pixel usually assumed to be 1. The only zero-order moment gives the area of the object and is given by

$$m_{00} = \sum_x \sum_y I(x, y) \tag{1.23}$$

The two first-order moments, m_{01} and m_{10}, are given by

$$m_{10} = \sum_x \sum_y x I(x, y) \ , \ m_{01} = \sum_x \sum_y y I(x, y) \tag{1.24}$$

The object centre of mass $(\bar{x}, \bar{y})$ can be computed from the ratio of the first-order to the zero-order moments

$$\bar{x} = \frac{m_{10}}{m_{00}} \ , \ \bar{y} = \frac{m_{01}}{m_{00}} \tag{1.25}$$

which is equivalent to equation 1.15 presented earlier.

Higher order moments $(p + q > 1)$ are usually defined in terms of the object centre of mass. These are called central moments since they are location invariant. They are defined as

$$\mu_{pq} = \sum_x \sum_y (x - \bar{x})^p (y - \bar{y})^q I(x, y) \tag{1.26}$$

The three second-order central moments are useful properties providing a measure of the dispersion of the pixels of an object with respect to its centroid. They are usually written in term of the raw moments

$$\mu_{20} = m_{20} - \bar{x}\, m_{10}\ ,\ \mu_{02} = m_{02} - \bar{y}\, m_{01}\ ,\ \mu_{11} = m_{11} - \frac{m_{10} m_{01}}{m_{00}} \tag{1.27}$$

Second-order moments are often used to derive three important shape descriptors: eccentricity and major and minor axis lengths. These are usually computed from the ellipse that has the same second-order moments as the object. The major and minor axis lengths are computed directly and the eccentricity is given by the ratio of the distance between the foci of the ellipse and its major axis length.

The number of moments continue to rise exponentially as their order increases.

grey-level measurements

Several object measurements can be derived from the intensity distribution of the pixels associated with the object. Most geometric measurements defined earlier for binary objects can be adapted to produce grey-level measurements. The most common grey-level measurements will be described in this section.

The simplest property to compute is probably the integrated grey level. It represents the "mass" of the object and is given by the sum of the grey levels of all the pixels in the object.

Most of the other grey-level properties are computed from the object histogram. Usually, the histogram is normalized by the size of the object to give the probability density function (pdf) of the grey levels. Properties derived from the normalized histogram provide statistical descriptors characterizing the grey-level distribution within the object. The grey-level probability density function $P(g)$ of an object is given by

$$P(g) = \frac{h(g)}{A} \tag{1.28}$$

where $h(g)$ is the number of pixels with grey level g and A the area of the object (total number of pixels).

The most common first-order grey-level properties computed from the pdf include the mean, standard deviation, mode, skew, energy and entropy.

The average intensity (mean grey level) of the object, is calculated by summing over all grey levels g

$$\bar{g} = \sum_{g} g P(g) \tag{1.29}$$

The standard deviation quantifies the spread of grey levels within the object. It is sometimes interpreted as a measure of contrast. It is defined as

$$\sigma_g = \sqrt{\sum_g (g - \bar{g})^2 P(g)} \tag{1.30}$$

The skew is a measure of the asymmetry of the probability distribution of grey levels. It is calculated by

$$\kappa = \frac{1}{\sigma_g^3} \sum_g (g - \bar{g})^3 P(g) \tag{1.31}$$

The entropy is a measure of the grey level dynamic range. It is given by

$$Entropy = -\sum_g P(g) \log_2[P(g)] \tag{1.32}$$

Finally, the energy is a measure of the image smoothness in terms of grey levels. It is given by

$$Energy = \sum_g [P(g)]^2 \tag{1.33}$$

Textures are another type of grey-level measurement that quantifies higher-order relationships within their probability distribution. In the context of image analysis, a texture can be defined as a property describing the spatial arrangement of the intensity of pixels in a local region. They characterize patterns in the variation of grey levels that are too small to be identified as separate objects. In that sense, textures, or at least their perception, are scale dependant. They are, however, usually independent of the position, orientation, size, shape, and average grey level of an object.

Although there are many texture measurements, the most popular properties were introduced by Haralick et al. [1973]. The basis for Haralick's texture features is the grey-level co-occurrence matrix (GLCM), a two-dimensional histogram that measures the frequency of a grey-level pair separated by a particular offset distance in a particular direction. The GLCM is a square matrix of dimension L where L is the number of grey levels in an image. For a given distance offset and direction, the elements $\mathbf{P}(i, j)$ of the GLCM are generated by counting the number of times a pixel with value i is separated by the specified offset in the specified direction from a pixel with value j. The matrix is then normalised to the total number of such comparisons made so that each entry can be considered to be a probability. The scale dependence is reflected in the fact that selecting a different offset direction and distance gives rise to a new GLCM. Once a GLCM has been computed, one can calculate the fourteen statistics introduced by Haralick. Examples include entropy H, defined as

$$H = -\sum_{i,j} \mathbf{P}(i, j) \log(\mathbf{P}(i, j)) \tag{1.34}$$

inertia I, given by

$$I = \sum_{i,j} (i-j)^2 \mathbf{P}(i,j) \tag{1.35}$$

energy, which is

$$E = \sum_{i,j} [\mathbf{P}(i,j)]^2 \tag{1.36}$$

and maximum probability P_{max}, given by

$$P_{max} = \max_{i,j} \mathbf{P}(i,j) \tag{1.37}$$

1.2.3 Image analysis in frequency space

Because of the way we perceive of the world around us, most people will perform their image analysis tasks in the original spatial domain of the images. However, while an image represented in frequency space may not be easily interpreted by a person, working in frequency space to perform certain image processing tasks can be very useful. The Fourier transform, which transforms an input image from the spatial domain to the frequency domain, is a very important image processing tool used in a wide range of applications, such as image filtering, image reconstruction and image compression.

Because the mathematical background of the Fourier Transform is very well documented in many textbook and we are only concerned with digital images, the discussion in this section will be restricted to the discrete Fourier transform (DFT). Instead of working on a continuous function, the DFT converts a sampled function from its original domain to the frequency domain. In images, the number of frequencies corresponds to the number of pixels in the spatial domain image so that the transformed image has the same size as the original.

For an image of size $M \times N$ represented by the function $I(x,y)$ in the spatial domain, the two-dimensional DFT is given by

$$F(u,v) = \frac{1}{MN} \sum_{x=0}^{M-1} \sum_{y=0}^{N-1} I(x,y)\, e^{-i2\pi(ux/M + vy/N)} \tag{1.38}$$

where u and v are spatial frequencies in the x and y directions. The exponential term is the basis function for the correspondence to the Fourier space and it comprises sine and cosine waves with increasing frequencies. The frequency resolution is related to the spatial resolution ($\Delta u = 1/\Delta x$) and the maximum frequency is given by $u_{max} = \frac{M}{2\Delta x}$. The DC-component $F(0,0)$ represents the average grey level of the image and the component $F(M-1, N-1)$ represents the highest frequency.

The inverse Fourier transform, used to transform the image back to the spatial domain, is given by

$$I(x,y) = \sum_{u=0}^{M-1} \sum_{v=0}^{N-1} F(u,v)\, e^{i2\pi(ux/M + vy/N)} \tag{1.39}$$

The result of the Fourier transform consist of an image with complex numbers which is often processed to produce two images representing the magnitude and the phase. The magnitude (or spectrum) is given by

$$|F(u,v)| = \sqrt{\Re[F(u,v)]^2 + \Im[F(u,v)]^2} \tag{1.40}$$

where $\Re[F(u,v)]$ and $\Im[F(u,v)]$ are the real and imaginary part of $F(u,v)$. The phase is given by

$$\phi(u,v) = \tan^{-1}\left[\frac{\Im[F(u,v)]}{\Re[F(u,v)]}\right] \tag{1.41}$$

In image processing, it is customary to display only the magnitude since it contains most of the geometric structure information from the spatial domain, but the phase is required to re-transform the image back to the spatial domain.

An example of the application of the Fourier transform to a CARS image from a mouse spinal cord is given in Fig. 1.15. The Fourier coefficients produced by eq. 1.38 are arranged such that the DC-component is in the corners and the high frequencies in the centre (Fig. 1.15 b)). Because of the periodicity of the content, the layout of the frequency domain content is usually changed by swapping the 1st and 3rd quadrants and the 2nd and 4th quadrants. This layout is considered more intuitive since the usually stronger low frequencies are in the centre and the high frequency content on the outside. Moreover, because of their large dynamic range, the Fourier coefficients usually requires a logarithmic transformation to be displayed correctly (Fig. 1.15 c)).

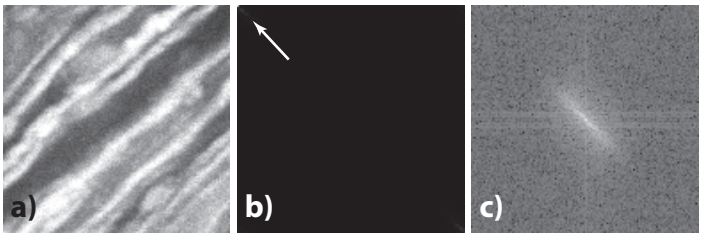

Figure 1.15 – A 2D Fourier transform. a) CARS image from a longitudinal tissue section of mouse spinal cord showing the myelin wrapped around the axons. b) The dynamic range of the raw DFT output is too large for proper display and the DC component is in the upper left corner (arrow). c) The modified DFT output after a logarithmic transformation and a shift in the layout.

The applications of the Fourier transform in image analysis tasks are too numerous to attempt a comprehensive description. Focusing on its use in microscopy, one of the most obvious utilisation is frequency filtering. This can be done by using a mask to select (or eliminate) certain frequencies prior to the image reconstruction. For example, to create a low-pass filter, one would simply need to set all frequencies above a certain value to zero. As well, because it is very sensitive to the actual resolution of the image, the Fourier transform can be used to measure the spatial resolution. Specifically, when a microscope image is oversampled, recorded with more pixels than the optical resolution, the magnitude of the image in the frequency domain will display an abrupt drop in magnitude beyond a certain frequency. This is because those higher frequencies contain no information but only random pixel noise. Finally, the Fourier Transform can also be used to gain information about the geometric structure of the spatial domain image. This can be useful to study images of tissue displaying some type of macroscopic organization. For instance, the image presented in Fig. 1.15 a) shows (a tiny section of) highly organized myelinated axons. Applying the transformation to the image reveals the general orientation of the fibres as can be seen from the diagonal structure in Fig. 1.15 c).

1.3 Main research goals and thesis plan

The compound microscope was invented sometimes in the 17^{th} century. Comparatively, it could be said that coherent anti-Stokes Raman scattering (CARS) microscopy, first demonstrated in 1982 [Duncan et al., 1982], is a young and immature technique. Nonetheless, after gaining the attention of many researchers, it has gathered a significant amount momentum in the field of optical microscopy, especially in biophotonics. This is easily explained since CARS microscopy satisfies three key requirements imposed on optical imaging techniques for the visualization of living biological specimens: noninvasiveness, chemical selectivity, and high sensitivity.

Despite the many advantages of CARS microscopy, there are still several obstacles that prevent the wide-scale adoption of the technique in biology and medicine: it requires expensive equipments, CARS microscopes are complex and difficult to operate, as a contrast mechanism, it lacks versatility, and finally, common image analysis methods need to be adapted and new ones added to the toolbox. For a young researcher, this is all extremely exciting since it promises to provide many challenges with a fair share of risk and a chance to make a difference. Therefore, this thesis is first and foremost about easing the adoption of CARS as a microscopy technique by addressing first one of the technical limitations of current implementations (chapter 3) and then expending the toolbox of adapted image analysis methods (chapters 4 and 5).

In chapter 2, we present a literature review of minimally invasive imaging methods relying

on vibrational contrast. While the review focuses on the application of Raman-based techniques for *in vivo* imaging, it also covers other imaging and spectroscopy applications in biology and medicine.

In section 1.1.3, the case was made about the many benefits of CARS spectral imaging systems. Also, as indicated by the ever growing number of related publications, there is a palpable interest in developing such systems. However, if the sheer diversity of the working principles of current implementations is any indication, the perfect CARS spectral imaging system has yet to be created. The first challenge that was addressed in this thesis concerns some of the shortcomings of CARS as a tool for spectral imaging, especially for experiments requiring that the signal is collected in the epi-direction (thick tissue and *in vivo*, clinical applications). Broadband methods based on transform-limited ultrashort pulses or supercontinuum generation have been successful with optically thin samples and in greatly simplifying the process of probing of multiple Raman lines. However, the requirement for a spectrometer leads to poor efficiency for collecting diffuse backscattered signal from turbid samples. Narrowband methods avoid collection efficiency problems since they generally rely on large area detectors already used in imaging for the signal detection. Typical CARS imaging system have access to a wide range of Raman lines, but their slow tunability imposes strong limitation to their usability in spectral imaging. Other narrowband methods relying on spectral focussing of broadband pulses or the use of an acousto-optic tunable filter are either limited in their vibrational tuning range or speed. Consequently, in order to surpass the capabilities of current CARS spectral imaging systems, it is likely that new laser sources will be required. This was the basis for the paper presented in chapter 3 where we introduced a novel CARS spectral imaging system. This original contribution addresses mainly the issue of vibrational tuning speed with a system that is many orders of magnitude faster than other narrowband techniques. Being based on a synchronised fibre laser, it also has other important advantages such as robustness, ease of use, and portability.

For many years, a significant fraction of the work done in Dr. Côté's lab was focussed on the development of a video-rate CARS microscopy platform. Our CARS microscope was designed specifically to satisfy the requirements of *in vivo* imaging experiments looking at the spinal cord of mice as well as the acquisition of large-scale maps from nerve cross sections. As a result, we have been conducting such experiments regularly for many years now as part of our multiple sclerosis research program. Consequently, the amount of image data started to accumulate at an alarming rate and we quickly realized that we had no way to properly analyse it using commonly available tools. This was due as much to the specifics of the biological questions that we were trying to answers as to the characteristics of CARS microscopy images. With this in mind, I initiated two image analysis projects with the intent of addressing some of those pressing needs.

Multiple sclerosis is a neurodegenerative disease that causes the degeneration of myelin

wrapped around the axons. Little is known about the exact sequence of events leading to lesion formation and the key players that are involved. Therefore, we set out to do is a series of experiments aimed at answering those questions. It turns out that CARS microscopy is an ideal tool for that task since it can easily "see" the myelin and hence the lesions that might appear when the disease strikes. What was needed, however, was a way to assess quantitatively the severity of individual lesions by objectively evaluating the myelin morphology. This was the main goal of the paper presented in chapter 4, where we introduced an automated method to quantify the local organization of myelinated axons in the spinal cord. Using a 2D-FFT, we can extract the average orientation and directional anisotropy of the fibres within contiguous image domains in the CARS images from longitudinal tissue sections. Those features were then used to calculate a new parameter, the CCP, representing the correlation between orientations of adjacent domains. We then showed that the CCP was a good proxy for the degree of organization/disorganization in the myelin structure.

The ability to assess the myelin health in longitudinal tissue sections is a very potent tool because it is compatible with *in vivo* experiments where the mechanisms leading to the degeneration can be studied. However, the limited penetration depth of CARS combined with the longitudinal view of the spinal cord does not permit to evaluate deep nerve fibres. Furthermore, myelin morphology is usually measured from images of transverse tissue sections and there is an extensive history of publications on the subject. This was the basis for the second image analysis project which led to the paper presented in chapter 5. This paper introduces a method for the automated segmentation of nerve fibres in CARS images of transverse tissue sections. This tool should enable us to get a more comprehensive picture about the evolution of the myelin health in the context of multiple sclerosis, but also of other pathologies.

Chapter 2

In vivo optical monitoring of tissue remodeling and diseases with vibrational contrast

S. Bégin[1,2], E. Bélanger[1,2], S. Laffray[1], R. Vallée[1,2,3] and D. Côté[1,2,3]

[1] Centre de Recherche Université Laval Robert-Giffard (CRULRG), Université Laval, Québec, Qc, G1J 2G3, Canada
[2] Centre d'Optique, Photonique et Laser (COPL), Université Laval, Québec, Qc, G1V 0A6, Canada
[3] Département de Physique, de Génie Physique et d'Optique, Université Laval, Québec, Qc, G1V 0A6, Canada

2.1 Résumé

Les études de remodelage tissulaire requièrent des techniques d'imagerie *in vivo* qui sont aussi peu envahissantes que possible pour éviter de perturber le micro-environnement à l'étude. À cette fin, les techniques Raman spontanées ont été utilisées mais leur faibles signaux ont, la plupart du temps, limité leur application à des mesures spectroscopiques discrètes. De nouvelles techniques basées sur l'effet Raman telles que la diffusion Raman cohérente et la diffusion Raman stimulée peuvent surmonter cette limitation. Ce manuscrit traite des applications en imagerie et en spectroscopie avec un contraste basé sur l'effet Raman dans le but d'observer les tissus vivants et décrit comment ces applications peuvent être combinées à des fins d'imagerie spectrale. En utilisant des techniques de micro-spectroscopie Raman non linéaires, il est possible de réaliser de l'imagerie *in vivo*.

2.2 Abstract

Studies of tissue remodeling require *in vivo* imaging techniques that are as minimally invasive as possible to avoid microenvironment perturbations. To this end, spontaneous Raman techniques have been used but low signals have limited their application mostly to point spectroscopy measurements. Novel Raman-based techniques such as coherent and stimulated Raman scattering can overcome this limitation. This manuscript discusses imaging and spectroscopy applications with Raman-based contrast for *in vivo* tissue monitoring, and how these can be combined into spectral imaging. Using nonlinear Raman microspectroscopy techniques, *in vivo* imaging can be performed.

2.3 Introduction

Understanding tissue remodeling in early stages of a disease or an injury implies knowing the nature of the tissue as well as the spatial organization of its constituents. In this regard, technological developments are continuously improving our capabilities to improve both diagnosis and treatment. This is undoubtedly a difficult task: these early changes are often subtle in nature and restricted to a small volume. In addition, the restructuring of tissue dictates that observations should be performed *in vivo* to avoid leaving out important factors that would be hard to control *in vitro* such as gradients of molecular factors or dynamic expression of cell receptors. Hence, imaging techniques must be highly specific and must have the capability of rapidly sampling large tissue volumes *in vivo* with good spatial resolution while minimally interfering with the processes going on in tissues. Optical-based techniques are well-suited for this task because of their versatile contrast mechanisms, high spatial resolution and general compatibility with *in vivo* settings. Endogenous contrast mechanisms based on multiphoton processes such as the Raman effect include a large variety of techniques sensitive to molecular vibrations. The interest in Raman-based techniques stems from their sensitivity to changes in the tissue biochemistry without the need for exogenous contrast agents, eliminating problems related to the delivery, specificity and invasiveness of those markers. These techniques share the common property that incident photons will produce new photons at a different wavelength with an energy shift directly related to the vibration. They can be incorporated into two broad classes of modalities for characterizing tissues: imaging and point-spectroscopy. In imaging, one or a few contrast mechanisms are combined to obtain a limited amount of information with all the benefits of images (high sampling, high spatial resolution, context, user feedback, etc.). On the other hand, spectroscopic techniques provide very high information content with typically low spatial sampling (a few points). Raman spectroscopy has a demonstrated diagnostic potential in oncology *in vivo* or *ex vivo* for a number of organs such as the colon [Chowdary et al., 2007], oesophagus [Kendall et al., 2003], stomach [Kumar et al., 2007], breast [Haka et al., 2005, Brozek-Pluska et al., 2008], cervix [Robichaux-Viehoever et al., 2007, Lyng et al., 2007], skin [Nijssen et al., 2002], blad-

der [Koljenovic et al., 2005a] and brain [Koljenovic et al., 2005b, Krafft et al., 2005] to name only a few. The importance of such results are not only limited to the development of *in vivo* tools, but may also prove useful to improve the diagnostic accuracy of current methods, reduce inter-observer variability [Haggitt, 1994] and augment our understanding of carcinogenesis processes. Unfortunately, the volume of tissue sampled by spectroscopic means is usually small, as the time necessary to acquire good spectra is long. It is the combination of both modalities into spectral imaging that has the most potential for tissue monitoring but progresses are limited by technological hurdles that will be discussed.

The purpose of the present article is to discuss state-of-the-art minimally invasive optical techniques based on endogenous contrast for monitoring tissue remodeling after injuries or diseases. This will be illustrated by examples with Raman-based techniques. The next section introduces recent advances in imaging based on vibrational contrast with coherent anti-Stokes Raman scattering (CARS) and stimulated Raman scattering (SRS) as they pertain to imaging diseases and pathologies at high spatial resolution. This is followed by a discussion on recent advances combining both spectroscopy and imaging in spectral imaging applications.

2.4 Imaging

2.4.1 Coherent anti-Stokes Raman scattering

In Raman-based techniques, the contrast is provided by the scattering of incident photons into a range of photons that carry the signature of the different molecular vibrations in their frequency shifts. It is the ability to probe and possibly identify common molecular bonds found in lipids, proteins, nucleic acids and water that makes Raman-based spectroscopy an appealing technique for tissue studies. There are two spectral regions of high information content in tissue: the high wave number region ($\sim$2400–3800 cm^{-1}) and the fingerprint region ($\sim$400–1800 cm^{-1}), sensitive respectively to molecular bonds with (C–H, O–H, etc.) and without (C–C, C=C, C–O, N–O, etc.) hydrogen. Typical Raman lines in the fingerprint region are relatively narrow (10–20 cm^{-1}) but about ten times broader in the high wave number region. For tissue spectroscopy, information in the fingerprint region is mostly extracted from the position and height of the lines, whereas in the high wave number region information comes from the lineshape of the vibrations, as was shown by Puppels' group [Koljenovic et al., 2005a]. For tissue diagnosis applications, the use of statistical methods for the classification of the spectral data is required, and sufficient, to extract the necessary information (for a review, see [Krafft et al., 2009b]). The most important limitation of the spontaneous Raman effect comes from the low scattering cross-sections, leading to photon conversion efficiencies typically ranging from 10^{-7} to 10^{-15} in tissue [Tuchin, 2007]. This leads to either low signals or long acquisition times. On the other hand, coherent anti-Stokes raman

scattering (CARS) is a third-order nonlinear process that benefits from the same specificity as spontaneous Raman but the coherent nature of the process makes the generated signal intensity significantly higher ($\sim 10^5$) than what is obtained with spontaneous Raman scattering for large concentrations of oscillators [Tolles et al., 1977b]. It is capable of probing specific molecules (i.e., single Raman line) in living cells with excellent sensitivity and a high time resolution. Since its first demonstration [Duncan et al., 1982], CARS microscopy has been used to visualize lipids (CH_2 symmetric stretching vibration at 2845 cm^{-1}) [Zumbusch et al., 1999b] but also the DNA (phosphate stretch vibration) and proteins (amide I vibration) in living cells [Cheng et al., 2002a]. The signal from lipids is so strong that it has allowed *in vivo* tissue imaging at video-rate [Evans et al., 2005] as well as visualization of single phospholipid bilayers [Potma and Xie, 2003]. In fact, most *in vivo* applications focus on lipid imaging (CH) and water imaging (OH) since these components provide the largest signals in tissue. Figure 2.1 illustrates common biological tissues that can be imaged with CARS nowadays, based on the state-of-the-art technology (integrated pixel dwell time of a few microseconds [Veilleux et al., 2008]). Figure 2.1(a) shows adipocytes at approximately 80 μm deep in freshly excised rat skin. The contrast is endogenous to the sample, arising from the lipid-rich structures present in the skin. Figure 2.1(b) represents a multimodal image of rabbit aorta. All signals are endogenous to the sample. They come from the lipids (CARS - red), collagen (second-harmonic - blue) and smooth muscle elastin (2-photon excitation fluorescence - green). Figure 2.1(c) depicts the parallel running profile of highly oriented myelin sheaths of live white matter in rat spinal cord tissue. It is worth noting that the signal comes only from the multilayered membrane of myelin, not from the axons. Finally, Fig. 2.1(d) displays a myelin image from a transverse section of fixed white matter rat spinal cord tissue. The circular geometry of the closely wrapped leaflets of myelin around the axon is clearly visible.

What is the origin of the CARS signal? It comes from the coherent superposition of the microscopic dipoles driven by the pump (E_p) and Stokes (E_S) fields. The nonlinear interaction of the two fields generates the macroscopic third-order polarisation ($P^{(3)}$) at the anti-Stokes frequency $\omega_{aS} = 2\omega_p - \omega_S$. The anti-Stokes signal intensity can be written as $I_{aS} \propto |\chi^{(3)}|^2 I_p^2 I_S \mathrm{sinc}^2(\Delta k z/2)$ where $\chi^{(3)}$ is the complex nonlinear optical susceptibility of the material comprising non-resonant ($\chi^{(3)}_{NR}$) and resonant ($\chi^{(3)}_R$) component, $\Delta k = |\mathbf{k}_{aS} - (2\mathbf{k}_p - \mathbf{k}_S)|$ is the wavevector mismatch and z is the thickness of the object. This dependence has five noticeable consequences: 1) the CARS signal benefits from optical sectioning due to the nonlinear intensity dependence, 2) the *phase matching condition* modulates the overall intensity, 3) the multiple coherently additive contributions to $\chi^{(3)}$ can lead to the resonant contribution being masked by other non-resonant contributions, 4) the nonlinear mixing depends on the tensor nature of the material and the polarization of the input beams, and finally, 5) the intensity of the CARS signal is proportional to the square of the number of vibrational oscillators as a direct consequence of the $|\chi^{(3)}|^2$ term. Because of the extremely small inter-

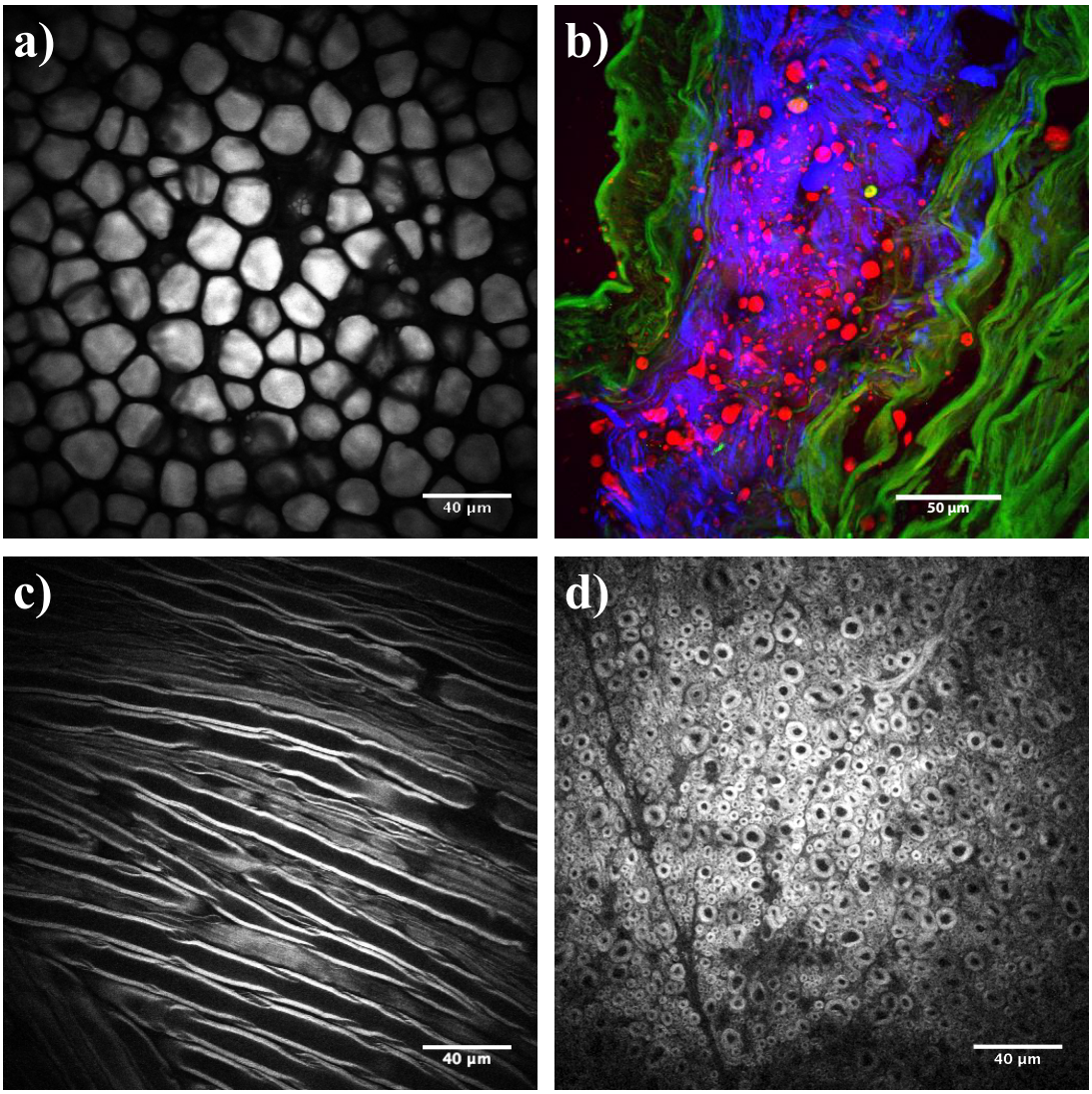

Figure 2.1 – (a) CARS image of adipocytes in freshly removed rat skin. (b) Multimodal image of rabbit aorta. Courtesy of Dr. A. Stolow. (c) and (d) Images of white matter from rat: (c) longitudinal optical section of highly oriented myelin sheaths from perfused but otherwise untouched spinal cord and (d) mechanically cut transverse section of fixed spinal cord.

action length and the large collection of wavevectors under high NA illumination (≥ 0.7), the adverse effects of phase-matching are reduced [Cheng et al., 2002c] and the signal can be emitted in the forward- and epi- directions. Large objects typically emit in the forward direction, while small objects emit equally in the forward and epi-direction [Cheng et al., 2002a,c]. In turbid samples such as tissues, the conditions are such that the signal is generated mostly in the forward direction but a significant fraction of those photons (ranging from 15% to 35% depending on tissue type) is backscattered and can be collected by the microscope objective [Evans et al., 2005], permitting *in vivo* measurements. The non-resonant contribution lacks chemical specificity and is present at all Raman shifts, reducing the sensitivity of CARS microscopy. This problem has been recognized for some time and many methods have been developed to reduce or suppress this contribution (epi-CARS for small structures [Volkmer et al., 2001], interferometric-CARS [Evans et al., 2004], time-resolved CARS [Volkmer et al., 2002], polarization sensitive detection [Cheng et al., 2001a], FM-CARS [Ganikhanov et al., 2006b]). In situations where the non-resonant background is detrimental, FM-CARS is probably the most notable approach since it increases the sensitivity by 3 orders of magnitude over conventional systems. It requires two pairs of pulses, each on- and off-resonance. Phase-locked detection of the rapid modulation between on- and off-resonance removes the slowly varying non-resonant contribution. However, the most important aspect of CARS imaging is that the coherent signal depends on the square of the molecular density. This is both a blessing and a curse: for large enough densities, the signals are nearly as high as fluorescence. On the other hand, this coherent dipole emission with resonant and non-resonant contributions results in the CARS spectra not matching the spontaneous Raman spectra, making quantitative analysis more difficult than for other techniques (e.g., fluorescence, spontaneous Raman) [Vartiainen et al., 2006]. Lipid membranes turn out to be easily imaged based on contrast from the CH_2 stretch vibration. This has brought about many applications of CARS microscopy in neurosciences: myelin, the white matter of the nervous system, originates from the wrapping of oligodendrocytes or Schwann cell membranes around axons. By tuning the contrast to the CH_2 stretch vibration at 2845 cm^{-1}, it is possible to image myelin without exogenous contrast agents. The first demonstration of myelin imaging with CARS was reported by Wang *et al.* [Wang, 2005]. They showed CARS images of myelin in fresh spinal cord tissue excised from a guinea pig. Since then, multiple studies have been undertaken in live animals, by our group and others, to study demyelination pathologies. For example, we have used *in vivo* CARS microscopy to observe multiple sclerosis-like lesions in an animal model (experimental autoimmune encephalomyelitis (EAE)), as shown in Fig. 2.2. The figure shows the tubular myelin in the dorsal root of the spinal cord (a) and in the dorsal column (b) of an EAE animal. Lesions are clearly seen on the dorsal column (part of the central nervous system), whereas the dorsal roots (part of the peripheral nervous system) are spared as expected from the nature of the disease. In the dorsal root, the myelin sheaths are organized on a large scale and well aligned, and present morphological structures such as a node

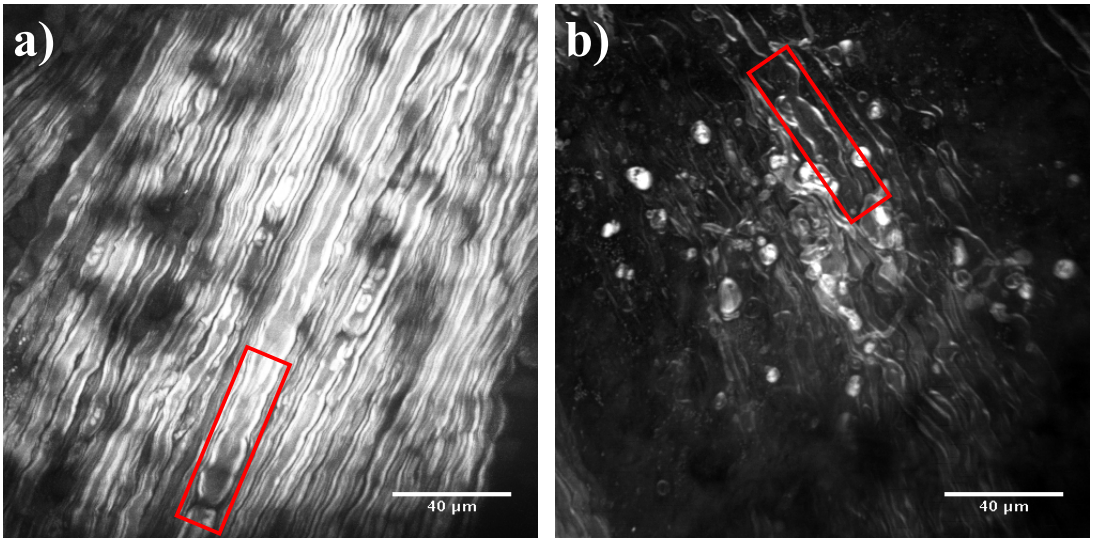

Figure 2.2 – *In vivo* CARS microscopy images of myelin from the spinal cord of EAE mice showing (a) intact myelin sheaths in the dorsal root (part of the peripheral nervous system), and (b) demyelinated regions in the dorsal column (part of the central nervous system). The differences are most apparent in the indicated areas.

of Ranvier. However, demyelinated regions, called plaques, and small lipid-filled spherical structures are seen in the dorsal column. Preliminary results demonstrate that those structures are probably fragmented myelin sheaths undergoing phagocytosis by macrophages.

Fu *et al.* [Fu et al., 2007a] have observed lysophosphatidylcholine-induced myelin degradation in excised guinea pig spinal cord tissue. They attributed myelin swelling to membrane vesiculation and splitting, confirmed by electron microscopy. In that work, they took advantage of the polarization dependence of the CARS generation to assess, at a sub-resolution level, the membrane disruption in the degradation process. More recently, Fu *et al.* [Fu et al., 2008] reported an *ex vivo* map of an horizontal section of the whole mouse brain to illustrate the myelinated fibers in different regions (Fig. 2.3).

The sciatic nerve is a perfect candidate for *in vivo* CARS imaging since the myelinated axons in the PNS are to some extent isolated from the movement induced by breathing and heartbeat. CARS imaging on healthy sciatic nerve tissue has been reported for the first time in 2007 by Huff *et al.* [Huff and Cheng, 2007]. In the work by Henry and co-workers, Wallerian degeneration and remyelination can be observed over the course of weeks [Henry et al., 2009] in an animal model of crush nerve injury on Sprague Dawley rat, as displayed on Fig. 2.4. The structural organization of the myelin sheaths is partially lost above the crush site and has disappeared completely below the injury. *In vivo* images of sciatic nerve were obtained with image stabilization algorithms to correct for unavoidable animal movement, and 3D reconstructions were obtained from the image stacks. It was shown that CARS microscopy

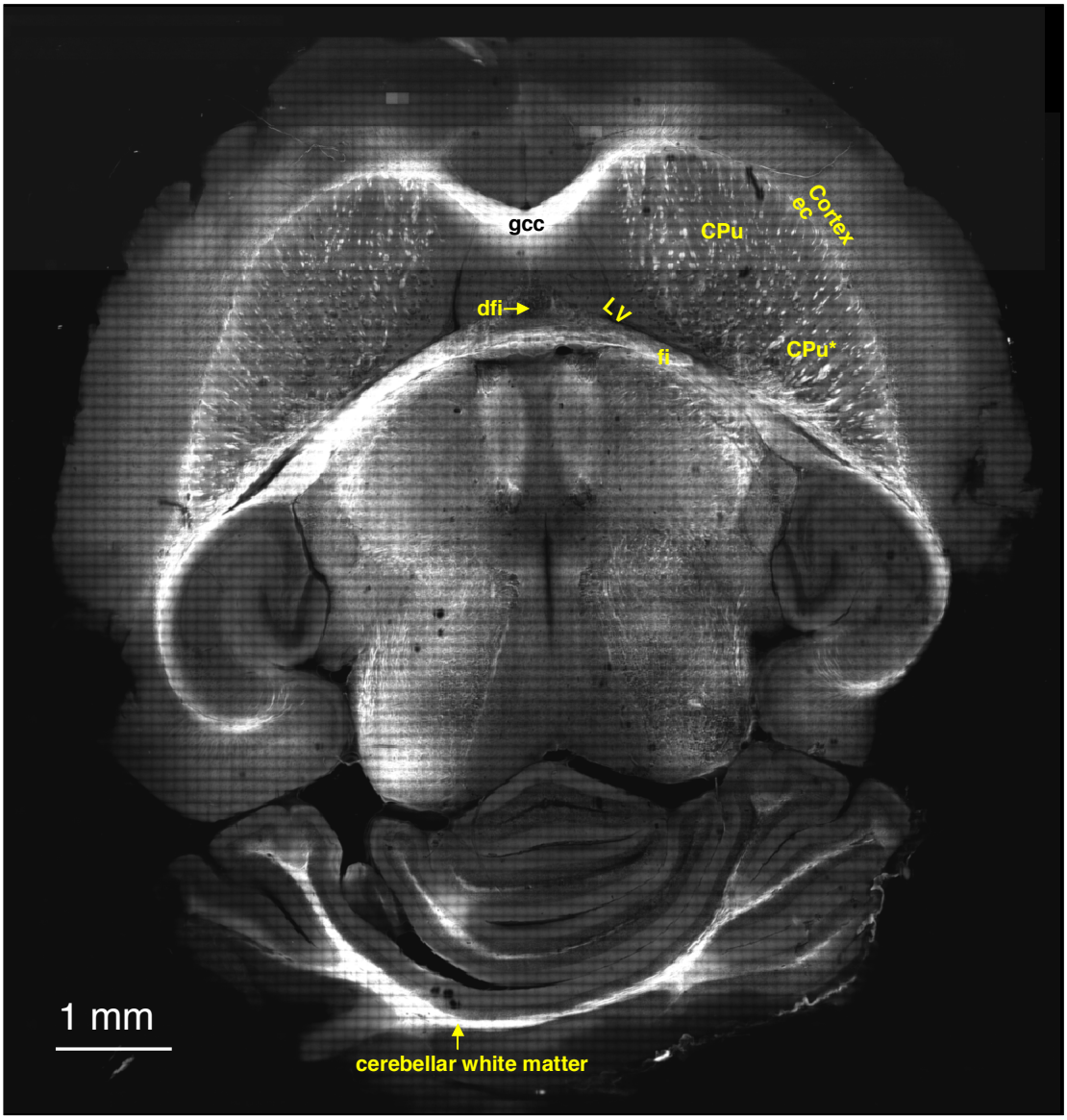

Figure 2.3 – About 10 000 CARS images were partially overlapped to create this mosaic of a horizontal slice through a mouse brain. (gcc: genu of corpus callosum, CPu: caudate putamen, ec: external capsule, dfi: dorsal fornix, fi: fimbria hippocampus and LV: lateral ventricle)

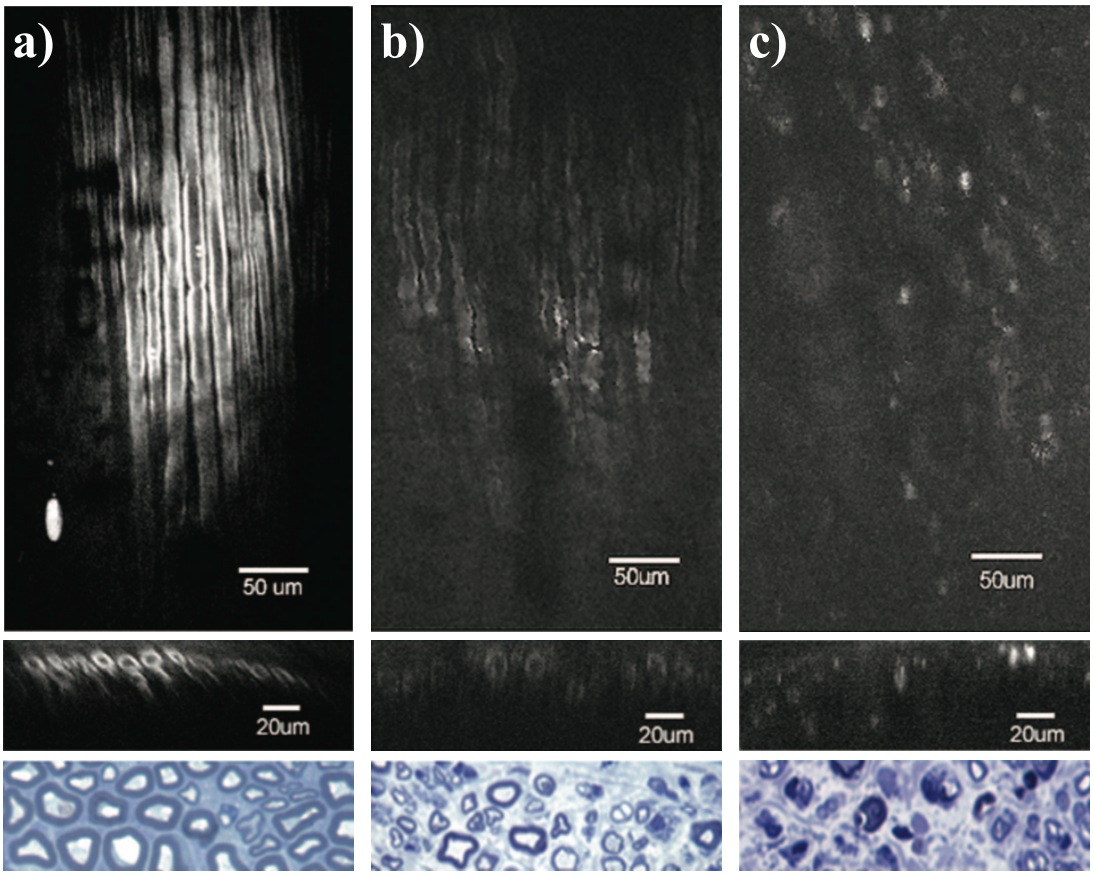

Figure 2.4 – *In vivo* CARS microscopy of a rat sciatic nerve in normal condition (a) and 2 weeks after crush injury above (b) and below (c) the crush site. The images show longitudinal section (above), cross-sections (center) and histological preparation (below) for all conditions.

could provide enough information to assess nerve health *in situ* as compared to histology.

More recently, we laid the foundation for CARS histomorphometry with a strategy that minimizes the intensity modulation of the images due to polarization. Although a solution has been suggested in the past [Fu et al., 2008], a scheme using a single image with circularly polarized excitation beams makes the image more homogenous and more readily used with standard image analysis tools [Bélanger et al., 2009b]. In order to perform histomorphometric analysis on large areas, techniques are being developed to automate the measurements.

Based on reconstructed orthogonal 3D views perpendicular to the parallel running axons (as illustrated in Fig. 2.5(a), also referred to contact-free CARS optical slice, an histomorphometric analysis has been conducted. Figure 2.5(b) relates the myelin area to the fiber diameter and shows that the probed axons are in a non-pathological state since no splitting or y-shaped distribution is observed. Finally, the scatter diagram of the g-ratio (ratio of inner to outer diameter) versus the axon caliber (Fig. 2.5(c)) reveals variations in g-ratios between

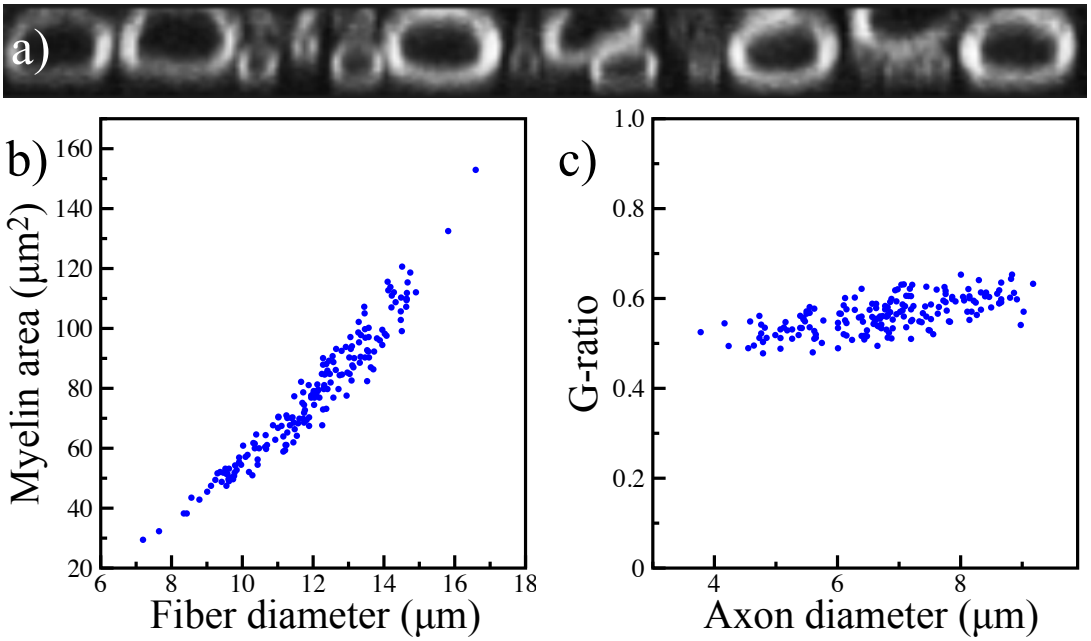

Figure 2.5 – (a) Contact-free CARS optical slice of live white matter from rat spinal cord tissue. (b) Scatter diagram of myelin area to the fiber diameter. (c) Scatter diagram of the g-ratio versus the axon caliber.

0.5 and 0.65 and a minor trend to increase with the axon caliber. This histomorphometry technique is currently being used for quantifying the early stages of multiple sclerosis in our group.

Apart from neuroscience applications, CARS microscopy has also been used to explore a variety of cancers. In particular, CARS has revealed the gross anatomy of the brain based on variations in the white matter content of healthy coronal sections of mice brain [Evans et al., 2007]. In the same paper, CARS was used on a mouse model of brain tumor to highlight the tumor margins with an accuracy comparable to the gold standard in histopathology (Fig. 2.6). The tumor contrast is produced by the absence of normal white matter in the tumor region as compared to the rest of the brain.

Obesity is known to be a risk factor for breast cancer incidence. The combination of SHG and CARS microscopy, in an early-onset of diet-induced obesity breast cancer animal model, has been used to assess the impact of obesity on the biochemical constitution of mammary glands and tumor stroma [Le et al., 2007]. The authors have shown that the size of the adipocytes in the mammary glands and the collagen content present in tumor stroma increase with the progression of the disease indicating that obesity produces an environment that facilitates the tumorgenesis. Also, a study on the impact of a high fat diet on cancer development has revealed an early detection of circulating tumor cells in the blood stream by intravital flow cytometry, increased lung metastasis and a polarized distribution of lipid droplets in the

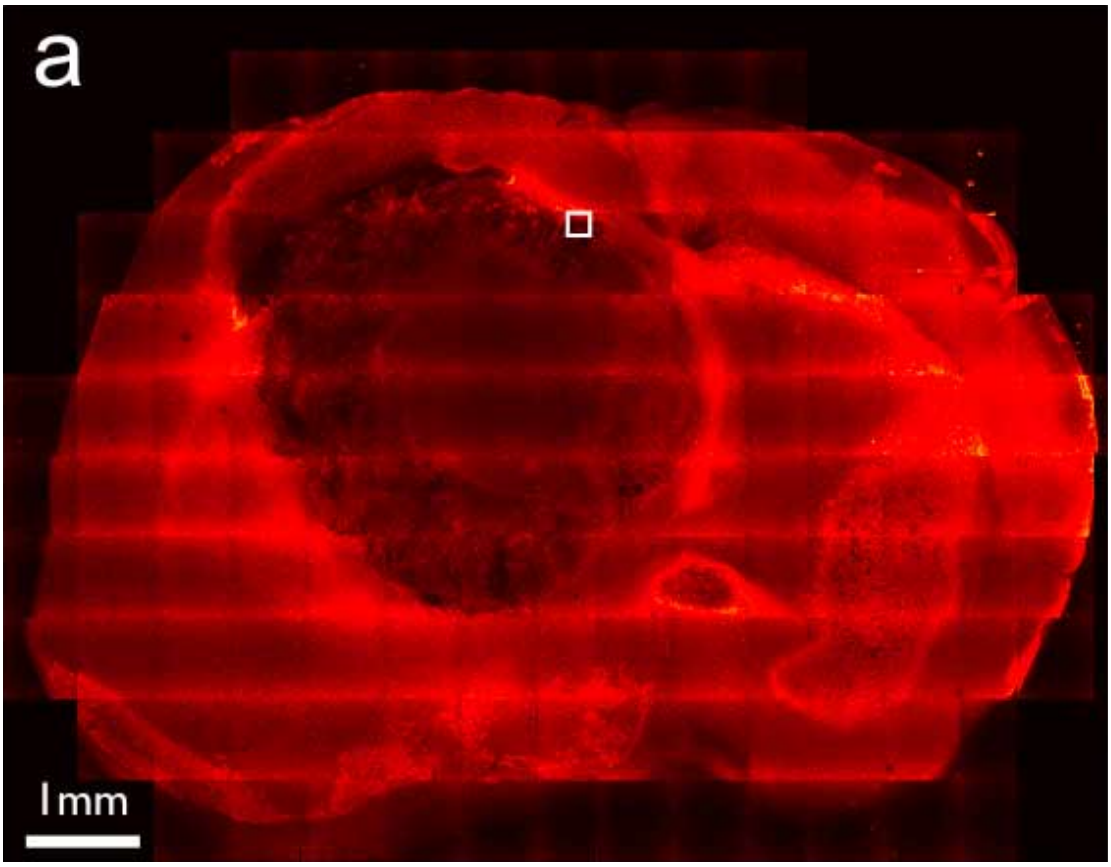

Figure 2.6 – A low resolution mosaic CARS microscopy image of a SCID mouse brain. This image demonstrates the ability of CARS to identify the boundary between healthy tissue and the tumor (astrocytoma).

circulating tumor cells [Le et al., 2009].

In conclusion, CARS microscopy provides excellent contrast for lipid imaging with minimal non-resonant background. This makes it an excellent modality for monitoring remodeling of myelinated tissues in the nervous system. However, the non-resonant background and the quadratic dependence on density become problematic for weaker lines of interest, such as protein or phosphate bands. Stimulated Raman scattering may overcome these issues.

2.4.2 Stimulated Raman scattering

Stimulated Raman scattering (SRS) is another Raman-based multiphoton technique with vibrational specificity and a sensitivity comparable to CARS [Ozeki et al., 2009]. Briefly, SRS requires the spatial and temporal superposition of two laser beams with a frequency difference matching that of a molecular vibration. When this condition is fulfilled, photons from the pump beam are depleted (stimulated Raman loss, (SRL)) leading to an increase of the number of photons in the Stokes beam (stimulated Raman gain). Detecting this modulation

in either beams provides contrast based on the vibration. Recently demonstrated for biological imaging by Freudiger *et al.* [Freudiger et al., 2008] and Nandakumar *et al.* [Nandakumar et al., 2009], it alleviates some of the key difficulties associated with CARS microscopy and spectroscopy. First, the signal intensity is linear with the intensity of both excitation lasers and with the concentration of Raman active molecules within the focal volume allowing simple quantitative analysis. Second, there is no non-resonant background and the signal follows the Raman spectrum, increasing the image contrast and removing the distorted line shape present in a CARS spectrum (see Fig. 2.7). Finally, the spatial resolution of SRS can be

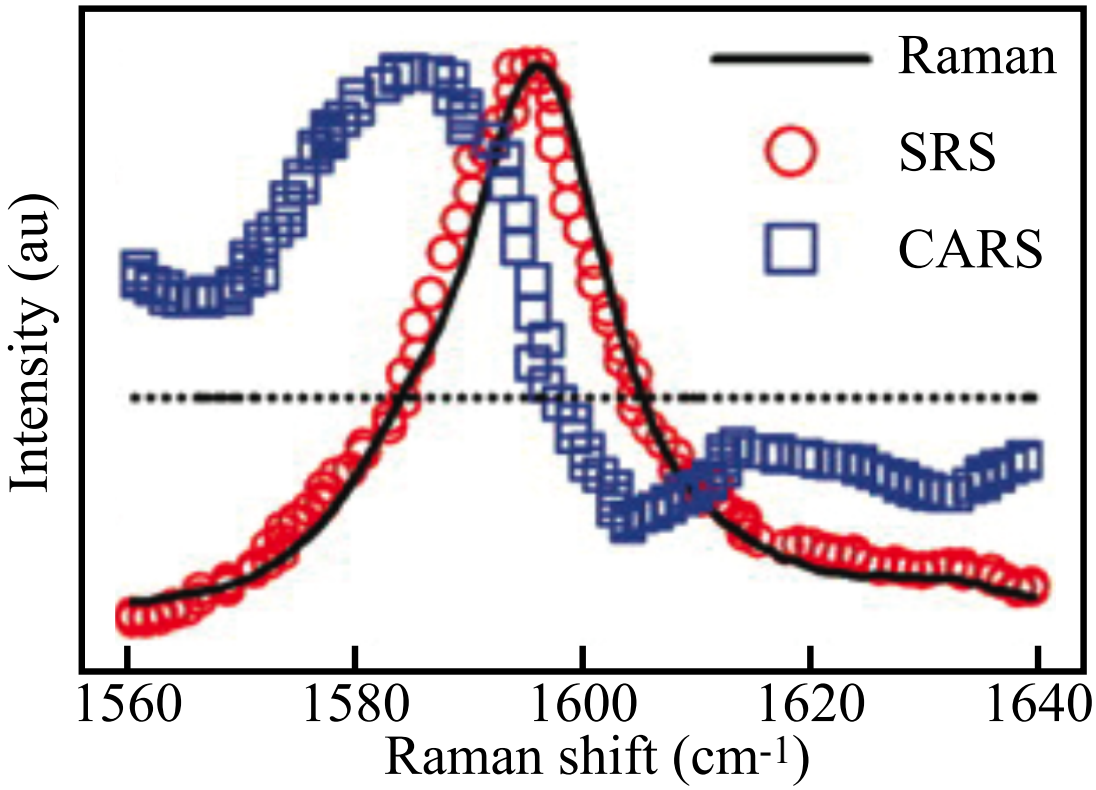

Figure 2.7 – Agreement of SRL spectrum (red circles) with the spontaneous Raman spectrum (black line) of the Raman peak (1595 cm^{-1}) of 10 mM retinol in ethanol. The distorted CARS spectrum (blue squares) exhibits a typical peak shift, dispersive shape and non-resonant background.

expressed in terms of the point spread function of the imaging system, allowing image deconvolution similar to what is done in fluorescence microscopy [Potma et al., 2000], in stark contrast with CARS microscopy [Hagmar et al., 2008].

Experimentally, contrary to CARS microscopy where sensitive photon counter detectors are needed, SRS microscopy requires detectors with a high dynamic range to detect the small intensity modulation at the wavelength of either excitation lasers. This can be achieved by modulating one of the two excitation beams and detecting the gain (or loss) experienced by

the other beam by way of a lock-in detection. The first report of SRS imaging used a low repetition rate amplified femtosecond laser system with an array of photodiodes for multiplex detection [Ploetz et al., 2007]. However, the long pixel dwell time and high peak power of their system is limiting for bioimaging. More recently, the Xie group reported on a system similar to that used for CARS microscopy based on an OPO synchronously pumped by a picosecond infrared laser [Freudiger et al., 2008]. Fast modulation (1.7 MHz) of the Stokes beam and phase sensitive detection with a high frequency lock-in amplifier enabled the acquisition of the stimulated Raman loss signal from fresh mouse tissue with a pixel dwell time of only 170 μs. Since then, other groups have followed suit with different laser sources [Ozeki et al., 2009, Nandakumar et al., 2009]. However, the great potential of SRS for tissue imaging has been described in the paper by Freudiger *et al.* [Freudiger et al., 2008] where the authors showed the imaging capabilities of SRS on fresh mouse tissue with different Raman lines (lipids, DMSO, retinoic acid). Of particular interest to neurosciences, images of neuron bundles from thin and thick slices of mouse corpus callosum were acquired. The authors also demonstrated the technique's ability to observe the distribution of retinoic acid in tissue, a drug used for treating skin disorders, in tissues. Finally, the potential of SRS for cancer identification or margin detection in the brain is demonstrated in Fig. 2.8. The large, irregularly

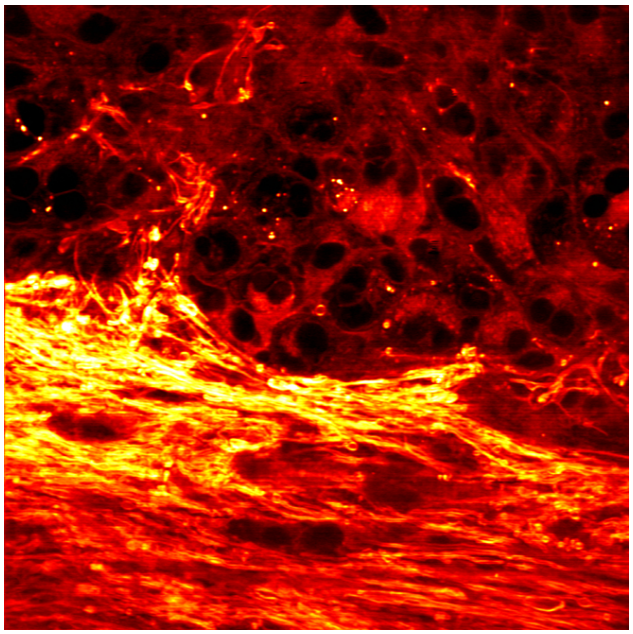

Figure 2.8 – The SRS image covering 200 $\times$ 200 μm provides lipid contrast based on the molecular signature of CH_2 groups, which allows the healthy tissue (bottom) to be distinguished from the lipid poor tumor (top). Courtesy of C. Freudiger, Dr. G. Young, Dr. S. Kesari and Prof. X. S. Xie.

shaped nuclei of the cells visible in the tumor region, are an important diagnostic marker.

2.4.3 Outlook on imaging

In general, the use of these rapid imaging techniques provides excellent context for measurements of a *single* biochemical species in tissue, but the amount of spectroscopic information is limited compared to spontaneous Raman spectroscopy. For instance, with spontaneous Raman spectroscopy it is possible to determine that the cholesterol content unexpectedly climbs as the tissues advances from healthy to malignant in both bladder and prostate (Fig. 2.9) [Stone et al., 2007], or that there is an increase in the level of glycogen in squamous area and an augmentation of DNA levels in abnormal regions of the esophagus [Shetty et al., 2006]. Bringing the level of endogenous specificity from vibrational spectroscopy to rapid high spatial resolution imaging in native tissue with the use of CARS or SRS spectroscopy still represents the holy grail of endogenous tissue spectral imaging.

2.5 Towards *in vivo* spectral imaging

The first efforts towards *in vivo* spectral imaging have been reported by the Feld group on human breast tissue [Shafer-Peltier et al., 2002]. Spontaneous Raman spectral images were acquired at a rate of 1 frame per 3.5 hours or 20 seconds per pixel for a range of healthy and diseased breast tissues, and relative concentrations of tissue constituents were extracted from the spectra using a least-squares fitting algorithm on reference spectra. Although some advances have since then made the acquisition times an order of magnitude faster [Hutchings et al., 2009], it is still much slower than what CARS and SRS could potentially offer: as was shown in the imaging section earlier, pixel dwell times as small as 100 ns are possible for imaging a single Raman line, which could translate in millisecond acquisition times for full spectra. The experimental realization of CARS spectral imaging can follow two strategies: broadband (or multiplex) and narrowband. In the broadband scheme, a spectrally narrow pump beam is combined with a broadband laser beam to simultaneously excite numerous Raman lines, thereby giving rise to a range of anti-Stokes photons covering the various vibrations. The detection of the anti-Stokes light is carried out with a spectrometer, usually a CCD-based imaging spectrometer for faster acquisition. In one of the first microspectroscopy experiment, appropriate pump and Stokes beams were obtained by synchronizing a picosecond laser with a broadband femtosecond laser (80 fs) giving simultaneous access to Raman bandwidths over 400 cm^{-1} with pixel dwell times ranging from 50 ms to 200 ms [Cheng et al., 2002b, Müller and Schins, 2002]. By monitoring the high wave number region between 2800 and 3100 cm^{-1}, it was shown that the gel and crystalline states of lipid bilayers can be differentiated. One can also make use of a single laser where the broadband Stokes beam is generated via a number of nonlinear processes (mostly self-phase modulation) from ultrashort pulses focused into specialised fibers. In the picosecond regime, a system using a homemade 1064 nm laser source and an optical fiber with a high GeO_2 content core (UHNA3) or a photonic crystal fiber has been described by Petrov *et al.* [Petrov and Yakovlev, 2005]. In

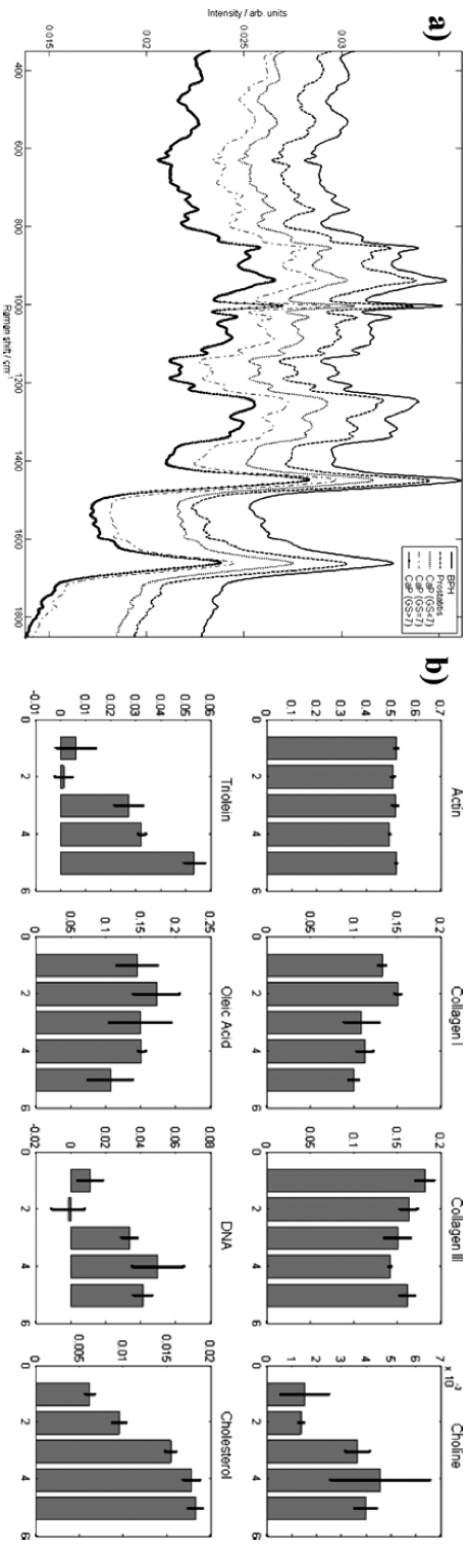

Figure 2.9 – Example of spectroscopic content obtained from Raman spectroscopy. Mean spectra for each prostate pathology (a) and the relative concentration of each individual constituent (b) for each pathology. (1 = benign prostate hyperplasia; 2 = prostate inflammation; 3–5 = low, moderate and high grades of prostate cancer) [Stone et al., 2007].

the femtosecond regime, Kee *et al.* [Kee and Cicerone, 2004] produced a spectrally narrow pump beam by filtering a femtosecond pulse and then launching the remaining power into the core of a tapered nonlinear fiber to create a continuum. The system was used to acquire broadband CARS spectra of benzonitrile with a 17 ms integration time leading to frame rates on the order of a few minutes for images of 256 $\times$ 256 pixels, about 5 orders of magnitude slower than state of the art, single-line narrowband CARS imaging system [Evans et al., 2005] but much faster than typical spontaneous Raman spectroscopy. In another example, variations in the ordering of acyl-chains and the composition of lipid droplets in the skin have been investigated using multiplex CARS spectral images [Rinia et al., 2008] (Fig. 2.10).

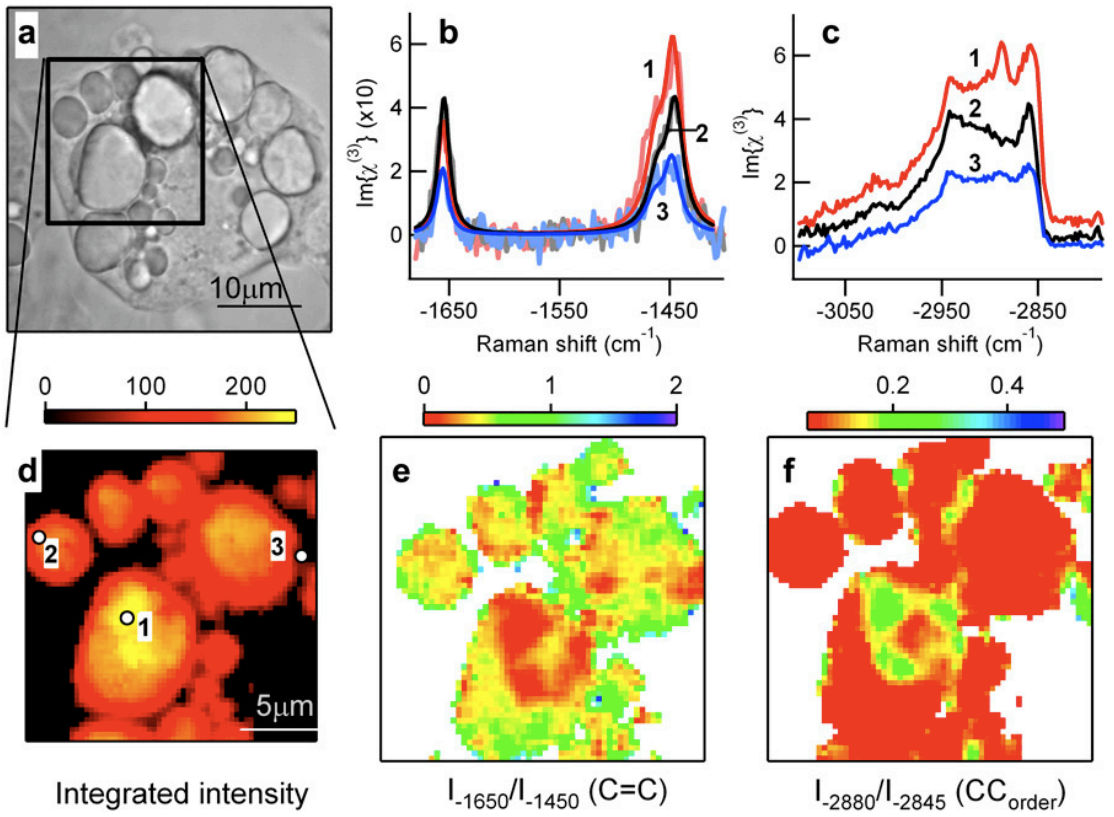

Figure 2.10 – Bright-field (a) and multiplex CARS spectral image (d) of an adipocyte. The spectral image is reconstructed from multiplex CARS spectra ((c) and (d)) acquired in 20 ms for every pixel. The images (e) and (f) represent the C=C concentration and the degrees of acyl-chain order respectively [Rinia et al., 2008].

The major drawbacks of this broadband CARS approach are related to the quality of the continuum (power levels, smoothness, stability, reproducibility, etc.), the presence of non-resonant background that must be removed with post-analysis, the relatively high power impinging on the sample because of the continuum that may cause nonlinear photodamage, and finally the necessity to use an imaging spectrometer that does not efficiently collect light from diffuse sources. The second approach to CARS spectroscopy consists in excit-

ing the Raman lines sequentially with narrowband excitation beams. This method has been successfully implemented with synchronized picosecond Ti:Sapphire lasers [Wang, 2005] or Nd:Vanadate laser pumping an OPO [Evans et al., 2005], but the long time associated with the manual tuning of the Stokes beam is problematic for *in vivo* applications. However, such a strategy does overcome key issues associated with the broadband strategy: much less non-resonant background, lower average power on the sample and no need for spectrally resolving the emitted light. SRS spectroscopy can also be performed with a narrowband excitation scheme, although it faces the same technological limitations as CARS: rapidly (kHz) tunable narrowband picosecond sources are not available commercially. A clever hybrid approach applicable to CARS spectroscopy was recently developed independently by two groups. While using two broadband femtosecond pulses would normally prevent high spectral resolution, the use of two identically chirped femtosecond pulses recovers the spectral resolution and permits tunability with the change of temporal delay between the pulses (see Fig. 2.11) [Hellerer et al., 2004, Pegoraro et al., 2009]. This technique has the key advantage

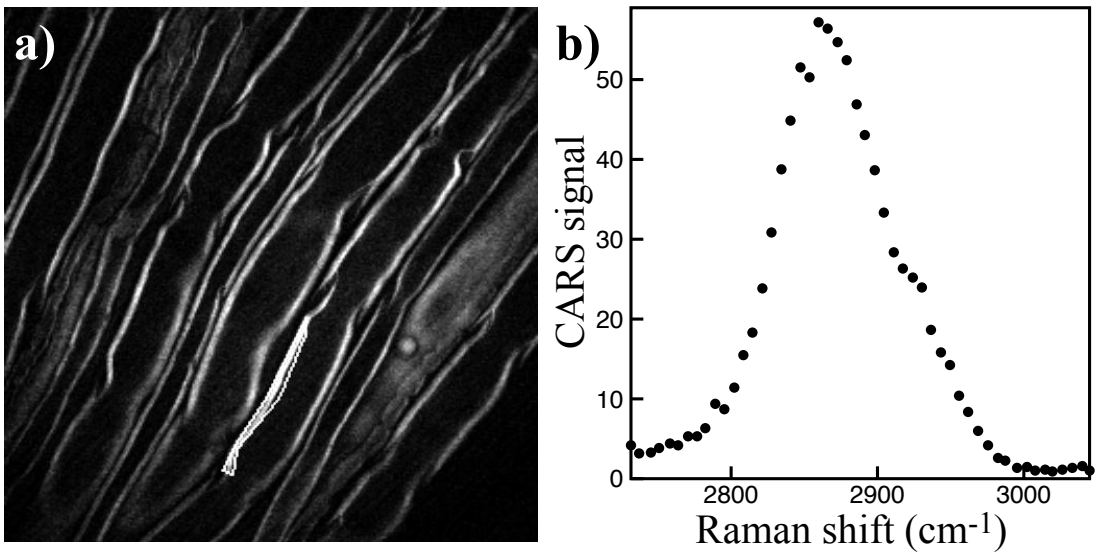

Figure 2.11 – (a) CARS image of a myelinated nerve fiber with an outline drawn around a region of interest where the myelin density is high. (b) Myelin spectrum derived from the average intensity within the region of interest. Courtesy of Dr. A. Stolow

of being compatible with standard multiphoton laser sources (Ti:Sapphire lasers) and permits both imaging and spectroscopy with the same setup.

A comparison between spontaneous Raman and CARS spectral imaging of colon tissue has been performed [Krafft et al., 2009a]. They demonstrated striking resemblance between spontaneous Raman and CARS microscopy of colonic polyps. In addition, they observed similarities between Raman and CARS spectra of colonic polyps colon tissue, suggesting that the changes in the biochemistry of cancer tissues can be precisely unraveled with CARS.

This implies that a direct correspondence with the extensive Raman literature is possible.

While coherent Raman spectroscopy techniques are not yet adequate for *in vivo* experiments, spontaneous Raman spectroscopy can be used to complement CARS imaging with good success. Recently, a system combining single-line CARS imaging for rapid tissue survey with spontaneous Raman for subsequent spectral analysis at points of interest has been described [Slipchenko et al., 2009], but is still limited by the long acquisition times of confocal Raman.

In summary, broadband approaches have had some success in spectral imaging, but key limitations persist: 1) the quality of the broadband light is still problematic, 2) the diffuse light source in tissue is not efficiently collected by imaging spectrometers, 3) relatively high power and long integration time may lead to nonlinear photodamage and 4) the presence of non-resonant background. On the other hand, narrowband approaches avoid these problems, but must presently rely on slow wavelength tuning because rapidly and broadly tunable, synchronized picosecond light sources are not commercially available. This makes them poorly optimized for *in vivo* spectral imaging.

2.6 Conclusion

This manuscript discussed the use of Raman-based techniques for imaging and characterizing tissue during the course of diseases or injuries. Coherent Raman imaging was highlighted with many applications in neuroscience because of its excellent contrast for myelin due to the importance of lipid content. Examples included *in vivo* monitoring of Wallerian degeneration of the peripheral nerve and observation of demyelinating lesions due to multiple sclerosis. In addition, stimulated Raman scattering was also discussed because it avoids two common problems of CARS imaging, namely non-resonant background and quadratic dependence on density, and may allow imaging of other Raman lines of interest in the fingerprint region. The combination of these imaging techniques for complete vibrational spectroscopy (spectral imaging) was also discussed: spectral imaging with broadband CARS spectroscopy is possible and examples in cell biology were highlighted but it suffers from non-resonant background and non optimal light sources. Narrowband wavelength-swept spectroscopy (both CARS and SRS) on the other hand is currently limited by the availability of rapidly tunable light sources and hence have seen limited *in vivo* applications, but as technology evolves, applications to *in vivo* spectral imaging will become more important.

Chapter 3

Coherent anti-Stokes Raman scattering hyperspectral tissue imaging with a wavelength-swept system

S. Bégin,[1,2] B. Burgoyne,[3] V. Mercier,[3] A. Villeneuve,[3] R. Vallée[2] and D. Côté[1,2]

[1]Centre de Recherche Université Laval Robert-Giffard (CRULRG), Université Laval,
Québec, QC, G1J 2G3, Canada
[2]Centre d'Optique, Photonique et Laser (COPL), Université Laval,
Québec, QC, G1V 0A6, Canada
[3]Genia Photonics Inc., 1111 Lapierre St.,
Lasalle, QC, H8N 2J4, Canada

3.1 Résumé

Nous présentons un système d'imagerie hyperspectral par diffusion Raman cohérente (CARS) à longueur d'onde balayée (WS-CARS) pour utilisation dans les tissus épais. Nous avons développé une stratégie où les lignes Raman sont excités de manière séquentielle ne nécessitant pas de spectromètre. Ce système laser à fibre, constitué d'un laser de pompe synchronisé avec un laser programmable rapidement accordable, peut accéder aux vibrations Raman sur une plage importante de la région des hauts nombres d'ondes (2700-2950 cm^{-1}) à une vitesse maximale de 10,000 éléments spectral par seconde. Pour démontrer les capacités du système, nous avons enregistré des spectres CARS de plusieurs échantillons ainsi que des images et des images hyper-spectrales de tissu épais en détection vers l'avant et vers l'arrière. Cet instrument devrait être particulièrement utile en fournissant des informations biochimiques locales avec le contexte environnant fournie par l'imagerie.

3.2 abstract

We present a wavelength-swept coherent anti-Stokes Raman scattering (WS-CARS) spectroscopy system for hyperspectral imaging in thick tissue. We use a strategy where the Raman lines are excited sequentially, circumventing the need for a spectrometer. This fibre laser system, consisting of a pump laser synchronized with a rapidly tunable programmable laser (PL), can access Raman lines over a significant fraction of the high-wavenumber region (2700-2950 cm^{-1}) at rates of up to 10,000 spectral points per second. To demonstrate its capabilities, we have acquired WS-CARS spectra of several samples as well as images and hyperspectral images (HSI) of thick tissue both in forward and epi-detection. This instrument should be especially useful in providing local biochemical information with surrounding context supplied by imaging.

3.3 Introduction

Raman based spectroscopy techniques are highly sensitive to the biochemical nature of materials and have the high spatial resolution associated with optical microscopy. Fast identification of biochemical components in turbid materials has generated strong interest in live tissue spectroscopy since it makes disease diagnosis possibly achievable *in situ*. For example, the diagnostic potential of Raman spectroscopy has generated a large amount of literature in oncology alone [Kendall et al., 2009, Krafft et al., 2009c]. However, it has become clear that a clinically useful technique should also provide context for diagnosis through imaging, something impossible with low sensitivity techniques such as spontaneous Raman spectroscopy.

Coherent anti-Stokes Raman scattering [Duncan et al., 1982, Zumbusch et al., 1999b] is a nonlinear technique with the necessary sensitivity for fast chemically-specific imaging. It requires two or more laser pulses of different wavelengths to coherently excite a Raman active vibrational mode in a molecule. On the one hand, the nonlinear nature of the process demands short pulses (ps or fs) with high peak power, and on the other hand a system with good tunability or a large bandwidth is necessary for spectroscopic measurements. Typical CARS systems based on optical parametric oscillators [Evans et al., 2005, Ganikhanov et al., 2006a] or synchronized Ti:Sapphire lasers [Potma et al., 2002, Evans et al., 2004] have been successful for imaging lipids, myelin and water [Zumbusch et al., 1999b, Bélanger et al., 2009b] (for a review see [Evans and Xie, 2008]) but their relatively slow tunability has hampered their use in spectroscopy. Broadband methods based on transform-limited ultrashort pulses [Cheng et al., 2002b, Müller and Schins, 2002, Selm et al., 2010] or continuum generation [Kee and Cicerone, 2004] have been successful for spectral imaging of optically thin systems. However, their need for a spectrometer to resolve the vibrational spectra results in very poor collection efficiency in turbid materials such as tissue where diffusion is important. Methods using spectral focussing of broadband excitation pulses avoid the need for a

spectrometer but rely on a mechanical delay line for vibrational tuning [Pegoraro et al., 2009, Langbein et al., 2009, Chen et al., 2010].

We propose a strategy where the Raman lines are excited sequentially at very high speed by narrowband picosecond pulses. The wavelength-swept coherent anti-Stokes Raman scattering system presented here is based on a master oscillator power amplifier (MOPA) pump laser synchronized with a rapidly tunable programmable laser (PL) as the Stokes beam. The spectral bandwidth of this instrument covers most of the high wavenumber region (2700-2950 cm^{-1}). This strategy has many advantages compared to other existing methods. With the spectroscopic information encoded in time (Fig. 3.1(a)), the detection can be done using fast and sensitive photomultiplier tubes. This is especially important for CARS spectroscopy in thick tissue where the large étendue of the scattered signal is not compatible with the small entrance slit of spectrometers, resulting in poor collection efficiencies. Furthermore, this system allows random access to any Raman line within its bandwidth. Since the acquisition time scales linearly with the number of spectral points, this should prove to be an essential feature for applications where speed is critical. Finally, the high flexibility of the wavelength sweep rate can easily accommodate rapid single point spectroscopy or hyperspectral imaging where a whole image is acquired for every Raman line (Fig. 3.1(b)). In this manuscript, we use the system for WS-CARS spectroscopy as well as single-line and hyperspectral imaging in thick tissue both in forward and epi-detection.

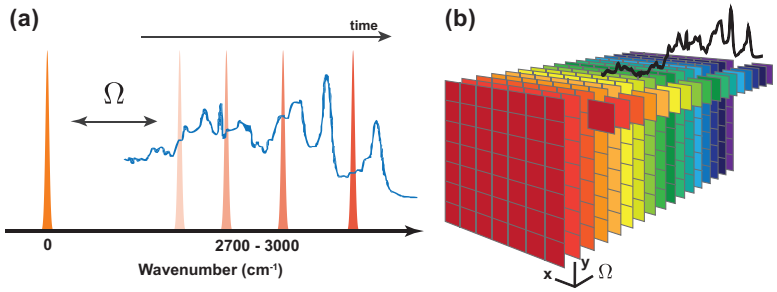

Figure 3.1 – (a) In wavelength-swept CARS spectroscopy, the Raman vibrations (Ω) are excited sequentially and the spectroscopic information is encoded in time. (b) Hyper spectral images are constructed by raster scanning of the sample for every Raman line. Every pixel contains a CARS spectrum.

3.4 Materials and methods

3.4.1 Synchronized fibre lasers system

The synchronized fibre lasers system presented here has characteristics tailored specifically for CARS spectroscopy and hyperspectral imaging. The system is composed of a programmable laser [Burgoyne and Villeneuve, 2010] and a MOPA driven by high-speed low-jitter electronics (Fig. 3.2(a)). The key characteristic of this system is the ability of the PL to rapidly (up to

10 kHz) and arbitrarily access any wavelength in its tuning range while maintaining synchronization with the MOPA. The novel programmable laser is based on a dispersion-tuned, actively mode-locked scheme [Li and Chan, 1998]. The dispersive elements are four chirped fibre Bragg gratings (CFBG) that essentially establish different cavity lengths for each wavelength. As a consequence, the laser operates at different repetition rates depending on the wavelength. Tuning is achieved by changing the driving frequency of the electro-optic modulator (EOM) (Fig. 3.2(b)). The tuning range of the PL goes from 1524 nm (12.35 MHz) to 1608.6 nm (13.98 MHz) in steps of 0.1 nm that match the spectral line widths of the laser pulses. The modulator is driven by a 25 picosecond pulse generator triggered by the function generation circuit. A wavelength division multiplexer (WDM) is used to combine the 980 nm pump and the signal into the erbium-doped fibre. The PL is amplified up to an average power of 35 mW using an erbium-doped amplifier. The MOPA is based on a 1080 nm CW laser diode externally modulated through an EOM driven by a 25 ps pulse generator. The optical signal is filtered and subjected to three stages of amplification resulting in nominally 100 mW of average power. We note that although every wavelength of the PL has a different repetition rate it does not pose a synchronization problem since both the MOPA and the PL are driven by the same function generation electronics including an arbitrary electronic time delay. Since the delay between the pulse trains is controlled electronically, there is no need for a mechanical delay line in the microscope optical path. Both lasers generate optical pulse widths of less than 35 ps, corresponding to a CARS excitation line width of less than 0.5 cm^{-1}. The long pulses (nominally 6 times longer than ideal picosecond CARS sources) are more than compensated for by the lower repetition rate (nominally 8 times lower than high repetition rate systems) yielding peak power (or pulse energy) on the order of 240 W (8 nJ) and 85 W (3 nJ) for the MOPA and PL respectively.

3.4.2 Experimental setup description

A schematic diagram of the experimental layout is shown in Fig. 3.3. The pump and Stokes beams from the synchronized lasers are collimated independently in order to prevent two-beams nonlinear interactions [Balu et al., 2010], and recombined using a long-pass filter at 45° (Semrock, LP02-1319RS-25). The beams are sent to a homemade laser-scanning microscope which collects non-descanned light in both forward- and epi-direction configurations. A gold coated 52X/0.65NA reflecting objective optimized for IR light with cover slip correction (140 μm) is used for imaging (Edmund Optics, 25-0548-020). This objective does not suffer from material absorption since gold has a very good reflectivity in the near IR (R >98%) but is minimally affected by obscuration (16.7%) due to the Cassegrain design. Furthermore, it is free from chromatic aberration. The optical power at the sample is 40 mW and 15 mW for the pump and Stokes beams respectively ($\sim$40% of the laser output power). The forward generated CARS signal is collected by a 40X/0.8NA water immersion objective (Olympus, LUMPlanFl/IR), while the epi-detected signals returns through the illumination

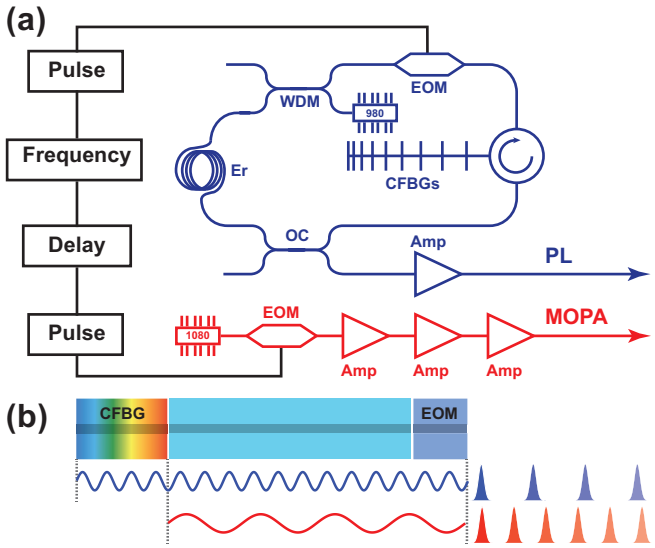

Figure 3.2 – (a) Schematic of the synchronized lasers. The PL (blue) and the MOPA (red) are driven by high-speed function generation electronics with adjustable delay (black). In the PL, the wavelength is determined by the frequency generator through dispersion tuning using four dispersive CFBGs and an EOM. The EOM is driven by a 25 picosecond pulse generator. A wavelength division multiplexer (WDM) is used to combine the 980 nm pump and the signal into the erbium-doped fibre. The MOPA consists of a CW laser diode modulated through an EOM by a 25 ps pulse generator with the same repetition rate as the PL. (b) The CFBG forms different cavity lengths for each wavelength. Tuning is achieved by changing the driving frequency of the EOM, and consequently the repetition rate of the laser.

objective. Both forward and epi CARS signals are extracted by long-pass filters used at 45° (Semrock, LP02980R-25) and filtered using combinations of two bandpass filters (Semrock, FF01-832/37-25 and Chroma, ET801/90m) before being detected by photomultiplier tubes (PMT) detectors (Hamamatsu, R3896). A homemade data acquisition system implemented in Matlab is used for WS-CARS spectroscopy experiments. ScanImage [Pologruto et al., 2003] is used for imaging and HSI experiments. For the system characterization experiments, a broadband 50/50 beam splitter is inserted in the beam path to send part of the excitation beams to a BBO crystal for sum frequency generation (SFG). The filtered (Semrock, FF01-640/14-25) SFG signal is measured using a silicon photodiode (Thorlabs, PDA36A).

3.4.3 Synchronized lasers system optimization and characterization

For every wavelength of the PL, the dispersion resulting from the laser cavities and the additional optics in the setup has to be electronically compensated to ensure temporal overlap of the pulses from both lasers at the sample. The function generation electronics triggering the lasers provide an adjustable time delay between both pulse trains. It can be tuned with high resolution delay increments (16 bits) throughout the large dynamic range of one round trip time. For example, the delay resolution at 12 MHz (83.3 ns of round trip time) is 1.27 ps.

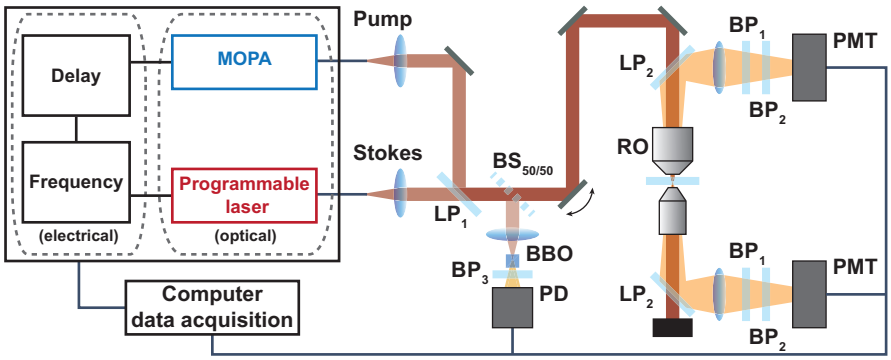

Figure 3.3 – WS-CARS microscopy setup. Pulses from the synchronized lasers are collimated separately, combined with a long-pass filter (LP_1) and then routed to a homemade laser scanning microscope. The beams are focused on the sample using a 52X/0.65NA reflecting objective (RO). The CARS signal is extracted with long-pass filters (LP_2), filtered using bandpass filters (BP_1, BP_2) and detected with PMTs in the epi- and forward- directions. A beam splitter ($BS_{50/50}$) can be inserted in the path for characterization experiments. The SFG generated in a BBO crystal is filtered (BP_3) and detected using a photodiode (PD).

In order to optimize the temporal superposition of the pulse trains, SFG is performed in a BBO crystal. The SFG signal is recorded while the time delay between the PL and the MOPA is swept at high speed (Fig. 3.4(a)). The optimal time delays are compiled in a lookup table that is used to automatically adjust the electronic delay when the PL wavelength is changed. Since the delay is controlled electronically, this can be done very rapidly (~10 ms/sweep) and in an automated fashion. The SFG delay curves are the cross-correlation of the pulses from both lasers [Potma et al., 2002]. For example, the 50 ps FWHM of the cross-correlation in Fig. 3.4(a) corresponds to about 35 ps for both laser pulses. This result is confirmed by the autocorrelation of the MOPA pulses (not shown). The pulse widths of the PL remain constant across the whole tuning range except for a slight broadening caused by a lower gain at the upper end of the range. The inset shows the SFG signal fluctuations at the half-maximum time delay over the course of 60 seconds. Since these fluctuations are due to both the timing jitter and power fluctuations in the MOPA and PL, we can set an upper limit of 2.4 ps on the timing jitter from the measurement. The signal is measured through a 1.9 MHz low-pass filter and sampled at 5 MHz to avoid aliasing problems and averaged over 1 ms.

The key feature of this system is its ability to rapidly and arbitrarily change the wavelength difference between the two lasers while maintaining synchronization and temporal overlap at the sample. This is demonstrated in Fig. 3.4(b) which shows wavelength sweeps for 3 different tuning rates (20 μs/step, 100 μs/step and 1 ms/step). The resulting SFG spectra cover the whole 84 nm tuning range with a resolution of 1 nm. SFG is a better indicator of CARS efficiency than average laser power since it depends directly on the nonlinear mixing of the pulses as can be seen by comparing SFG (lines) and PL power spectra (black diamonds). The SFG signal level is constant from 1525 nm to 1560 nm and then progressively drops

due to the lower gain of the PL amplifier at higher wavelengths as well as inefficiencies of the BBO crystal. This will translate into lower CARS efficiencies for spectroscopy at longer wavelengths, as will be shown in Fig. 3.6 and 3.7. The sweep consistency is maintained as the sweeping rate increases, showing only some slight variations at 100 μs/step and some degradation at 20 μs/step. At rates of 1 ms/step and slower, the shapes of the spectra are identical and highly repeatable. The ripples in the spectra are caused by the transfer function of the PL optical components, especially the chirped fibre Bragg gratings.

Fig. 3.4(c) shows a typical SFG time series (blue) highlighting the PL cavity dynamics following wavelength changes at 50 μs/step (black). The actively mode-locked operation is usually established in 15 μs (red) but may require more time at longer wavelengths near the end of the tuning range. For this reason, we operate the PL at tuning rates of 100 μs/step or slower, discarding the first 15 μs of acquired data. This dead time is a result from the erbium-doped fibre gain dynamics and could be overcome using other gain media such as semiconductor optical amplifiers.

Fig. 3.4(d) shows an epi-CARS image of a thin-film interface of water (which does not contain C-H bonds) and peanut oil acquired at 2850 cm^{-1} (PL tuned to 1560 nm). The 4% signal-to-background ratio from the average line profile yields an upper limit to the nonresonant background contribution. In fact, most of the background signal comes from the PMT dark noise and a small leakage of the pump laser through the optical filters. This small nonresonant contribution is explained by the 35 ps pulse length [Cheng et al., 2001b], since the non-resonant background decreases for increasing pulse widths.

3.5 Results and discussion

3.5.1 CARS imaging

The imaging capabilities of the WS-CARS microscope are demonstrated on a mouse ear. The adipocytes are clearly visible in both the forward- (Fig. 3.5(a)) and epi-detected (Fig. 3.5(b)) images. This epi-detection capability is a direct consequence of the wavelength-swept strategy that removes the necessity of using a spectrometer for collection and permits an efficient collection of all the CARS photons with a large area PMT. The anti-Stokes signal in the images comes from the symmetric CH_2 stretching mode of the lipids present in the structures approximately 80 μm deep in the skin. The images are an average intensity projection of 10 frames acquired in a total of 7.5 seconds.

3.5.2 WS-CARS spectroscopy

The wavelength-sweep mode is used for single point spectroscopy by rapidly tuning the PL and recording the anti-Stokes signal. The maximum spectral resolution of the system is

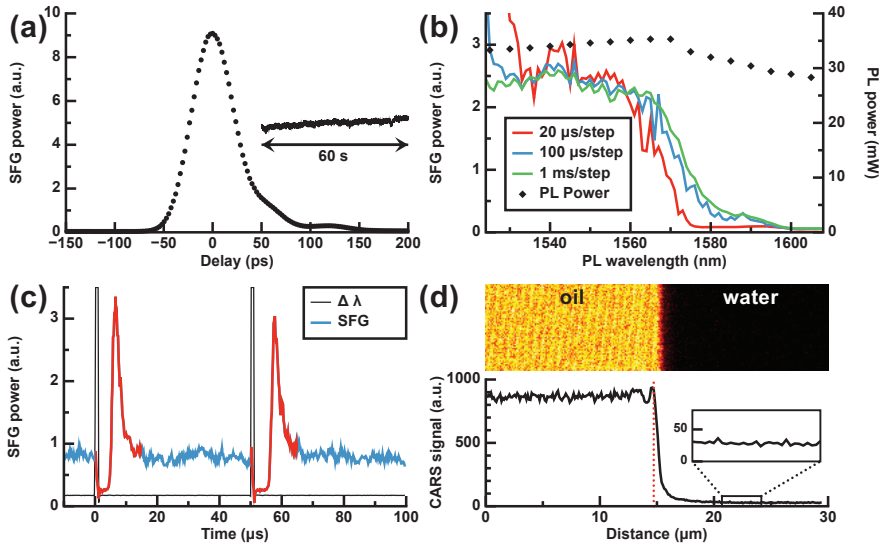

Figure 3.4 – (a) Typical cross-correlation trace between the PL and the MOPA, used to calibrate the temporal overlap of the pulses at the target and to characterize their pulse widths. The delay sweep acquired at a rate of 50 μs/step (λ_{PL} = 1560 nm, total time = 7.5 ms). Inset shows the half maximum SFG signal recorded over 60 seconds. (b) SFG spectra acquired at different sweep rates are highly repeatable. The diamond curve indicates the power spectrum of the PL. (c) SFG time series (blue) reveals the PL cavity dynamics following wavelength changes (black). The stabilization period (red) typically lasts 15 μs. (d) CARS image of the interface of a water-oil thin film indicates that the non-resonant background is at most 4%.

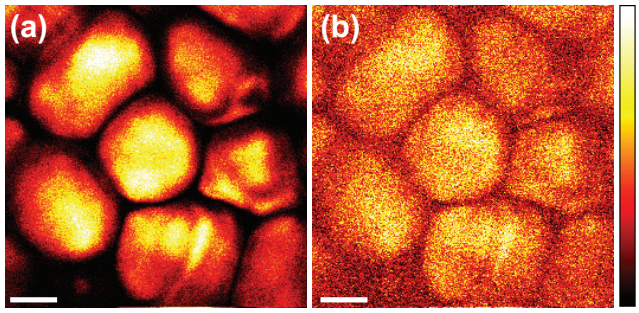

Figure 3.5 – *Ex vivo* CARS images of adipocytes in a 1-mm-thick mouse ear acquired in the forward- (a) and epi- (b) direction at 2849 cm^{-1}. The signal in image (a) is approximately 6 times brighter than (b). The images are an average of 10 frames acquired in a total of 7.5 seconds. Scale bars are 20 μm.

given by the CARS excitation line width of less than 0.5 cm^{-1} and the matching minimal tuning step of 0.4 cm^{-1}. Typical Raman line widths in the high-wavenumber region are on the order of several tens of cm^{-1}. Hence, the tuning step in the experiments can be adjusted without any loss of information.

In Fig. 3.6(a), WS-CARS spectra of different chemical species (peanut oil, dimethyl sulfoxide (DMSO), silicone and polystyrene) are presented. The spectral asymmetry in nonlinear efficiency from this laser system (see Fig. 3.4(b)) modulates the intensities of the Raman lines but not their spectral positions. Peanut oil is composed mainly of unsaturated fatty acid (56.6% oleic acid and 26.7% linoleic acid). Its Raman band, attributed to the symmetric CH_2 stretching mode, shows a strong peak at 2849 cm^{-1}. Pure DMSO has an intense Raman band at 2914 cm^{-1} attributed to the symmetric CH_3 stretching vibrations of its methyl groups. Silicone and polystyrene have slightly more complex spectra which are also weaker. The liquid samples are placed in a 140 μm deep chamber on a microscope slide and covered by a cover slip. A mixture of 10 μm polystyrene beads (Polysciences) and water is used in a similar manner. Proper alignment of the excitation beams on a polystyrene bead is done using a CARS image such as the one presented in Fig. 3.6(b). All the spectra are acquired in 622 ms at a rate of 2 ms/step. They cover the range from 2697.6 to 2954.1 cm^{-1} with an acquisition resolution of 0.8 cm^{-1} (321 points). Fig. 3.6(b) shows two images of 10 μm diameter polystyrene beads in peanut oil recorded at two different Raman lines. The image acquired at 2849.0 cm^{-1} (top) emphasizes the contribution from the surrounding oil while the image acquired at 2889.8 cm^{-1} (bottom) highlights the equal contributions of the polystyrene and the oil at that wavenumber. The images are an average intensity projection of 10 frames acquired in a total of 7.5 seconds.

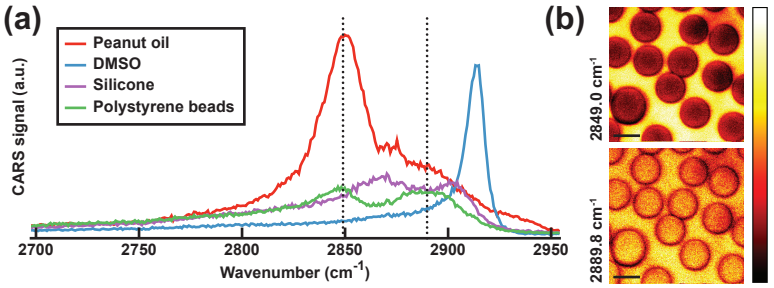

Figure 3.6 – (a) WS-CARS spectra of peanut oil (red), DMSO (blue), silicone (purple) and polystyrene beads (green). Each spectrum ranges from 2697.6 to 2954.1 cm^{-1} with a resolution of 0.8 cm^{-1}. The PL tuning rate is 2 ms/step and the total acquisition time is 622 ms per spectrum. (b) CARS images of polystyrene beads in peanut oil recorded at 2849.0 cm^{-1} (top) and 2889.8 cm^{-1} (bottom) in the forward direction. Scale bars are 10 μm.

Next, the sensitivity and speed of the single point spectroscopy mode is demonstrated. Fig. 3.7 shows WS-CARS spectra of various fatty acids of different degrees of saturation. Fatty acids are characterized by a carboxylic acid (R–COOH) attached to an aliphatic chain

(...–CH_2–CH_2–CH_2–...) which can be saturated or unsaturated to various degrees. The degree of unsaturation can be determined based on their nonlinear Raman signature [Chowdary et al., 2010]. As seen in Fig. 3.7 the number of double bonds in the chain alters the relative shape of the spectra. The spectra are in good agreement with previously published spontaneous Raman spectra [Freudiger et al., 2008]. Olive oil, composed mostly of oleic acid and palmitic acid, is 13% saturated, 73% monounsaturated and 11% polyunsaturated. The other fatty acids are docosahexaenoic acid (DHA), eicosapentaenoic acid (EPA) and arachidonic acid (AA) which have respectively six, five and four C=C bonds in their aliphatic chains. The samples are placed in a 140 μm deep chamber on a microscope slide and protected by a cover slip. Each spectrum ranging from 2697.6 to 2989.7 cm^{-1} with an acquisition resolution of 0.4 cm^{-1} (711 points), is acquired in 71 ms at a rate of 100 μs/step. The data is filtered using a running average algorithm with a window of 11 pixels for an effective resolution of 4 cm^{-1}.

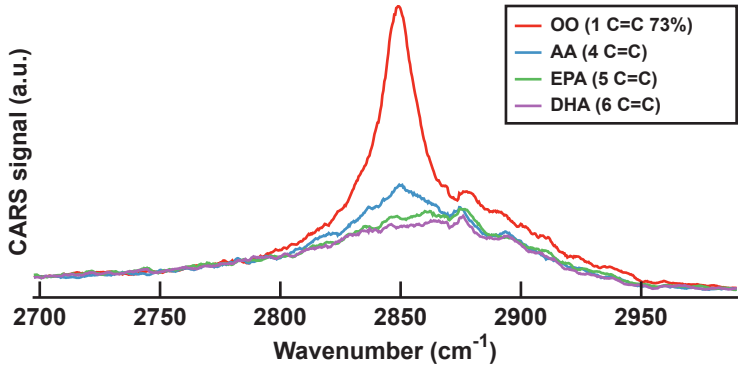

Figure 3.7 – WS-CARS spectra of unsaturated fatty acids. Olive oil (OO) is 13% saturated and 73% monounsaturated, arachidonic acid (AA) has 4 double bonds, eicosapentaenoic acid (EPA) has 5 double bonds and docosahexaenoic acid (DHA) has 6 double bonds. Each spectrum was acquired in 71 ms at a rate of 100 μs/step.

3.5.3 WS-CARS hyperspectral imaging

In this section, hyperspectral imaging of a skin sample incubated in DMSO (Fig. 3.8) is presented. DMSO is a lipophobic compound that easily penetrates the skin. For this experiment, a complete mouse ear is kept in DMSO for 2 hours at room temperature and placed on a microscope slide for imaging. The HSI is acquired using ScanImage externally triggered by the synchronized lasers system during a wavelength sweep ranging from 2786.8 cm^{-1} to 2950.1 cm^{-1} with a resolution of 2 cm^{-1} at a rate of 1 Hz. The acquisition time for the 256x256x81 HSI is 81 seconds (1.2 ms per spectrum) with a corresponding true pixel dwell time of 6.4 μs per wavelength. This pixel dwell time is comparable to what is achieved using commercial systems, and emphasizes that the system is almost as efficient as fluorescence microscopes while providing full spectral information. A closer look at the HSI shows

that the fat is compartmentalized in the adipocytes (Fig. 3.8 left image, 2849 cm^{-1}) while the DMSO is constrained to the extracellular space (Fig. 3.8 right image, 2914 cm^{-1}). The lipophobic nature of DMSO is also evident in the spectral projection (Fig. 3.8 central panel) where we can see that the two compounds are mutually exclusive.

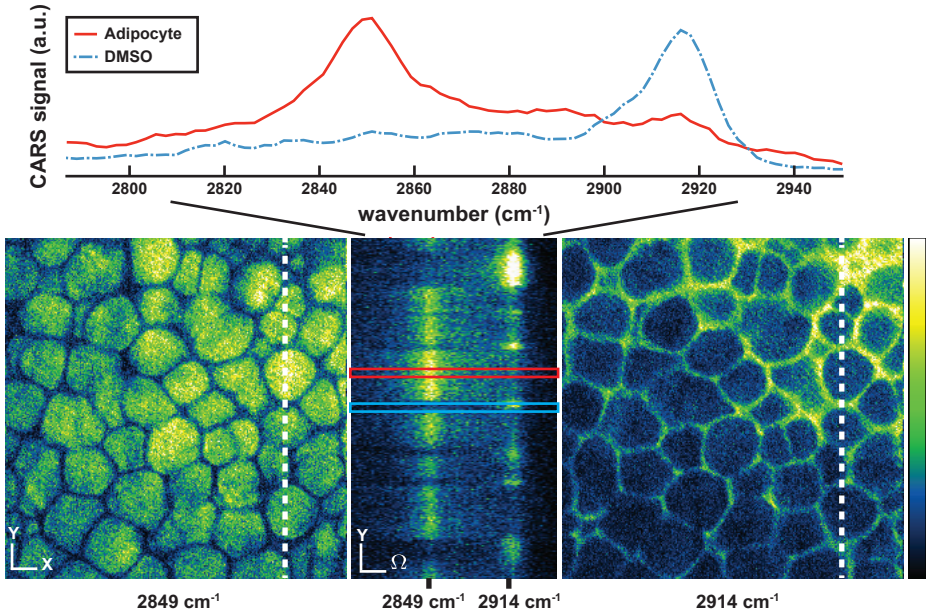

Figure 3.8 – Hyperspectral CARS images of mouse skin incubated in DMSO for 2 hours. The left and right images correspond to the lipid (2849 cm^{-1}) and DMSO (2914 cm^{-1}) Raman line. The central panel shows a spectral projection along the dotted lines. The adipocytes and DMSO CARS spectra (4-pixel-wide red and blue boxes in central panel) are shown on top. A total of 81 images were acquired at a rate of one frame per second. Every pixel in the HSI is a spectrum ranging from 2786.8 cm^{-1} to 2950.1 cm^{-1}. Acquisition time for the 256x256x81 HSI is 81 seconds (1.2 ms per spectrum). The images were acquired in the forward direction. Scale bar is 10 μm.

Discrimination between chemical species can be done much more rapidly by imaging only the relevant Raman bands since the integration time scales linearly with their numbers. For example, a look at the spectra from Fig. 3.8 shows that DMSO has a vibrational resonance (2914 cm^{-1}) which is well separated from the lipid peak (2849 cm^{-1}). Therefore, they can be easily differentiated using random access multi line imaging resulting in much shorter acquisition times. Furthermore, since this system can access any arbitrary sequence of Raman lines in its tuning range, multi line imaging can easily be scaled to suit more demanding experiments. This will be especially useful for applications such as *in vivo* tissue diagnosis where many vibrational lines would be needed to identify complex tissue constituents with great speed. In this example, after proper identification of the diagnostically relevant Raman lines, imaging could be performed over a large area in a short time.

3.6 Conclusion

We presented a wavelength-swept approach to CARS microscopy that is especially well suited for experiments on thick tissue where scattering plays an important role. This system does not require a spectrometer that would limit collection efficiency and prevent epi-detection. The current system configuration is designed to access Raman lines within most of the high-wavenumber region (2700-2950 cm^{-1}). Tuning speeds of up to 100 μs per spectral points are demonstrated with the acquisition of CARS spectra of various samples. As well, CARS hyperspectral images containing tens of thousands of spectra are acquired in just over a minute. Thanks to the 12 MHz repetition rate, efficient CARS generation is possible even with 35 ps pulses. Strategies to shorten the pulses, using for instance a shorter pulse generator or a time-lens [Wang et al., 2010], are being explored. This flexible all-fibre system could bridge an important gap between fundamental research microscopy tools and clinically useful instruments by combining the context of imaging with the richness of spectroscopic information.

Chapter 4

Local assessment of myelin health in a multiple sclerosis mouse model using a 2D Fourier transform approach

S. Bégin,[1,2,3] E. Bélanger,[1,2,3] S. Laffray,[1,3] B. Aubé,[1,3,4] É. Chamma,[1,3] J. Bélisle,[1] S. Lacroix,[4,5] Y. De Koninck,[1,6] and D. Côté[1,2,3]

[1] Centre de recherche de l'Institut universitaire en santé mentale de Québec (CRIUSMQ), Université Laval, Québec, Canada
[2] Département de physique, génie physique et optique, Université Laval, Québec, Canada
[3] Centre d'optique, photonique et laser (COPL), Université Laval, Québec, Canada
[4] Centre de recherche du CHU de Québec-CHUL, Université Laval, Québec, Canada
[5] Département de médecine moléculaire, Université Laval, Québec, Canada
[6] Département de psychiatrie et de neurosciences, Université Laval, Québec, Canada

4.1 Résumé

Nous présentons une approche automatisé basée sur la transformée de Fourier à deux dimensions (2D-FT) pour analyser localement l'organisation des axones myélinisés dans la moelle épinière. La microscopie par diffusion Raman cohérente (CARS) a été utilisé pour observer des lésions dans un modèle animal de la sclérose en plaques couramment utilisé: l'encéphalomyélite allergique expérimentale (EAE). Les images sont fractionnées et une 2D-FT permet de trouver l'orientation moyenne ainsi que l'anisotropie directionnelle des fibres dans les sous-domaines contigus. Nous introduisons le paramètre de corrélation corrigée, une mesure de la corrélation entre les orientations de domaines adjacents. Nous montrons que dans le modèle animal EAE de sclérose en plaques, le PCC peut être utilisé pour quan-

tifier le degré d'organisation/désorganisation de la structure de la myéline. Cette analyse a été appliquée à un grand nombre d'images provenant d'animaux de différents scores cliniques. Nous démontrons que certains descripteurs de la fonction de densité de probabilité du paramètre de corrélation corrigée sont fortement corrélés avec les scores cliniques des animaux. Cette procédure, compatible avec l'imagerie d'animaux *in vivo*, a été développé pour l'évaluation locale *in situ* des axones myélinisés affectés par l'EAE.

4.2 abstract

We present an automated two-dimensional Fourier transform (2D-FT) approach to analyze the local organization of myelinated axons in the spinal cord. Coherent anti-Stokes Raman scattering (CARS) microscopy was used to observe lesions in a commonly used animal model of multiple sclerosis (MS), experimental autoimmune encephalomyelitis (EAE). A 2D-FT was applied on the CARS images to find the average orientation and directional anisotropy of the fibers within contiguous image domains. We introduce the corrected correlation parameter (CCP), a measure of the correlation between orientations of adjacent domains. We show that in the EAE animal model of MS, the CCP can be used to quantify the degree of organization/disorganization in the myelin structure. This analysis was applied to a large image dataset from animals at different clinical scores and we show that some descriptors of the CCP probability density function are strongly correlated with the clinical scores. This procedure, compatible with live animal imaging, has been developed to perform local *in situ* evaluation of myelinated axons afflicted by EAE.

4.3 Introduction

Proper function of the nervous system relies on fast electrical conduction between neurons, sometimes over very long distances. For instance, muscle movements are triggered by action potentials that propagate from cortical neurons to the spinal cord and finally to the neuromuscular junction. The myelin sheath surrounding the axons in the white matter of the central nervous system (CNS) is essential for efficient and fast transmission of electric signals between the source and target cells. The degeneration of myelin along axons caused by certain CNS pathologies such as multiple sclerosis (MS), leads to poor signal conduction. Demyelination also causes axons to become vulnerable to irreversible damage caused by immune cells, which often results in paralysis [Nave, 2010]. The driving mechanisms for the loss of myelin are thought to be largely autoimmune in nature [King et al., 2009]. However, much remains unanswered with respect to the exact sequence of events leading to lesion formation in MS and the key players that are involved [van der Valk and Amor, 2009, Filippi et al., 2012]. The experimental autoimmune encephalomyelitis (EAE) animal model is a good surrogate for the human condition [Mix et al., 2010, 't Hart et al., 2011]. The clinical progres-

sion of the disease is assessed by evaluating the motor skills of the animal. The clinical score, given on a scale of 0 to 5, represents a global average of all lesions across the brain and spinal cord into a single number representing their final effects on motor skills, and as such, does not provide information on the severity of individual lesions. This is in stark contrast with the cellular view of EAE where one observes a very high amount of heterogeneity in spinal cord lesions both throughout the cord and across different animals [Brown and Sawchenko, 2007]. With this in mind, there is a clear need for a local, objective, and fast assessment of myelin morphology or architecture to identify and follow potential early lesions at the cellular level.

Myelin was visualized with coherent anti-Stokes Raman scattering (CARS) microscopy, a label-free technique that takes advantage of the endogenous contrast provided by the lipid content of myelin [Evans and Xie, 2008, Bégin et al., 2009, Pezacki et al., 2011]. CARS imaging of spinal tissue has been first reported in 2005 by Wang *et al*. [Wang et al., 2005]. Since then, it has been used to visualize demyelination [Fu et al., 2007b, Imitola et al., 2011, Fu et al., 2011, Shi et al., 2011, Freudiger et al., 2012], and we have proposed several techniques to characterize myelin morphology in this context [Bélanger et al., 2009a, 2011]. We now extend this work using CARS images of myelin acquired in mice affected with EAE to quantify the local tissue architecture within an image, but not the structure of individual myelin sheaths.

Recently, researchers have characterized the local tissue architecture of collagen imaged with second harmonic microscopy by using a two-dimensional Fourier transform (2D-FT) method [Matteini et al., 2009, Rao et al., 2009, Cicchi et al., 2013]. More specifically, the average fiber orientation as well as the directional anisotropy within the image were extracted from the 2D-FT and then used to calculate the correlation between the orientations of neighboring domains [Ghazaryan et al., 2013]. The main goal of the present article is therefore to expand this formalism and to introduce a metric adapted to myelin images obtained with CARS microscopy. This metric becomes a local assessment of myelin health. First, we demonstrate how the degree of directional anisotropy is incorporated as a modification to the correlation parameter introduced previously. Then, we show how it is calculated on images of the spinal cord taken from EAE mice at different clinical stages of the disease. Finally, we conclude by discussing how this new metric is highly sensitive to regions where the myelin structure is strongly disrupted and can be used to separate lesions from healthy tissue.

The MATLAB code implementing this analysis as well as the data will be made available on the group web site at http://www.dcclab.ca.

4.4 Materials and methods

4.4.1 EAE Induction

EAE was induced in eight 10 weeks old C57BL/6 female mice using the Hooke Laboratories kit EK-0115. The kit is composed of an emulsion of complete Freund's adjuvant (CFA) and MOG35-55 (1 mg/mL), a myelin oligodendrocyte peptide. The CFA is composed of incomplete Freund's adjuvant with killed mycobacterium tuberculosis H37Ra (2 mg/mL). On the day of immunization, mice received 0.1 mL of the emulsion injected subcutaneously (s.c.) on the upper back and 0.1 mL on the lower back. They were also administered 0.1 mL of pertussis toxin (PTX, 0.7-10 μg/mL of phosphate buffer solution (PBS)) intraperitoneally (i.p.) and again 24 hours later. A total of four control animals were divided into two groups. First, two CFA control mice received the same injections on day 0 and 1, but an antigen-free emulsion was used. The CFA control mice are used to assess the effects of both PTX and CFA on myelin. Secondly, two saline control mice received saline only both s.c. and i.p. on day 0 and 1. Clinical signs were scored daily and graded from 0 to 5: 0 = no signs, 1 = limp tail, 2 = limp tail and weakness in hind legs, 3 = limp tail and paralysis of hind legs, 4 = limp tail, paralysis of hind legs and weakness of front legs, 5 = complete paralysis of both hind and front legs. All procedures were approved by our local institutional animal care and use committee.

4.4.2 Tissue preparation

Mice were selected for tissue processing based on their clinical score to have tissue samples from all of the early stages of the disease (0-3). Mice were intracardially perfused with 0.1 M PBS followed by 4% paraformaldehyde (PFA). The whole spinal cord was dissected out from each mouse and placed in 4% PFA overnight. Cervical, thoracic and lumbar spinal segments corresponding respectively to the C3-5, T4-8 and L3-5 levels were isolated from the spinal cord. Each spinal segment was mounted in a petri dish filled with agarose gel. A cavity corresponding approximately to the size of each spinal segment was carved into the gel and used to support the segment during imaging. The remaining space was filled with 0.1 M PBS and a coverslip was mounted on top of the agarose chamber.

4.4.3 CARS microscopy

The laser sources and the custom-made video-rate laser scanning microscope have been described previously [Veilleux et al., 2008]. In short, the laser system consists of an optical parametric oscillator (OPO) (Levante Emerald OPO ps, APE-Berlin) pumped by a frequency-doubled Nd:Vanadate mode-locked laser (picoTRAIN, High Q Laser). CARS is a nonlinear process requiring two pulsed laser beams whose frequency difference matches a Raman active vibration in the sample [Duncan et al., 1982, Zumbusch et al., 1999a]. To probe the CH_2 symmetric stretch vibrations of lipids at 2845 cm^{-1}, the 1064 nm laser was used as the Stokes

beam with the signal from the OPO tuned to 816.8 nm as the pump beam. The excitation beams were overlapped in space using a dichroic long-pass filter (LP02-1064RU-25, Semrock) and in time using a delay line before being sent to the video-rate laser scanning microscope. The states of polarization of the excitation beams was carefully controlled to be circular to avoid the polarization dependence of the CARS signal intensity [Bélanger et al., 2009a]. To avoid photodamage of the spinal cord tissue, the average power of the pump and Stokes beam at the sample was limited to a few tens of mW.

The microscope achieves an image acquisition rate of 15 frames per second by using a gold-coated polygonal mirror for the fast axis (DT-36-290-025, Lincoln Laser) and a galvanometer mirror for the slow axis (6240H, Cambridge Technology). The field of view (FOV) of the microscope is 112.5 μm by 112.5 μm with a 60$\times$ objective lens (UPLSAPO 1.2 NA w, Olympus) and the images are 500$\times$500 pixels in size (225 nm/pixel). The backscattered anti-Stokes signal at 662.8 nm was epi-detected using a dichroic long-pass filter (FF735-Di01- 25$\times$36, Semrock) for the signal extraction, the combination of two laser block filters (FF01-750/SP-25, Semrock) and a band-pass filter (FF01-655/40-25, Semrock) to filter out unwanted residual light and a red-sensitive photomultiplier tube (R3896, Hamamatsu) for the detection.

4.4.4 CARS map acquisitions of the spinal cord surface

All spinal segments (cervical, thoracic and lumbar) were imaged on the dorsal side. Additionally, for the lumbar segments, the lateral and ventral sides were imaged as well. To image the complete surface of a segment, the sample was moved using a manipulator (MPC-200 with ROE-200, Sutter Instrument) across a volume corresponding to a thin rectangular slab containing the surface planes of the spinal cord. This gave an x-y grid sequence of z-stacks with an overlap of 20 % of the image FOV. Complete maps were typically acquired in 4 hours.

4.4.5 Post-acquisition image processing

Prior to the analysis, some image processing was required to generate 2D maps of the spinal cord surface. First, all the raw images were flat-field corrected and then the z-stacks were assembled together using Fiji [Preibisch et al., 2009] to form 3D maps. The last step consists in reducing the volumes to 2D maps by choosing the surface plane of interest, to facilitate their visual exploration, reduce the file sizes and decrease computation time for the analysis. The challenge in this step lies in defining this plane of interest in terms of quantitative parameters that can be automatically measured. For our particular case, we found that the average intensity and the standard deviation of the pixel values in a 100$\times$100 window surrounding a pixel of interest in an image plane of a 3D map are good indicators to determine if that particular pixel is located in the plane of interest. For every pixel in a given x-y plane, the average intensity and standard deviation values were compared with those calculated from the pixels located in the same x-y position but at different z positions of the 3D maps. By maxi-

mizing those values, one can determine which z pixel is best suited for the 2D reconstruction of the spinal cord surface.

4.4.6 Analysis of fiber orientation

The general orientation of the fibers was obtained by finding the orientation of the Fourier spectrum of the image. In the first step of the analysis, a CARS map of the surface of the spinal cord segment was subdivided into square domains of equal sizes. The domains were transformed using a 2D-FT. The resulting images were treated using a 2D adaptive Wiener noise filtering method [Lim, 1990] and a 2D Savitzky-Golay smoothing filter [Savitzky and Golay, 1964] before undergoing segmentation. Each image was then segmented using a thresholding method described below and the resulting segmented object was transformed into an ellipse that has the same second-order moments.

The average fiber orientation within the image domain can be inferred from the direction of the minor axis of the ellipse. This orientation is expressed within the range $\pm 90^\circ$ with respect to the image horizontal axis. In addition, the directional anisotropy within the image domain is given by the aspect ratio (AR) between the minor and the major axes of the ellipse. The AR is interpreted as the accuracy of the calculated average fiber orientation, with values ranging from 0 (accurate) to 1 (inaccurate).

To determine the optimal domain size, we calculated the median AR from all the maps from control animals (saline and CFA) for domains of different sizes (Fig. 4.1). The domain size should be small enough to maximize spatial resolution but large enough to provide an accurate orientation of the fibers. At very small domain sizes, the average AR always approaches 1 regardless of the actual image due to poor frequency sampling. On the other hand, domains larger than typical lesion size sacrifice the spatial resolution with no benefit to the accuracy of the orientation. This is a direct consequence of the overall parallel alignment of the nerve fibers in the spinal cord and we thus choose to determine the optimal domain size of 192 pixels as shown in Fig. 4.1. Note that this is different for collagen in biological tissue in which there is no unique orientation over large areas [Ghazaryan et al., 2013].

To find the appropriate threshold level for the image segmentation, we assumed that: 1) the shape of the segmented object has to be as close as possible to an ellipse, and 2) the AR of the ellipse has to be as small as possible for an accurate estimation of the average fiber orientation. Every 2D-FT image was therefore segmented at various levels across its intensity range and for every threshold value, the ellipticity of the object and the AR of the equivalent ellipse were computed. The ellipticity is defined as [Rosin, 2003]:

$$E_I = \begin{cases} 16\pi^2 I_1 & if\ I_1 \leq \frac{1}{16\pi^2} \\ \frac{1}{16\pi^2 I_1} & otherwise, \end{cases} \tag{4.1}$$

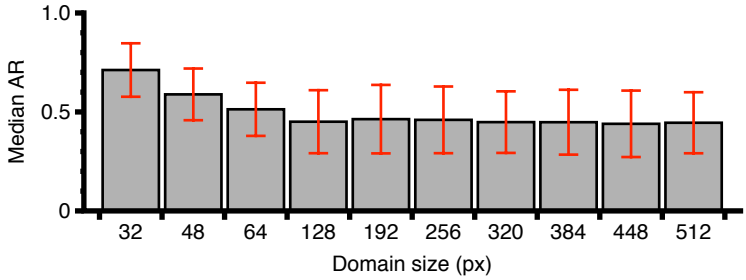

Figure 4.1 – Median AR (with median absolute deviation) as a function of domain size. For small domain sizes, poor orientation accuracy is due to lack of data on fiber morphology. At large sizes, no additional accuracy is obtained on the orientation although spatial resolution is decreased. The optimal size was thus choosen to be 192 pixels.

where I_1 is the simplest affine moment invariant of the circle [Flusser and Suk, 1993] and can be written as:

$$I_1 = \frac{\mu_{20}\mu_{02} - \mu_{11}^2}{\mu_{00}^4}. \tag{4.2}$$

I_1 is defined in terms of the central moments:

$$\mu_{pq} = \sum_{x,y}(x - \bar{x})^p (y - \bar{y})^q \mathrm{I}(x, y), \tag{4.3}$$

where $\bar{x}$ and $\bar{y}$ are the components of the image centroid and $\mathrm{I}(x, y)$ is the pixel intensity. Finally, the threshold value corresponding to the maximum ratio of the ellipticity and AR was used for the segmentation.

To demonstrate this strategy, we applied the analysis on 192×192 pixels domains for three different CARS images of mouse spinal cord surface (Fig. 4.2). From top to bottom in Fig. 4.2(a), the tissue becomes progressively afflicted by EAE lesions and the tissue organization suffers accordingly. Fig. 4.2(b) shows the noise filtered and smoothed 2D-FT of the domains. In Fig. 4.2(c), superposed on the resulting segmented objects are the equivalent ellipses with lines highlighting the orientation of the minor and major axes. Finally, in Fig. 4.2(d), the average tissue orientation is drawn over the images with the color of the line representing the AR (see AR color code at the right of Fig. 4.2).

4.4.7 Correlation parameter

The correlation parameter (CP) is a quantitative parameter evaluating the collinearity between the orientations of neighboring domains [Ghazaryan et al., 2013]. For two adjacent domains, the scalar product between the orientations of the (i, j) and $(i + 1, j)$ domains can be expressed as $\vec{S}_{i,j} \cdot \vec{S}_{i+1,j}$. For domain angles $\theta_{i,j}$ and $\theta_{i+1,j}$, this expression becomes:

$$\vec{S}_{i,j} \cdot \vec{S}_{i+1,j} = \mid \vec{S}_{i,j} \mid\mid \vec{S}_{i+1,j} \mid cos(\theta_{i,j} - \theta_{i+1,j}) \tag{4.4}$$

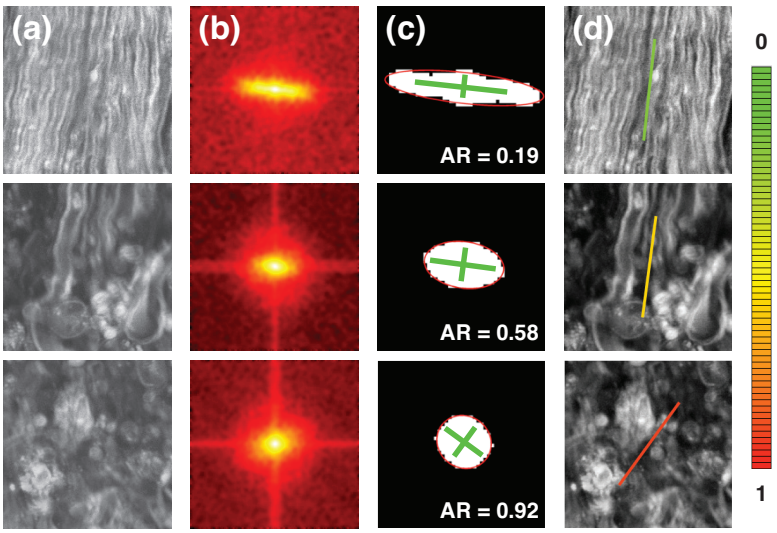

Figure 4.2 – (a) Three different CARS images of mouse spinal cord surface in the longitudinal orientation. From top to bottom, the tissue becomes progressively afflicted by EAE lesions. (b) Processed 2D-FT of the domains. (c) Segmented objects with superposed equivalent ellipses and main axes. (d) Average fiber orientation overlaid on the images with AR color-coded (AR color code shown right).

or, for unit vectors $\vec{S}$:

$$\vec{S}_{i,j} \cdot \vec{S}_{i+1,j} = cos(\theta_{i,j} - \theta_{i+1,j}). \tag{4.5}$$

For simplicity, this expression can be transformed so that it varies from -1 for orthogonal domain orientations to +1 for perfectly parallel domain orientations of fibers for any two angles in the range $\pm 90°$. We call this value the collinearity between the domains i and $i+1$:

$$\mathrm{C}_{i \to i+1} = 2[cos^2(\theta_{i,j} - \theta_{i+1,j}) - 0.5]. \tag{4.6}$$

Finally, the CP representing the collinearity of domain (i, j) with all four neighboring domains can be expressed as the average collinearity for all four neighbors:

$$CP_{i,j} = \frac{\mathrm{C}_{i \to i-1} + \mathrm{C}_{i \to i+1} + \mathrm{C}_{j \to j-1} + \mathrm{C}_{j \to j+1}}{4}, \tag{4.7}$$

or, more generally as:

$$CP_{i,j} = \frac{1}{\mathrm{N}_{nb}} \sum_{\mathrm{N}_{nb}} 2 \left[cos^2(\theta_{i,j} - \theta_{nb}) - 0.5 \right], \tag{4.8}$$

where nb represents the four possible neighbors and the number of neighbors (N_{nb}) is introduced to ensure that CP stays in the range ± 1. A CP value close to 0 implies a random orientation of domains with no correlation.

Moreover, the uncertainty in the fiber orientation was taken into account with a correction to the CP using the following expression:

$$\mathrm{CCP} = \mathrm{CP}[1 - \mathrm{AR}], \tag{4.9}$$

where CCP is the corrected correlation parameter. When the fiber orientation is certain (low AR), this correction affects the CP only slightly. On the other hand, the usefulness of the correction is made apparent when the fiber orientation is uncertain (high AR) but correlated between neighbored domains (high CP). In this case, the CCP is lowered which gives a better indication of a lesion.

An example is presented in Fig. 4.3 where the CP and CCP were calculated on the central 192×192 pixels domain for two CARS images of mouse spinal cord in the longitudinal orientation. For all three panels, the top image shows healthy tissue and the bottom image shows tissue where the myelin structure is lost due to an advanced stage of EAE. In Fig. 4.3(a), the orientation and AR were calculated for the central domain as well as for its four neighboring domains. In Fig. 4.3(b) and (c) the CP and the CCP have been calculated for both images. For the image of healthy tissue (top example), the CCP is close to 1, implying good tissue organization. On the bottom image, the CCP is closer to 0 because the fiber orientation is uncertain and more random between the domains, which is indicative of a loss of organization in the tissue. The result is shown as a color overlay following the color code shown at the bottom of Fig. 4.3.

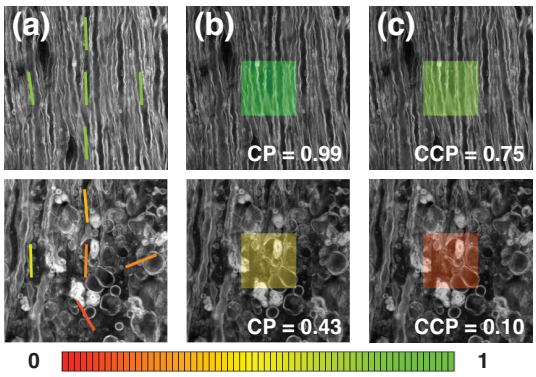

Figure 4.3 – Two CARS images of healthy (top) and diseased (bottom) spinal cord. (a) The orientation and AR were calculated for square domains of 192×192 pixels. In (b) and (c), the calculated CP and CCP are shown on the bottom right corner as well as color-coded on the images (CP and CCP color code shown at the bottom).

4.5 Results and discussion

To validate the ability of the corrected correlation parameter (CCP) in discriminating different stages of myelin degeneration, images from four controls (i.e. injected with saline or CFA) and eight immunized mice were chosen and compared together. Those twelve images were representative of the various levels of surface tissue organization (healthy-appearing, moderate and severe disorganization) encountered in control and EAE animals. The 216×216 μm

images were subdivided in 25 domains of 192×192 pixels and then characterized by their median CCP. Fig. 4.4 shows the images with a color-coded CCP on each tile in decreasing order of their median CCP. In Fig. 4.4(a), all six images show healthy-appearing white matter and their CCPs are accordingly high (CCP $>$ 0.5). Fig. 4.4(b) shows three images typical of moderately disorganized tissue and Fig. 4.4(c) is showing three images with a more severe disorganization. As can be seen from panels b and c, the values of the median CCP confirm the visual assessment of the level of degeneration and indicate that the CCP can discriminate various lesion states as observed in the spinal cord of EAE animals. Thus, the CPP that we established represents an objective, local measurement of myelin health and is indicative of local disorganization and disruption.

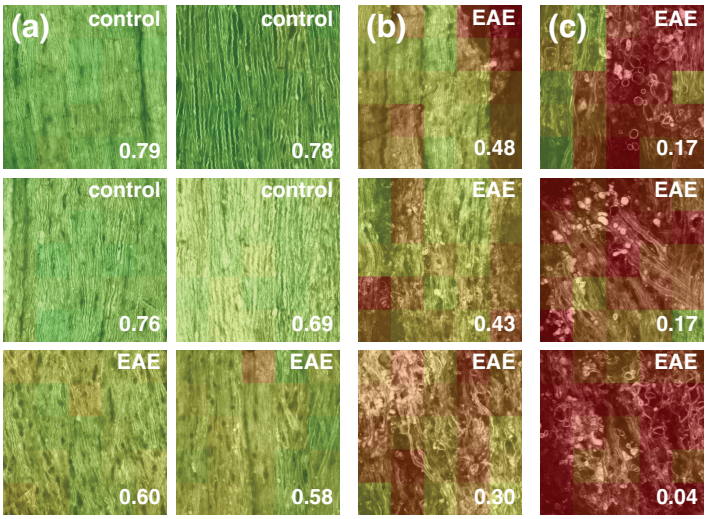

Figure 4.4 – The CCP was calculated for twelve images, each divided into 25 domains. The median CCP is shown. (a) Six images typical of healthy-appearing spinal cord tissue. (b) Three images showing a moderate degree of disorganization. (c) Three images showing a severe degree of disorganization.

Note that over large areas of the spinal cord, the heterogeneous nature of EAE becomes apparent. For instance, in Fig. 4.5, a larger map of the spinal cord surface (600×600 μm) from a score 1 mouse shows that lesions appear locally throughout the spinal cord and that the level of tissue organization is highly heterogeneous. On the scale of this image, the median CCP is not sufficient to describe the tissue: the median CCP is 0.57, with the upper left area showing healthy-appearing white matter and a median CCP of 0.71, while the lower right corner shows a lesion where the tissue is severely disorganized and the median CCP is only 0.10. Hence, the CCP is only meaningful in small regions of interest whose dimensions are on the order of the expected lesion size. As we show in the next paragraph, the probability density function (PDF) of the CCP is a good descriptor for larger areas.

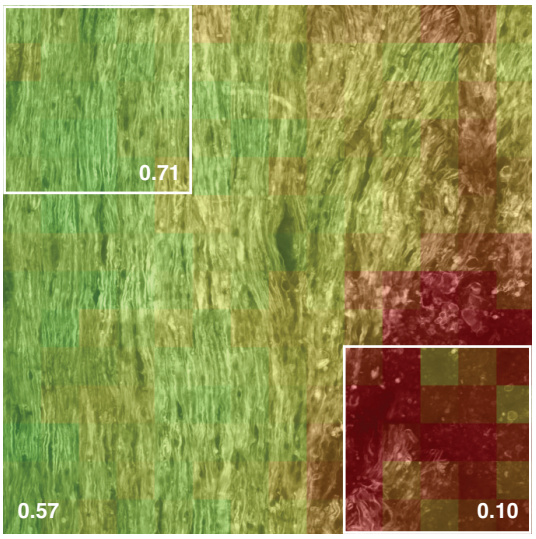

Figure 4.5 – In this large map of spinal cord surface (600×600 μm), we can see that the lesions appear in patches. The difference between the median CCP of the whole image and that of the two subsections highlights the fact that the level of tissue disorganization is heterogeneous throughout the spinal cord.

Whereas the EAE clinical score is a global functional measure of the motor skills of the animals, we have clearly demonstrated that the CCP is a local structural measure of the level of tissue organization within a myelinated area. This complex and novel analysis was applied to our complete image dataset covering about 30 mm^2 of spinal cord surface from animals at different clinical scores, for a total of 16,000 square domains. The results are presented as the PDF of the CCP in Fig. 4.6. The two mice per condition are labeled M1 (blue line) and M2 (orange line) and the number of domains per mouse is indicated (ND_{M1}, ND_{M2}). As expected, samples from mice displaying high EAE clinical scores have accumulated a greater number of low CCP regions (lesions) and the severity of those lesions is higher (lower CCP values).

Although a certain amount of variability is apparent between mice of the same score, there is clearly a trend linking the shape of the PDF to the clinical scores. To substantiate this, we have calculated the Spearman correlation coefficients (r_s) of six different descriptors of the PDF with the clinical scores. In Fig. 4.7, the descriptors are plotted against the different conditions in order of decreasing correlation coefficient: mean CCP ($r_s = -0.9329$), healthy fraction ($r_s = -0.9188$), median CCP ($r_s = -0.8622$), middle 95% CCP range ($r_s = 0.8340$) and PDF kurtosis and skewness ($r_s = -0.3534$ and $r_s = 0.0707$ respectively). The mean CCP and the healthy fraction show a strong correlation whereas the PDF kurtosis and skewness are not correlated with the clinical score. The healthy fraction is the ratio of the number of healthy domains to the total number of domains. Since 97% of the domains of the saline and

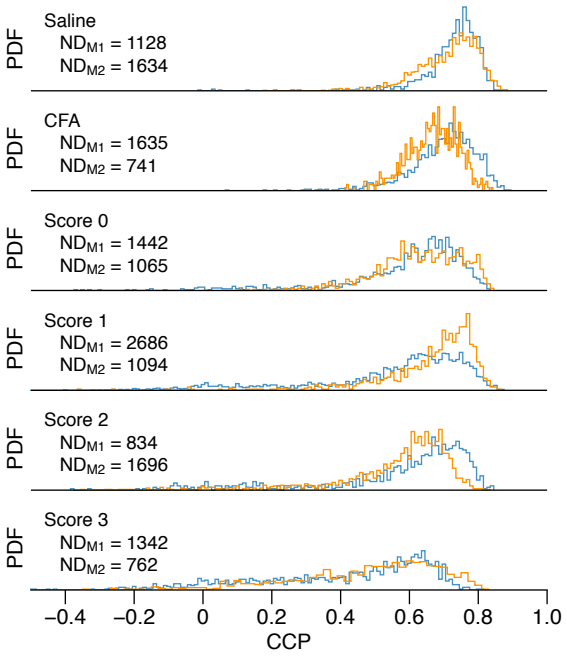

Figure 4.6 – PDF of the CCP for all domains in maps for both control and EAE mice (two mice per condition, blue and orange lines). The number of domains per mouse (ND_{M1}, ND_{M2}) is indicated for all conditions.

CFA maps have a CCP value above 0.5, this was determined to be the threshold separating the two categories, healthy-appearing and disorganized tissue. For each parameter, we used the standard bootstrap method [Efron and Tibshirani, 1993] to make sure that the spinal cord sampling was sufficient. The bootstrap percentile confidence interval at 95% was calculated using 10,000 bootstrap replications of the PDFs. The best line from a robust linear regression is also plotted to give a sense of the degree of correlation.

The myelin disruption, although related to nerve function, is not a direct measurement of a nerve functional integrity. In fact, a more complete model relating myelin disruption to loss of nerve function would clearly consider the number, size and most importantly localization of the moderate to severe lesions throughout the entire spinal cord. The robust and automated technique developed here is a first step in that direction. In addition, because the CCP can be calculated in real time, this procedure is compatible with live animal imaging to provide *in situ* information to complement the structural measurements of the local myelin architecture. For example, it would be possible to screen large areas of the spinal cord, find areas of interest indicative of possible early lesions, and measure a more extensive set of functional parameters (blood-brain-barrier permeability, cellular recruitment, microglial activity, etc...). When coupled with a minimally invasive microendoscopic approach [Bélanger et al., 2012], it would be possible to follow the evolution of a given region of interest over

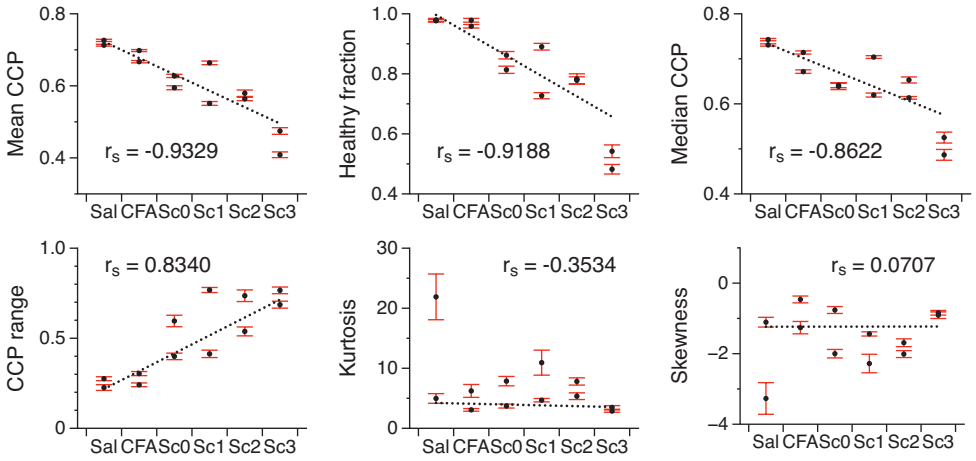

Figure 4.7 – Different descriptors of the PDF are plotted against the clinical scores in order of decreasing correlation coefficient (r_s). The bootstrap percentile confidence interval at 95% shows the sampling error. The line of best fit is plotted to emphasize the correlation.

time to understand the sequence of the interactions between all the key players.

4.6 Conclusion

In this article, we presented an approach to calculate the average orientation and the directional anisotropy within a myelin image domain. We also introduced a new quantitative parameter, the corrected correlation parameter (CCP), used to assess myelin health locally on images taken from the spinal cord of mice at different stages of a MS-like pathology. We have shown that the CCP can be used to quantify the degree of organization/disorganization in the myelin structure. We have also shown that in the EAE animal model of MS, the number of sites with a lower CCP increases as the disease progresses. The CCP could therefore be developed into a parameter for presymptomatic detection of myelin disruption. This metric will be combined with other measurements such as blood-brain-barrier permeability and cellular recruitment measurements to obtain a more complete picture of the disease at various stages of its development.

Chapter 5

Automated method for the segmentation and morphometry of nerve fibres in large scale CARS images of spinal cord tissue

Steve Bégin[1,2,3], Olivier Dupont-Therrien[1,3], Erik Bélanger[1,2,3], Amy Daradich[1,2,3], Sophie Laffray[1,3], Yves De Koninck[1,4] and Daniel Côté[1,2,3,*]

[1] Centre de recherche de l'Institut universitaire en santé mentale de Québec (CRIUSMQ), Université Laval, Québec, Canada
[2] Département de physique, génie physique et optique, Université Laval, Québec, Canada
[3] Centre d'optique, photonique et laser (COPL), Université Laval, Québec, Canada
[4] Département de psychiatrie et de neurosciences, Université Laval, Québec, Canada

5.1 Résumé

Nous présentons une méthode entièrement automatisé permettant la segmentation à grande échelle de fibres nerveuses dans des images de microscopie par diffusion Raman cohérente (CARS). La méthode a été spécifiquement conçu pour traité des images CARS de coupes transversales de tissu nerveux, mais convient également aux images de microscopie optique standard. Après une description détaillée de l'algorithme de segmentation, la précision de la méthode est quantifiée en comparant les images binaires résultantes au résultat d'une segmentation manuelle des images. Nous démontrons ensuite la capacité de notre méthode à extraire des données morphologiques à partir d'images CARS de tissus nerveux. Finalement,

nous présentons le résultat de la segmentation d'une grande mosaïque d'images CARS couvrant plus de la moitié d'une coupe transverse de la moelle épinière d'une souris et montront des preuves de groupes de neurones avec le G-ratios similaires dans la moelle épinière.

5.2 Abstract

A fully automated method for large-scale segmentation of nerve fibers from coherent anti-Stokes Raman scattering (CARS) microscopy images is presented. The method is specifically designed for CARS images of transverse cross sections of nervous tissue but is also suitable for use with standard light microscopy images. After a detailed description of the two-part segmentation algorithm, its accuracy is quantified by comparing the resulting binary images to manually segmented images. We then demonstrate the ability of our method to retrieve morphological data from CARS images of nerve tissue. Finally, we present the segmentation of a large mosaic of CARS images covering more than half the area of a mouse spinal cord cross section and show evidence of clusters of neurons with similar g-ratios throughout the spinal cord.

5.3 Introduction

The nervous system is an immensely complex organ containing a staggering number of interconnected neurons (up to 10^{11}). To function properly, the nervous system requires fast and efficient transmission of electrical signals between neurons. In vertebrates, this is aided by the myelin sheath, a cellular membrane formed by specialized glial cells that is wrapped around axons to increase the propagation speed of the action potentials along these axons Rushton [1951]. There are a number of pathologies that affect myelin and lead to poor conduction as well as irreversible damage to axons Nave [2010], the most widespread being multiple sclerosis where there can be thinning, blebbing or swelling of the myelin. Physical disability results from the accumulation of several types of damage along a given neurological pathway, and consequently, disabilities are apparent only when the disease has progressed significantly. Since local myelin damage is the origin of this macroscopic damage, the investigation of nerve morphology (*e.g.* axon diameter and area, myelin thickness) is of particular interest, as it characterizes damage early on in the evolution of the pathology Dunn et al. [1975].

Nerve fiber morphometry is typically found by imaging cross sections of nerve tissue with a microscope and then identifying and measuring the structures of interest. Traditionally, morphometry was measured manually by an expert using prints or a projection of the images along with a ruler Matthews [1968] or digitalizing tablet Ewart et al. [1989], Friede and Beuche [1985]. Nowadays, the extraction of morphometric information from the myelinated axons that populate an image can be partially or fully automated by transforming the images

into something simpler and more meaningful. This is accomplished through the process of image segmentation, *i.e.* the partitioning of an image into the components of interest. In the case presented here, every pixel of the image must be classified either as axon, myelin, or background.

The application of image segmentation techniques across all imaging modalities in biology and medicine has become a very active field of research in recent years Meijering [2012], Uchida [2013]. Over the last few decades, there have been numerous studies proposing nerve fiber segmentation techniques for optical microscopy images. Semi-automated methods (where human intervention is required at some point throughout the process) are faster than a human expert and have traditionally had the advantage of accuracy over fully-automated methods Mezin et al. [1994], Hunter et al. [2007], More et al. [2011]. The latter are very attractive since they are usually faster than semi-automated methods and are not user-dependent. While most of these methods are based on typical segmentation techniques such as template matching Frykman et al. [1979], edge detection Ellis et al. [1980], Zimmerman et al. [1980], Usson et al. [1991], zonal graph Romero et al. [2000], thresholding Weyn et al. [2005], Urso-Baiarda and Grobbelaar [2006], neural networks Jurrus et al. [2010] and region growing Zhao et al. [2010], Gierthmuehlen et al. [2013], other contributions rely on multiple stage methods using a combination of techniques: elliptical Hough transform followed by an active contour model Fok et al. [1996], multi-level gradient watershed and fuzzy systems Wang et al. [2012]. Li et al. Li et al. [2012] use a classification algorithm (spectral angle mapper) to segment nerve fibers in hyperspectral images.

While the majority of these methods were developed for standard light microscopy images, some were intended to work with transmission electron microscope images Jurrus et al. [2010], Zhao et al. [2010] and scanning electron microscope images More et al. [2011]. To the best of our knowledge, there are only a few studies whereby automated segmentation was developed for nonlinear optical microscopy images to find cell nuclei Hammoudi et al. [2011], Medyukhina et al. [2012, 2013] and none to extract nerve fiber morphology. Moreover, the issue that is central to segmentation of microscopy images is that optical modalities, especially nonlinear techniques, are very sensitive to fine spatial and molecular details in samples. This is a double-edged sword: it is the strength that justifies their development, but it is also the Achilles heel of the resulting images: inhomogeneities in intensities on the scale of microns are quite common, especially *in vivo*, and render many standard image segmentation strategies used in surveillance, magnetic resonance imaging, positron emission tomography, and other fields very difficult to apply.

Over the last decade, a microscopy technique particularly well suited to myelin imaging has gained wide acceptance. Coherent anti-Stokes Raman scattering (CARS) microscopy is a nonlinear optical technique Zumbusch et al. [1999a], Evans and Xie [2008], Bégin et al. [2009] that uses the endogenous contrast provided by molecules already present in the sample of

interest: *i.e.* the contrast can be tuned to the myelin lipid content Wang et al. [2005]. Since then, it has been used to visualize demyelination Fu et al. [2007b], Imitola et al. [2011], Fu et al. [2011], Shi et al. [2011], Freudiger et al. [2012], and we have proposed several techniques to characterize myelin morphology Bélanger et al. [2009a, 2011], Bégin et al. [2013].

The present work sets out to develop strategies for segmentation of CARS microscopy images to be used for myelin characterization. Therefore, the primary objective of this article is to present a fully automated nerve fiber segmentation methods designed specifically for CARS microscopy images of transverse sections of nervous tissue. After a brief outline of the imaging method, we present the details of the segmentation strategy. Then, the accuracy of the proposed segmentation method is quantified. Finally, we conclude by presenting how this method can be used to successfully extract nerve fiber morphology information from large-scale CARS images.

The MATLAB code implementing this analysis in addition to all of the data used is made available on the group web site at http://www.dcclab.ca.

5.4 Materials and methods

5.4.1 Tissue preparation

C57BL/6 adult mice, 25 to 30 g of body weight, were intracardially perfused with 0.1 M phosphate buffer solution (PBS) followed by 4% paraformaldehyde (PFA). The whole spinal cord was dissected from each mouse and fixed flat in 4% PFA overnight. The spinal segment of interest was isolated from the spinal cord, embedded in low gelling temperature agarose, and 350 μm thick transverse sections were made with a vibratome (Leica, VT 1000). Slices were rinsed several times with 0.1 M PBS solution and then mounted inside a spacer on a slide. The remaining space was filled with 0.1 M PBS and a coverslip was mounted on top of the spacer. All experimental procedures have been performed in accordance with guidelines from the Canadian Council on Animal Care.

5.4.2 CARS microscopy

Image acquisition is performed using a custom video-rate laser scanning microscope based on a fast rotating polygonal mirror. Our microscope allows for a maximum image acquisition rate of 30 frames per seconds at 500×500 pixels or 752×500 pixels. Coherent anti-Stokes Raman scattering (CARS) is used to image the myelin sheaths surrounding the axons by probing the CH_2 symmetric stretch vibrations of lipids at 2845 cm^{-1}. This is achieved using a 1064 nm beam from a Nd:Vanadate mode-locked laser overlapped in space and time with a second beam from an optical parametric oscillator tuned to 816.8 nm. In order to reduce the acquisition noise, images are typically averaged over 15 to 30 individual frames. More

details about the system can be found in a previous article by Veilleux et al. Veilleux et al. [2008].

Large-scale mosaic acquisitions of spinal cord cross sections

Imaging an entire cross section from a mouse spinal cord, which typically spans a few mm in diameter, can require as many as 800 images to cover the whole area. Our strategy involves scanning the surface by moving the sample over an x-y grid sequence with an overlap of 20 % of the image field of view (FOV). For each position, the sample is imaged at various depths to form z-stacks which are later stitched together Preibisch et al. [2009] to generate a 3D mosaic. Finally, the surface plane of interest is extracted from the 3D mosaic Bégin et al. [2013] to form the 2D mosaic suitable for the segmentation analysis. A complete mosaic of 5000×7000 pixels (typical) and 0.225 μm spatial resolution is typically acquired in 3.5 hours.

Image processing

The relatively wide FOV of the microscope brings undesired illumination variations across the image. For this reason, the images are processed using contrast-limited adaptive histogram equalization Zuiderveld [1994] to minimize the effect of inhomogeneous illumination on the segmentation results. This method is used on small regions of the image to enhance the contrast such that the histogram of the region matches that of a specified distribution. We found that a uniform target distribution within 16×16 pixel regions improves the segmentation results significantly.

An example of a myelin CARS image of a transverse spinal cord section from a healthy mouse is shown in Fig. 5.1. The image is split in two to show a section from the raw unprocessed image (Fig. 5.1(a)) and a section preprocessed with contrast-limited adaptive histogram equalization (Fig. 5.1(b)).

5.5 Segmentation strategy

Segmentation, *i.e.*, the task of classifying each pixel and assigning it to a meaningful object, may range from trivial to challenging. Pixel classification is highly dependent on how pixels of a different nature appear differently in an image (contrast). In addition, assignment of the classified pixels to distinct objects depends on how well separated the objects are in an image (*i.e.*, if their pixels are touching or not). In the case where high-contrast objects are isolated, segmentation is often trivial. In optical microscopy, however, images contain many low-contrast objects that are touching. Information about the system under study (expected morphology, detection noise, spatial resolution, etc.) is therefore used to inform pixel classification and assignment. In the case of CARS images of nerve fibers in transverse tissue sections, we make use of the following information: 1) the signal is only produced by

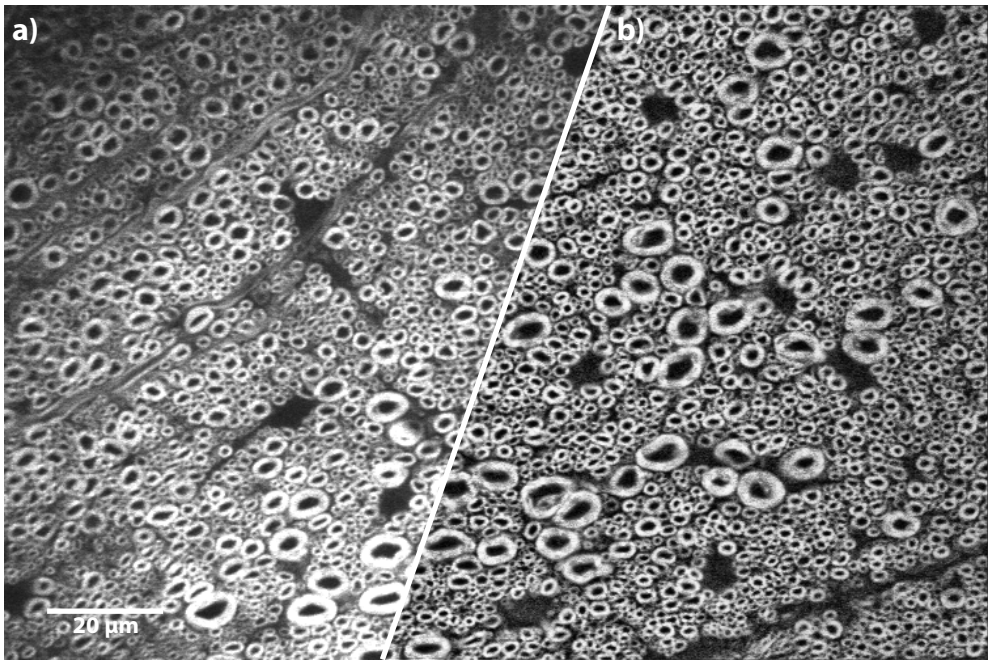

Figure 5.1 – Myelin CARS image of a transverse spinal cord section from a healthy mouse split in two to show a raw unprocessed image section (a) and a section preprocessed with contrast-limited adaptive histogram equalization (b). The image is 752 × 500 pixels in size and an average of 30 frames.

myelin, 2) a myelinated axon does not touch other axons since it is wrapped inside a myelin sheath, 3) the shape of the exterior myelin boundary is similar to the axon boundary, and 4) adjacent myelinated fibers are in contact but do not overlap. With those facts in mind, we devised a two-part strategy whereby the axon candidates are first segmented and the collected information is then used to determine the myelin outer boundary, which in turn serves to unambiguously identify axons.

The challenge with axon segmentation lies in the fact that they are defined by an absence of signal in the images. Therefore, finding dark regions will invariably lead to true axons as well as inter-nerve-fiber background labeled as axon candidates. The axon segmentation is divided into three steps: 1) groups of pixels corresponding to a local minimum of at least a certain depth (extended-minima algorithm) are identified as axons candidates regardless of their shape, 2) their shape is refined through an iterative deformation process (active contour algorithm) 3) the axon candidates are subjected to a first validation test that aims to identify and remove inter-nerve-fiber background based on morphological properties. The result is a binary image of the remaining axon candidates and another image of the background.

The challenge with the myelin segmentation is to accurately identify the outer myelin boundary in images where most myelinated axons are touching each other. To achieve this goal,

we probe the image around each axon candidate and use the information contained in the binary images of the other axons as well as the background to limit the search space. The myelin segmentation strategy comprises three steps: 1) the myelin outer boundary of axon candidates is detected in the straightened subspace image when the intensity changes from high to low, 2) the candidates are subjected to a second validation test based on the area overlap between neighboring nerve fibers, and 3) all unique pairs of touching segmented myelin are pairwise separated using a watershed algorithm. After completing these steps, we have a new binary image representing myelin sheaths around axon objects with no connectivity between them, as well as updated binary images of the axons and the background from the validation step.

A block diagram of the previously outlined method is shown in Fig. 5.2. Specific details describing individual steps are in the sections to follow.

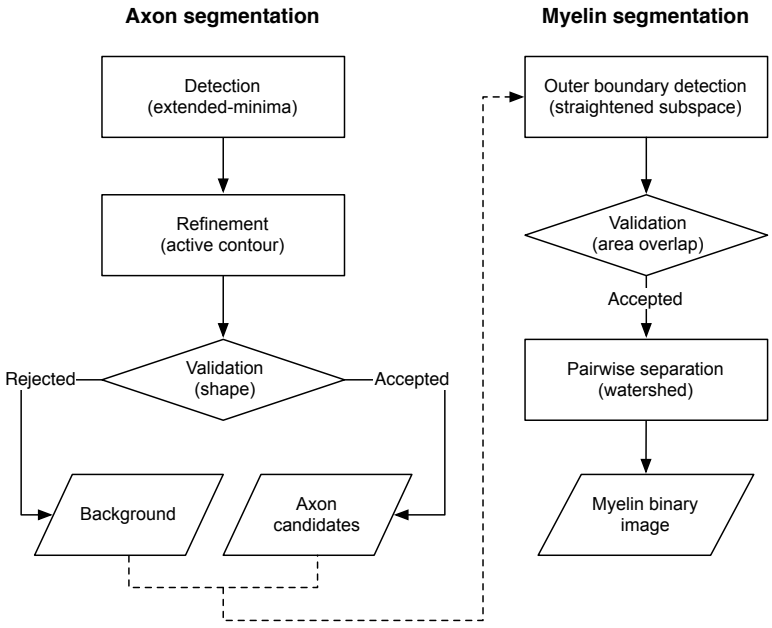

Figure 5.2 – Flow chart of the two-part algorithm. (Left) Axon segmentation: 1) detection of axon candidates by extented-minima transform, 2) shape refinement with an active contour method and 3) candidate validation based on their shape. This part produces two binary images of the axon candidates and the background. (Right) Myelin segmentation: 1) segmentation of the myelin outer boundary in the straightened subspace images of the axon candidates, 2) candidate validation based on area overlap and 3) separation of touching myelin pairs by watershed technique. The final output is a binary image representing the myelin sheaths.

5.5.1 Axon segmentation

Axon detection with extended-minima transform

Initial axon segmentation is obtained by looking for regional minima of at least a certain depth (intensity) in the image. This is accomplished by computing the H-minima transform of the contrast enhanced image and then finding the regional minima. The H-minima transform removes all minima with a depth of less than a certain value (h). The value of h can be set empirically by trial and error on a typical image portion and we found that a value of h on the order of the image intensity standard deviation offers a good starting point. Following the H-minima transform, all pixels with a uniform intensity that are surrounded by higher intensity pixels are extracted as connected components to form the objects populating the initial segmentation.

As shown in Fig. 5.3(a), the output of this step is a binary image containing seeds for all of the axons as well as possible false positives. The objects in the binary image are called seeds because they only approximate the shape of the underlying object.

Axon segmentation refinement with active contour method

In this step, the shapes of the seed objects resulting from the initial segmentation are refined through a deformation process known as "active contour" Kass et al. [1988]. Active contour methods are used to better separate the foreground from the background by allowing an initial curve to deform iteratively so as to minimize a function defined in terms of the contour internal and external energies. The external energy often comprises image forces such as the intensity or gradient while the internal energy usually relates to curve elongation or bending.

Classically, energy functional defined based on the image gradient and curve evolution relies on an edge detector to find the presence of the object boundary. In this work, we use an active contour method whereby the energy describes the foreground and background in terms of their mean intensity Chan and Vese [2001]. The so called Chan-Vese method is better suited to detecting objects with smooth or discontinuous boundaries, with or without gradient.

Our segmentation algorithm was developed to analyze very large images containing many thousands of objects. While computational speed is not the most crucial factor, computation time has to be kept in check. This is especially true in this step where all the objects found by the initial segmentation are refined individually. Furthermore, when using the typical framework (level set Sethian [1999]), active contour methods are notoriously slow to compute. Fortunately, a much more efficient framework called the sparse field method Whitaker [1998] exists with drastically decreased computation time. The main drawback of this framework is that it is not possible for new a curve to appear spontaneously. In our workflow however, this is not a limitation since the goal of this step is to improve the shape of a previously found object.

While there exist many implementations of the Chan-Vese active contour algorithm, we settled on an implementation that also uses local image statistics to define the energy functional Lankton and Tannenbaum [2008] which helps to segment objects that cannot easily be distinguished using global statistics. For every point along the curve, the foreground and background are described in terms of smaller local regions of radius r. A radius value of 10 pixels was used throughout this work.

The number of iterations is set to 100 even if shape refinement usually converges to the correct solution in fewer iterations. The regularization term controlling curve smoothness is set to 0.1 (between 0 and 1, where 0 indicates no penalty for arc length of the curve).

All objects touching the image border or containing less than 10 pixels are removed because their morphological properties cannot be accurately measured. The lower size limit was found with a simulation where the image of a circle of known radius was reduced in size until the error on the measured radius became significant.

At the completion of this stage of the analysis, we now have a binary image containing axon candidates whose shapes were refined to better represent the underlying image properties (Fig. 5.3(b)). This image contains true axons as well as a large number of false positive in areas between the myelinated axons.

Axon validation using morphological properties

The main objective of the axon validation stage is to eliminate false positives from the binary image of axon candidates. The validation is based on morphological properties that were chosen based on their ability to separate true axons from false positives.

To determine an optimal set of properties, we measured a total of ten morphological parameters for over 10,000 axons identified manually in eight CARS images. Next, we examined all possible combinations of parameters taken one to ten at a time. The data was standardized (zero mean and unit variance) to account for the difference in range of the parameters. Using the squared Euclidean distance of an object to the origin of the parameter set space as a common metric, the optimal set was chosen based on its ability to discern false positives from true axons.

The optimal set is composed of four parameters: the circularity, the perimeter and area solidity and the concave perimeter fraction. The circularity is defined as $4\pi A/P^2$ and its value is always less than one except for the case of a perfect circle. The perimeter and area solidity are defined in terms of the object's convex hull (CH) as P/P_{CH} and A/A_{CH}, respectively. Both values are less than one for a concave polygon. The concave perimeter fraction, defined as the ratio of the length of the concave perimeter sections to the object perimeter $L_{concave}/P$, is greater than zero for a concave object.

Unfortunately, we found that even the optimal choice of parameters showed an overlap in their distributions for the true and false axons. For this reason, the cutoff (in terms of the square Euclidean distance to the origin of the parameter set space) was chosen conservatively so as to preserve most of the true axons, and a second validation test is introduced later in the analysis. Any object rejected through the validation stage is added to the binary image of the background that is used in the myelin segmentation step. Fig. 5.3(c), shows the axons (green) as well as the background (red) superimposed on the original image.

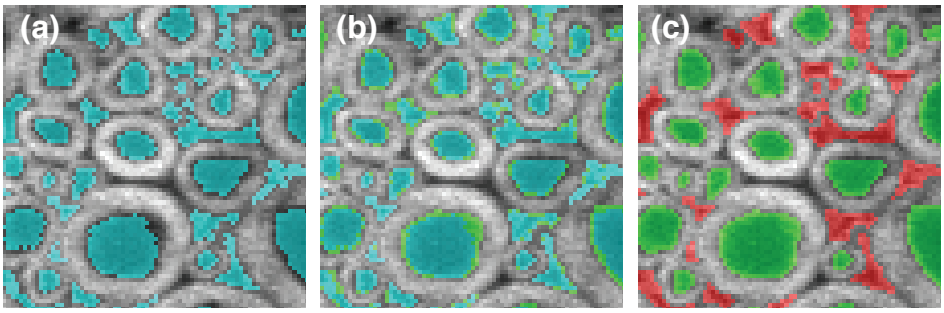

Figure 5.3 – Axon segmentation in a transverse CARS image of mouse spinal cord. (a) Axon detection with extended-minima transform. (b) Segmentation refinement using an active contour method. (c) Object validation separates the axons (green) from the background (red).

5.5.2 Myelin segmentation

Myelin segmentation in the straightened subspace image

Myelin segmentation begins with the creation of a straightened subspace Chav et al. [2009] image around every axon. Because the shape of the myelin outer boundary is in essence a scaled version of the axon shape, this image transformation aims to simplify the segmentation by reshaping the myelin outer boundary in more or less a straight line.

It requires a prior shape which is given by the binary image of the axon. For a given axon, starting from its contour, the image intensity is interpolated along 72 lines radiating outward ($\sim 5^\circ$ step) and perpendicular to the axon boundary. Fig. 5.4(a) shows the probing lines (black) around an axon (green) as well as the binary images of the other axons (blue) and the background (red) overlaid on the processed CARS image. The radial probing is performed on the processed CARS image as well as on the combined binary image of the axons and the background to produce two straightened subspace images. The intensity image is used to find the myelin boundary and the binary image (blue for axons and red for background) is used to restrict its position.

The myelin boundary is expected to coincide with regions where the intensity changes from high to low. Since the boundary is mostly oriented in the straightened subspace image, the Sobel filter is used to produce a cost map that enhances the edges along the direction per-

pendicular to the boundary. However, because the myelinated axons are so tightly packed, clear edges are not always present along a line of sight linking two axons. For this reason, the search space for the boundary is restricted using prior knowledge collected during the axon segmentation. *i.e.*, it is prohibited from going through pixels previously labeled as background or axons.

Once this is done, the boundary is found with a combination of three approaches. The first uses a minimal-path algorithm Vincent [1998] to extract a low-cost path made continuous by extrapolating over fragmented edge sections, and has only one parameter controlling the linearity of the path. Although it usually extracts the expected solution, it favors low-cost solutions without considering their distances from the axon surfaces. Because of the way in which the straightened subspace images are created, higher cost solutions closer to the axon surface will sometimes generate more accurate solutions. Thus, either we look for the first minima along all the probed lines starting from the axon surface, or we look for the first minima lower than a specified cost threshold. The best of these three solutions is found based on their linearity by computing the standard deviation of the distances from the axons along the paths and choosing the solution with the smallest variation. The minimal-path algorithm is favored about 60% of the time. An example of the solution for the myelin outer boundary is shown in Fig. 5.4(b) as an overlay (green line) on the Sobel-filtered intensity image of the straightened subspace with the other axons and the background in blue and red.

Finally, once the myelin boundary is found, it is projected back to the original image space to form a polygon centered on the axon. The polygon is then smoothed using a spline function and is used to create a binary mask (Fig. 5.4(c)) that is stored in a list.

Myelin validation using area overlap

The guiding principle for this stage of the validation is that a properly segmented myelin outer boundary should have little to no overlap with neighboring myelinated axons. Therefore, the degree of overlap can be useful to reject false positives that could not be differentiated from true axons based on their morphology during the axon validation stage. The overlap fraction (Λ) is defined for a given candidate as the ratio of the overlapping myelin area to the total myelin area.

The first step in the myelin validation procedure is to compute the overlap fraction for all objects and place those with a value of Λ above a certain threshold in a candidate buffer. Starting with the objects having the highest overlap fraction, we re-compute the value of Λ to account for objects previously removed from the buffer and dismiss the object if Λ is still above the threshold. The threshold value was determined empirically ($\Lambda_T = 40\%$) so as to maximize the gain in precision while minimizing the loss of sensitivity. An example is shown in Fig. 5.4(d) where the overlapping area is shown in yellow. In this case, the newly

identified false candidate (red) has an overlap fraction well above the threshold and is easily separated from the true candidates (green).

Separation of touching myelin pairs

Now that the myelin boundaries have been segmented and most of the non-axons removed, we need to make sure that none of the objects are connected in the final binary image. Separating touching objects is generally regarded as a difficult task, but here the problem is drastically simplified with the *a* priori knowledge of the number of true objects. The robust separation of touching myelin is obtained by processing the objects one pair at a time using a marker-controlled watershed segmentation algorithm.

The first step consists of finding all the pairs of connected myelin and to process them two at a time (Fig. 5.4(e)). The convex hull of each object is computed to help prevent issues associated with over-segmentation. The two convex hulls are combined to form a single object and the Euclidean distance transform of the resulting binary image is computed. The foreground is marked to zero using the binary images of the related axons and the watershed function is invoked to separate the image into two domains (Fig. 5.4(f)). Finally, once this procedure has been done for all connected pairs, the watershed lines are used to produce a binary image where none of the segmented myelin is connected (Fig. 5.4(g)).

5.5.3 Segmentation accuracy

The accuracy of the proposed segmentation method is quantified by comparing the binary images produced at different stages of the algorithm to a ground truth. The ground truth was created manually for the position and shape of the axons. Through this process, the true positives (TP) and false positives (FP) are identified and two important parameters can be computed: the *sensitivity* and the *precision* of the segmentation. The sensitivity, or the true positive rate (TPR), is given by the ratio of the number of true positives (TP) over the number of objects in the ground truth. The precision, or positive predictive value (PPV), is given by the ratio of the number of true positives over the number of true positives plus the number of false positives (FP), *i.e.*, the total number of segmented objects.

From a binary image resulting from the segmentation step under investigation, the axon candidates are extracted using feature-based boolean logic AND, *i.e.*, objects in the segmentation binary image overlapping objects in the ground truth are selected. Then, the true positives are determined using two criteria based on similarity measures between the object pairs: the modified Hausdorff distance (MHD) Dubuisson and Jain [1994] and the Dice coefficient, also known as the the quotient of similarity (QS) Dice [1945].

The modified Hausdorff distance is a robust measure of similarity that works well for the purpose of object matching. Given two binary objects $\mathbb{A}$ and $\mathbb{B}$ and their boundaries $\mathbb{A}' =$

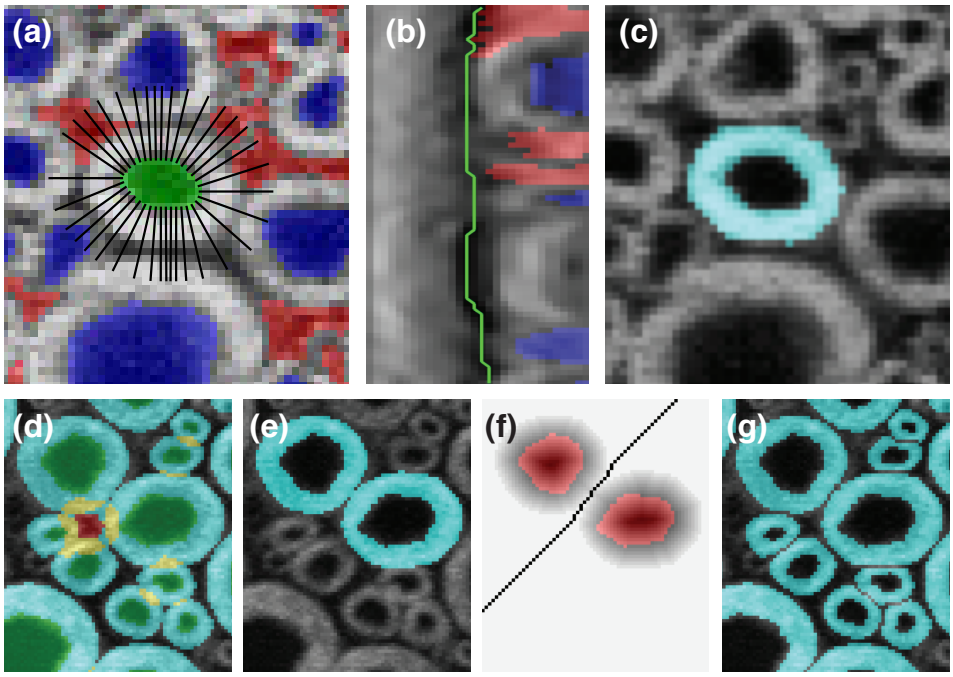

Figure 5.4 – Myelin segmentation in a transverse CARS image of mouse spinal cord. (a) The space around an axon (green) is probed along 72 radial lines to produce a straightened subspace image. (b) Sobel filter of the straightened subspace image with the myelin boundary (green). In both (a) and (b), the other axons are shown in blue and the background in red. (c) Segmented myelin. (d) The myelin validation stages uses the area overlap (yellow) as a metric to separate false (red) from true (green) candidates. (e) Connected objects are separated in pairs using a (f) marker-controlled watershed algorithm. (g) Final binary image with separated nerve fibers.

$\{a_1, ..., a_{N_a}\}$ and $\mathbb{B}' = \{b_1, ..., b_{N_b}\}$, the MHD is defined as:

$$\mathrm{MHD}(\mathbb{A}', \mathbb{B}') = \max(D(\mathbb{A}', \mathbb{B}'), D(\mathbb{B}', \mathbb{A}')) \tag{5.1}$$

$$D(\mathbb{A}', \mathbb{B}') = \frac{1}{N_a} \sum_{a \in \mathbb{A}'} d(a, \mathbb{B}) \tag{5.2}$$

where $d(a, \mathbb{B}) = \min_{b \in \mathbb{B}'} \parallel a - b \parallel$ is the distance between point a and the set of point $\mathbb{B}'$, and $\parallel \cdot \parallel$ indicates the Euclidean distance. $D(\mathbb{A}', \mathbb{B}')$ represents the average distance from $\mathbb{A}'$ to $\mathbb{B}'$ and *v*ice versa. When the objects $\mathbb{A}$ and $\mathbb{B}$ become more similar, the value of the MHD becomes smaller.

The quotient of similarity is defined as:

$$\mathrm{QS}(\mathbb{A}, \mathbb{B}) = \frac{2N(\mathbb{A} \cap \mathbb{B})}{N(\mathbb{A}) + N(\mathbb{B})} \tag{5.3}$$

where $\cap$ is a pixel-based boolean AND and $N(\cdot)$ denotes the number of pixels in a set. The QS value ranges from 0 to 1, where 1 denotes identical objects.

From the visual comparison of the results and the ground truth, it was decided that an object with a MHD value lower than 3 or a QS higher than 0.85 was similar enough to the ground truth to be considered a true positive. Any object not passing the similarity test is labeled as a false positive.

Fig. 5.5 shows a CARS image section with an overlay of the segmentation result that is color-coded to illustrate its comparison with the corresponding ground truth. The true positive axons and the false positive objects are indicated in green and red, respectively. In addition, the false negative axons, *i.e.*, true axons that were rejected by one of the validation stages, are indicated in magenta and axons that were missed entirely in blue. Finally, the segmented myelin is shown in cyan. Any object smaller than 10 pixels was rejected prior to the first validation stage.

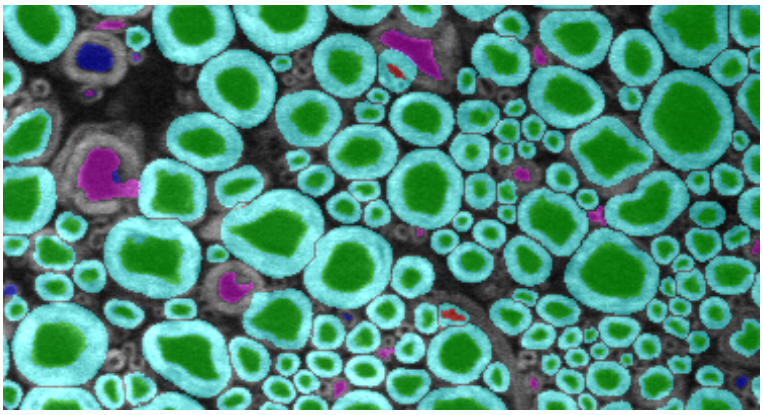

Figure 5.5 – Section of a CARS image with overlay for the true positive axons (green), the false positive objects (red), false negative axons (magenta), missed axons (blue) and segmented myelin (cyan). Objects smaller than 10 pixels were discarded prior to the initial validation stage.

5.6 Results

5.6.1 Segmentation accuracy

The performance of our segmentation strategy was evaluated using a set of eight CARS images and two toluidine blue stained images of transverse spinal cord sections from healthy mice. The accuracy of the proposed method is measured both at the end of the axon refinement stage and after the two validation stages. This is summarized in Table 5.1.

Results shown in the "Refinement" columns in Table 5.1 indicate that the segmentation is

extremely sensitive, missing only a few percent of the axons present in the ground truth. The median similarity value for all true positive objects identified after the refinement stage is 0.85 for the QS and 0.50 for the MHD. This, in conjunction with the visual inspection of the segmentation results, indicates a very good agreement between the axon shapes from the automatic segmentation and the ground truth.

Next, the behavior of the two validation stages is quantified. The axon validation stage (axon validation columns in Table 5.1) was designed to remove as many of the false positives as possible without significantly altering the sensitivity. A normalized distance threshold of 15 leads to a gain of 20% to 30% in precision in exchange for a decrease of no more than 2% in sensitivity. Finally, with the myelin validation stage (myelin validation columns in Table 5.1), the segmentation precision is increased to about 95% while the final sensitivity is reduced by ∼10%.

		Refinement				Axon validation		Myelin validation	
Images	Ground Truth	Detected Objects	TP	TPR (%)	PPV (%)	TPR (%)	PPV (%)	TPR (%)	PPV (%)
CARS 1	1002	1644	982	98	60	94	80	84	94
CARS 2	1310	2055	1251	95	61	94	83	86	95
CARS 3	1256	2007	1236	98	62	98	84	88	94
CARS 4	1504	2231	1463	97	66	96	87	89	97
CARS 5	1487	2312	1476	99	64	98	83	88	95
CARS 6	559	937	543	97	58	95	88	90	96
CARS 7	976	1552	936	96	60	93	83	85	95
CARS 8	1437	2110	1360	95	64	94	87	87	97
TB 1	1178	1905	1170	99	61	93	80	89	94
TB 2	2023	2563	1913	95	75	91	87	80	96

Table 5.1 – The segmentation accuracy was evaluated using a set of eight CARS images and two toluidine blue stained images of transverse spinal cord sections from healthy mice. True positives (TP) and false positives (FP). The sensitivity, or the true positive rate (TPR), is given by the ratio of the number of true positives (TP) over the number of objects in the ground truth. The precision, or positive predictive value (PPV), is given by the ratio of the number of true positives over the number of true positives plus the number of false positives (FP), *i.e.*, the total number of segmented objects.

5.6.2 Morphology

This section showcases the ability of our method to retrieve morphological data from large mosaic images of nerve tissue. In particular, we used a cross section from the cervical region of the spinal cord from a healthy mouse. The cross section, approximately 1.7 mm in diameter, required 324 images to cover approximately 60% of the surface. Our nerve fiber segmentation algorithm revealed around 32,000 myelinated axons in the spinal cord white

matter. For each nerve fiber, standard morphometric measurements are computed from the segmentation results. From the two primitive parameters measured directly on the binary image (axon and fiber area), three parameters can be derived (*i.e.* axon and fiber equivalent diameter, and g-ratio). The equivalent diameter is defined as the diameter of a circle that has the same area as the object. The g-ratio, defined as the ratio of the axon diameter to the fiber diameter (*i.e.*, axon plus myelin sheath), is computed from the equivalent diameters. The result of our segmentation is presented in Fig. 5.6(a) where the 32,000 myelin sheaths are shown as an overlay color coded for the g-ratio. Such an overview can be useful to see large-scale organization such as the concentration of higher g-ratio fibers around the anterior median fissure on the ventral side of the spinal cord (middle bottom) or the cluster of low g-ratio fibers in the middle of the spinal cord on the dorsal side (middle top). A zoomed-in view of a region of interest (blue rectangle) is presented in Fig. 5.6(b). The g-ratio follows a normal distribution with an average of 0.5 and standard deviation of 0.1. In Fig. 5.6(c) and (d), we present typical parameter couples as 2D histograms. A small sub-distribution is noticeable in both histograms: it includes a very small fraction ($< 1\%$) of fibers for which the myelin outer diameter is underestimated (see arrows in Fig. 5.6(b)). This double ring structure could be the result of a preparation artifact, but it is also consistent with the appearance of Schmidt-Lanterman incisures in transverse cuts Ross and Pawlina [2006]. The algorithm makes no attempt at handling these rare cases differently.

5.7 Conclusion

We have shown in this manuscript how we can extract nerve fiber morphometric information from CARS images of nervous tissue. Valuable information is readily obtained from these images using an automatic segmentation algorithm developed specifically for the task of classifying each pixel as myelin, axon, or background, as well as assigning it to a given nerve fiber. The critical aspect for success was to recognize that pixel classification needs to be informed by the geometry before being considered final, and that the geometry is highly specific to the problem at hand. We have proceeded by first identifying axon candidates which are then filtered based on shape parameters to remove obvious false positives. In the second stage where myelin pixels are identified, if the resulting myelin conflicted with the myelin from other axons, the myelin sheath with the most conflicts was assumed incorrect, while the others were confirmed as myelin. The algorithm was tested against manually segmented images with great success. Finally, it was used for the robust segmentation of large-scale CARS images where local clusters can be recognized. In future work, we plan to use this method to both quickly and accurately measure small changes in myelination in the earliest stages of demyelinating diseases such as multiple sclerosis, which will dramatically improve our understanding of the initiation of such debilitating diseases.

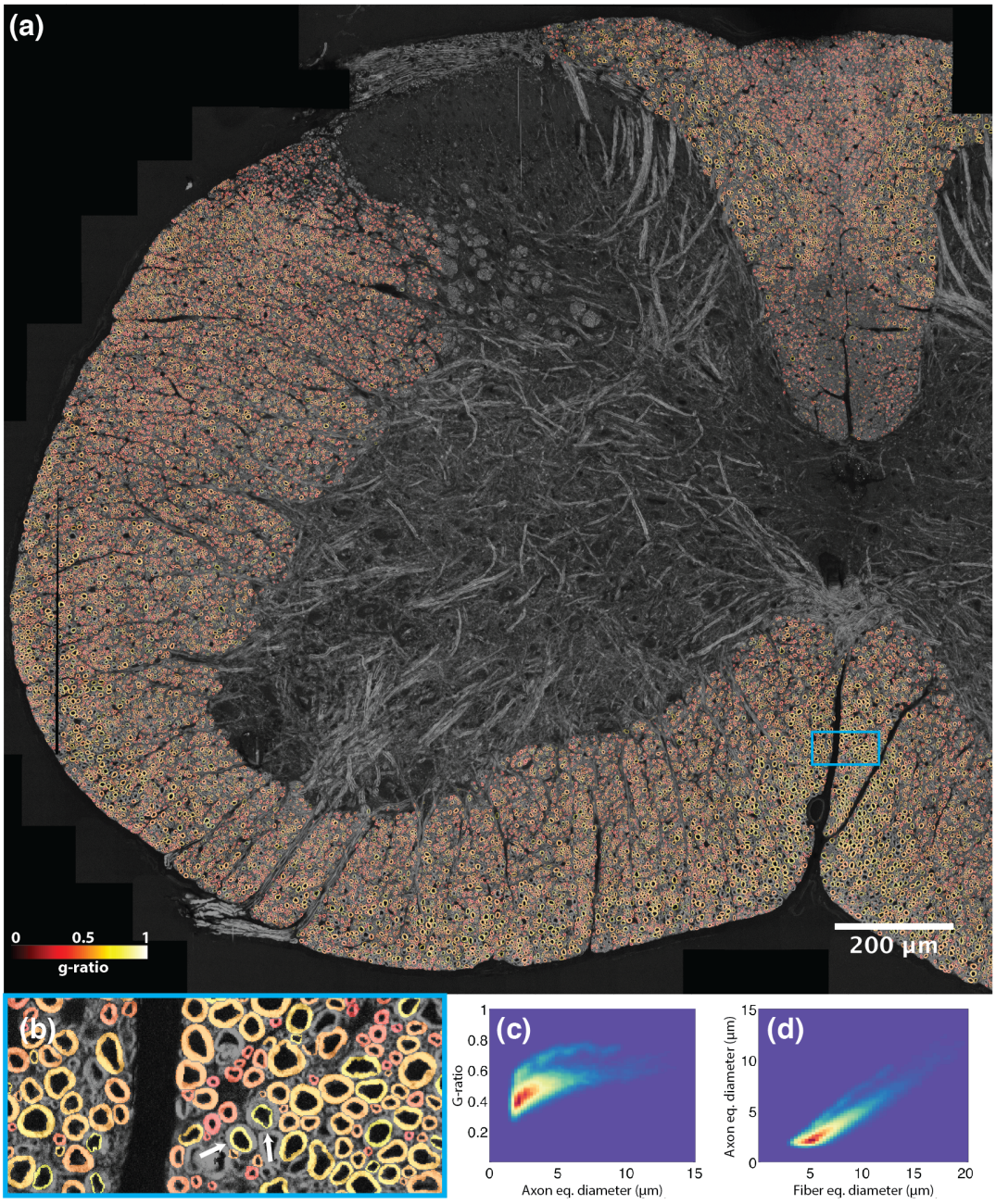

Figure 5.6 – Nerve fiber segmentation in a CARS mosaic from a transverse section of healthy mouse spinal cord. (a) Myelin sheaths are shown as an overlay, color-coded to the value of the g-ratio. (b) Zoomed-in view of the blue region of interest around the anterior median fissure on the ventral side of the spinal cord. The white arrows show examples where the myelin outer diameter is underestimated. Morphometric parameter 2D histograms of (c) the g-ratio versus axon equivalent diameter and (d) axon equivalent diameter versus fiber equivalent diameter.

Conclusion

The main goal of this thesis was to overcome some of the obstacles hampering the wide-scale adoption of CARS as a microscopy technique. The three innovative findings presented in this thesis in the form of original publications provide a definitive proof that this objective has been achieved successfully. This last chapter proposes to summarize briefly those findings, expose their limitations, bring suggestions for their improvement, and finally suggest some recommendations for future experiments.

In chapter 3, we presented a novel fiber laser system consisting of a pump laser synchronized with a rapidly tunable programmable laser for the rapid acquisition of CARS spectral images in thick tissue. This new system represented a major improvement over previous attempt at CARS spectral imaging especially for experiments requiring that the signal is collected in the epi-direction as is the case when looking at thick tissue sections. The quality of our work as been noticed by the community as is reflected by the 34 citations over the last three years. The most distinctive feature of this system is its ability to access Raman lines over a significant fraction of the high-wavenumber region (2700-2950 cm^{-1}) at rates of up to 10,000 spectral points per second. While we successfully demonstrated the acquisition of CARS spectra, images and spectral images in thick tissue, the early prototype used for those experiments had a few shortcomings. Its most important limitation comes from the high level of laser noise which in turn limits the detection sensitivity. Because it comes from many sources, reducing the noise level has been very challenging so far. Two important factors were identified through our experiments: 1) the general reliance on high speed electronics, in particular the active mode locking scheme, is responsible for a significant fraction of the laser noise, and 2) the erbium-doped fiber gain dynamics has an important role to play in the matter. Possible solutions currently investigated by the team at Genia include refining the electronics as much as possible and changing the gain medium for semiconductor optical amplifier which have better noise characteristics. As well, a collinear balanced detection detection scheme has been used successfully for noise suppression in fiber laser [Nose et al., 2012] and could possibly be useful here. Other possible improvements include moving the current operating wavelengths of the laser towards the visible. This would benefit the detection sensitivity as well as enable the use of more conventional optics (lens, filters, microscope objectives) designed for standard optical microscopes operating in the visible.

Shortening the pulse length (∼5–10 ps) would be favorable for the excitation efficiency and strategies to shorten the pulses using a shorter pulse generator or a time-lens scheme are being explored. With these improvements in place, we believe this system will be poised to become a major player in the CARS microscopy field.

The initial motivation for the CARS spectral imaging project comes from the large amount of literature related to the *in situ* diagnostic potential of Raman spectroscopy, especially in oncology. However, for a Raman based technique to become clinically relevant, its sensitivity would have to increase by many orders of magnitudes, which is exactly what was achieved with our CARS spectral imaging system. The first experiment that we plan to conduct with the next generation prototype is to explore the diagnostic potential of CARS spectral imaging for brain cancer. In order to do this, we will use our system to acquire spectral images of fixed slices of human brain tissue from biopsies previously graded by a trained pathologist. A fraction of the data from the spectral images will be used in conjunction with the grades to build a diagnostic model that will then be tested against the rest of the data to measure its predictive power. Since the start of this project, a large fraction of the research in our group became focused on the understanding of multiple sclerosis through the use of animal models such as EAE and our video-rate microscopy platform. Little is known about the onset of this disease, in part because we are still unsure what to look for and where, but also because by the time a lesion becomes apparent on an image, most of the damage is already done and it is too late to learn much. For this reason, we have worked on different strategies to increase our detection sensitivity to changes in the myelin structure in early stages of the disease. So far, most of our efforts relied on polarimetric CARS, but it is clear that CARS spectral imaging may provide key informations for the identification of early lesions.

In chapter 4, we proposed a new method based on a two-dimensional Fourier transform to quantify and measure the local organization of myelinated axons in the spinal cord. This contribution was significant mainly because it represents the first attempt to characterize quantitatively the tissue architecture of nerve fibers as well as one of the rare quantitative image analysis techniques for CARS images. We have shown how this analysis can be useful to study the organization/disorganization in the myelin structure from spinal cord of animals afflicted by EAE, a common animal model of multiple sclerosis. A current limitation of the procedure is that its current implementation in Matlab cannot be used in real time but only as a post-acquisition analysis. Conceptually however, this procedure is compatible with live animal imaging and now that most of the development has been done, it only needs to be ported to *iPhoton*, the home-made acquisition system used throughout the lab for *in vivo* CARS experiments.

Once a real-time version of the software has been implemented, it could be used in conjunction with a minimally invasive microendoscopic approach [Bélanger et al., 2012] to follow the evolution of a given region of interest over time. Such an experiment would also permit

to measure a more extensive set of functional parameters (blood-brain-barrier permeability, cellular recruitment, microglial activity, etc...) with the context provided by the localization and degree of severity of the lesions. This would provide valuable informations that would undoubtedly help understand the sequence of the interaction between all the key players in EAE. Moreover, myelin disruption is clearly related to nerve function but it is not a direct measurement of a nerve functional integrity. Hence, we propose another set of experiments that could be used to build a more complete model relating myelin disruption to loss of nerve function. Such a model would need to consider the number, size and most importantly localization of the moderate to severe lesions throughout the entire spinal cord. While the acquisition of CARS microscopy maps of the complete surface of the spinal cord is currently out of reach with our microscopy platform, the necessary functionalities are being put into place by other members of the lab. Some key elements that are being addressed include acquisition and mapping speed, conservation of the spinal cord during the experiment, and proper handling of the curvature of the surface during the acquisition since the spinal cord is roughly cylindrical in shape. For the near future however, the surface of multiple spinal cords could be undersampled at the microscope and analyzed using the automated technique presented in chapter 4 to build a draft of the model.

In chapter 5, we presented a fully-automated method for the segmentation of nerve fibers in CARS images from transverse sections of nervous tissue. While methods for the characterization of myelin morphology have been around for a long time, this is the first technique that was developed specifically for CARS microscopy and can consequently benefit from the many advantages offered by CARS such as minimal preparation and good specificity to myelin. Our algorithm can be used to quickly and accurately extract nerve fiber morphometric information from large-scale mosaic images containing many thousands of myelinated axons. Image segmentation is often regarded as one of the most challenging task in image analysis and this particular project has certainly been true to that statement. As a consequence, there are still many aspects of our procedure that require some work. For instance, the analysis is fully automated but it initially requires tuning of eleven parameters that can influence the result to various extents. Reducing the number of parameters would greatly enhance the usability of the method. As well, because it is relatively difficult for a user to see the effect of varying those parameters and therefore make an optimal choice, providing an interface for the exploration of the parameter space would be a great addition. Another current limitation concerns the first validation stage. As we have shown, the initial sensitivity of the method is almost 100%, but its precision is much lower ($\sim$60%). The aim of the validation stage is to recover as much of the precision as possible without reducing the sensitivity. This has proved to be the most challenging task of this particular project for two reasons: 1) the shape of the real axons is roughly circular but can vary significantly, 2) the shape of the false positives is not constrained by particular biological structures and can take any shape, even circular. As a consequence, every shape parameter that was tried showed an overlap in

the distributions for the true and false axons and no parameter combination enables a clean separation between the two groups with the current threshold method. One solution that could possibly improve the validation stage involves the use of fuzzy logic to remove false positive since it is particularly well suited to deal with the notion of partial truth. However, the validation stage currently relies only on the shape of the axon candidates in the binary image. Hence, it might be more advantageous to explore other metrics based on the brightness values or textures of the pixels belonging to the axon candidates or even to the area surrounding them.

Manual or even semi-automated segmentation of myelinated axons is such a labor-intensive endeavor (many seconds per nerve fiber) that histomorphology studies relying on such methods have to restrict significantly the number of segmented nerve fibers. Because our method provides a way to automatically collect morphological data from images of nervous tissue, it removes the necessity to make compromises on the number of segmented nerve fibers. This opens the door to histomorphology analysis of large areas of nervous tissue which should be useful for a wide range of applications including studies of nerve structure and their response to injury or drugs. For instance, with the video-rate CARS microscope available in our lab, it should be possible to quickly acquire mosaic of images covering the complete surface of the spinal cord or nerves of humans or other large animals. Moreover, comprehensive whole-nerve analysis should allow for an accurate description of the nerve fiber population within the nerve, may permit the identification of subtle differences between specimens of different gender, or supply valuable informations in studies striving to understand the early stages of demyelinating diseases such as MS.

Bibliography

M. Balu, G. Liu, Z. Chen, B. J. Tromberg, and E. O. Potma. Fiber delivered probe for efficient CARS imaging of tissues. *Opt. Express*, 18(3):2380–2388, 2010.

P. R. Barber, B. Vojnovic, G. Atkin, F. M. Daley, S. A. Everett, G. D. Wilson, and J. D. Gilbey. Applications of cost-effective spectral imaging microscopy in cancer research. *Journal of Physics D: Applied Physics*, 36(14):1729–1738, July 2003.

E. Beaurepaire, M. Oheim, and J. Mertz. Ultra-deep two-photon fluorescence excitation in turbid media. *Opt. Commun.*, 188:25–29, 2001.

S. Bégin, E. Bélanger, S. Laffray, R. Vallée, and D. C. Côté. In vivo optical monitoring of tissue pathologies and diseases with vibrational contrast. *J. Biophotonics*, 2(11):632–642, Nov. 2009.

S. Bégin, E. Bélanger, S. Laffray, B. Aubé, E. Chamma, J. Bélisle, S. Lacroix, Y. de Koninck, and D. Côté. Local assessment of myelin health in a multiple sclerosis mouse model using a 2D Fourier transform approach. *Biomed. Opt. Express*, 4(10):2003–2014, 2013.

E. Bélanger, S. Bégin, S. Laffray, Y. de Koninck, R. Vallée, and D. C. Côté. Quantitative myelin imaging with coherent anti-Stokes Raman scattering microscopy: alleviating the excitation polarization dependence with circularly polarized laser beams. *Opt. Express*, 17(21):18419–18432, Oct. 2009a.

E. Bélanger, S. Bégin, S. Laffray, Y. De Koninck, R. Vallée, and D. C. Côté. Quantitative myelin imaging with coherent anti-stokes raman scattering microscopy: alleviating the excitation polarization dependence with circularly polarized laser beams. *Opt. Express*, 17(21):18419–18432, 2009b.

E. Bélanger, F. P. Henry, R. Vallée, M. A. Randolph, I. E. Kochevar, J. M. Winograd, C. P. Lin, and D. C. Côté. In vivo evaluation of demyelination and remyelination in a nerve crush injury model. *Biomed. Opt. Express*, 2(9):2698–2708, Sept. 2011.

E. Bélanger, J. Crépeau, S. Laffray, R. Vallée, Y. De Koninck, and D. Côté. Live animal myelin histomorphometry of the spinal cord with video-rate multimodal nonlinear microendoscopy. *J. Biomed. Opt.*, 17(2):021107, Feb. 2012.

S. Beucher and C. Lantuejoul. Use of Watersheds in Contour Detection. In *International Workshop on Image Processing: Real-time Edge and Motion Detection/Estimation, Rennes, France.*, Sept. 1979.

D. A. Brown and P. E. Sawchenko. Time course and distribution of inflammatory and neurodegenerative events suggest structural bases for the pathogenesis of experimental autoimmune encephalomyelitis. *J. Comp. Neurol.*, 502(2):236–260, May 2007.

B. Brozek-Pluska, I. Placek, K. Kurczewski, Z. Morawiec, M. Tazbir, and H. Abramczyk. Breast cancer diagnostics by raman spectroscopy. *J. Mol. Liq.*, 141(3):145–148, 2008.

S. Brustlein, P. Ferrand, N. Walther, S. Brasselet, C. Billaudeau, D. Marguet, and H. Rigneault. Optical parametric oscillator-based light source for coherent Raman scattering microscopy: practical overview. *Journal of Biomedical Optics*, 16(2):021106, 2011.

B. Burgoyne and A. Villeneuve. Programmable lasers: design and applications. In *Proc. SPIE*, volume 7580, pages 758002–758002–15, 2010.

H. Cahyadi, J. Iwatsuka, T. Minamikawa, H. Niioka, T. Araki, and M. Hashimoto. Fast spectral coherent anti-Stokes Raman scattering microscopy with high-speed tunable picosecond laser. *Journal of Biomedical Optics*, 18(9):096009–096009, 2013.

T. F. Chan and L. A. Vese. Active contours without edges. *Trans. Img. Proc.*, 10(2):266–277, Feb. 2001.

R. Chav, T. Cresson, C. Kauffmann, and J. A. de Guise. Method for fast and accurate segmentation processing from prior shape: application to femoral head segmentation on x-ray images. In *SPIE Medical Imaging*, volume 7259, pages 72594Y–72594Y–8, 2009.

B.-C. Chen, J. Sung, and S.-H. Lim. Chemical imaging with frequency modulation coherent anti-Stokes Raman scattering microscopy at the vibrational fingerprint region. *J. Phys. Chem. B*, 114(50):16871–16880, Dec. 2010.

B.-C. Chen, J. Sung, X. Wu, and S.-H. Lim. Chemical imaging and microspectroscopy with spectral focusing coherent anti-Stokes Raman scattering. *J. Biomed. Opt.*, 16(2):021112, 2011.

J. X. Cheng, L. D. Book, and X. S. Xie. Polarization coherent anti-stokes raman scattering microscopy. *Opt. Lett.*, 26(17):1341–1343, 2001a.

J.-X. Cheng, A. Volkmer, L. D. Book, and X. S. Xie. An epi-detected coherent anti-stokes raman scattering (e-cars) microscope with high spectral resolution and high sensitivity. *J. Phys. Chem. B*, 105:1277–1280, 2001b.

J.-X. Cheng, K. Y. Jia, G. Zheng, and X. S. Xie. Laser-scanning coherent anti-stokes raman scattering microscopy and applications to cell biology. *Biophys. J.*, 83:502–9, 2002a.

J.-X. Cheng, A. Volkmer, L. D. Book, and X. S. Xie. Multiplex coherent anti-stokes raman scattering microspectroscopy and study of lipid vesicles. *J. Phys. Chem. B*, 106:8493–8498, 2002b.

J.-X. Cheng, A. Volkmer, and X. S. Xie. Theoretical and experimental characterization of coherent anti-stokes raman scattering microscopy. *J. Opt. Soc. Am. B*, 19:1363–1375, 2002c.

M. V. P. Chowdary, K. K. Kumar, K. Thakur, A. Anand, J. Kurien, C. M. Krishna, and S. Mathew. Discrimination of normal and malignant mucosal tissues of the colon by raman spectroscopy. *Photomed. Laser Surg.*, 25(4):269–274, 2007.

P. D. Chowdary, W. A. Benalcazar, Z. Jiang, D. M. Marks, S. A. Boppart, and M. Gruebele. High Speed Nonlinear Interferometric Vibrational Analysis of Lipids by Spectral Decomposition. *Anal. Chem.*, 82(9):3812–3818, 2010.

R. Cicchi, N. Vogler, D. Kapsokalyvas, B. Dietzek, J. Popp, and F. S. Pavone. From molecular structure to tissue architecture: collagen organization probed by SHG microscopy. *J. Biophotonics*, 6(2):129–142, Feb. 2013.

L. R. Dice. Measures of the Amount of Ecologic Association Between Species. *Ecology*, 26(3): 297, July 1945.

M. P. Dubuisson and A. K. Jain. A modified Hausdorff distance for object matching. In *Proceedings of the 12th IAPR International Conference on Pattern Recognition*, volume 1, pages 566–568, 1994.

M. D. Duncan, J. Reintjes, and T. J. Manuccia. Scanning coherent anti-Stokes Raman microscope. *Opt. Lett.*, 7(8):350–352, Aug. 1982.

R. F. Dunn, D. P. O'Leary, and W. E. Kumley. Quantitative analysis of micrographs by computer graphics. *J. Microsc.*, 105(2):205–213, 1975.

R. C. Ecker, R. de Martin, G. E. Steiner, and J. A. Schmid. Application of spectral imaging microscopy in cytomics and fluorescence resonance energy transfer (FRET) analysis. *Cytometry Part A*, 59A(2):172–181, 2004.

B. Efron and R. J. Tibshirani. *An introduction to the bootstrap*. Chapman & Hall, New York, 1993.

T. J. Ellis, D. Rosen, and J. B. Cavanagh. Automated measurement of peripheral nerve fibres in transverse section. *J. Biomed. Eng.*, 2(4):272–280, Oct. 1980.

C. L. Evans and X. S. Xie. Coherent anti-Stokes Raman scattering microscopy: chemical imaging for biology and medicine. *Annu. Rev. Anal. Chem.*, 1(1):883–909, 2008.

C. L. Evans, E. O. Potma, and X. S. Xie. Coherent anti-stokes raman scattering spectral interferometry: determination of the real and imaginary components of nonlinear susceptibility chi((3)) for vibrational microscopy. *Opt. Lett.*, 29:2923–2925, 2004.

C. L. Evans, E. O. Potma, M. Puoris'haag, D. Côté, C. P. Lin, and X. S. Xie. Chemical imaging of tissue in vivo with video-rate coherent anti-stokes raman scattering microscopy. *Proc. Natl. Acad. Sci.*, 102:16807–16812, 2005.

C. L. Evans, X. Xu, S. Kesari, X. S. Xie, S. T. C. Wong, and G. S. Young. Chemically-selective imaging of brain structures with cars microscopy. *Opt. Express*, 15:12076–12087, 2007.

D. P. Ewart, W. M. Kuzon Jr., J. S. Fish, and N. H. McKee. Nerve fibre morphometry: a comparison of techniques. *J. Neurosci. Meth.*, 29(2):143–150, Aug. 1989.

M. Filippi, M. A. Rocca, F. Barkhof, W. Brück, J. T. Chen, G. Comi, G. DeLuca, N. De Stefano, B. J. Erickson, N. Evangelou, F. Fazekas, J. J. G. Geurts, C. Lucchinetti, D. H. Miller, D. Pelletier, B. F. G. Popescu, and H. Lassmann. Association between pathological and MRI findings in multiple sclerosis. *Lancet Neurol.*, 11(4):349–360, Apr. 2012.

J. Flusser and T. Suk. Pattern recognition by affine moment invariants. *Pattern Recognit.*, 26 (1):167–174, 1993.

Y. L. Fok, J. K. Chan, and R. T. Chin. Automated analysis of nerve-cell images using active contour models. *IEEE Trans. Med. Imag.*, 15(3):353–368, 1996.

C. W. Freudiger, W. Min, B. G. Saar, S. Lu, G. R. Holtom, C. He, J. C. Tsai, J. X. Kang, and X. S. Xie. Label-Free Biomedical Imaging with High Sensitivity by Stimulated Raman Scattering Microscopy. *Science*, 322(5909):1857–1861, Dec. 2008.

C. W. Freudiger, R. Pfannl, D. A. Orringer, B. G. Saar, M. Ji, Q. Zeng, L. Ottoboni, Y. Wei, W. Ying, C. Waeber, J. R. Sims, P. L. De Jager, O. Sagher, M. A. Philbert, X. Xu, S. Kesari, X. S. Xie, and G. S. Young. Multicolored stain-free histopathology with coherent Raman imaging. *Lab. Invest.*, 92(10):1492–1502, Oct. 2012.

R. L. Friede and W. Beuche. Combined scatter diagrams of sheath thickness and fibre calibre in human sural nerves: changes with age and neuropathy. *J. Neurol. Neurosurg. Psychiatry*, 48(8):749–756, Aug. 1985.

G. K. Frykman, H. G. Rutherford, and I. R. Neilsen. Automated nerve fiber counting using an array processor in a Multi-Mini Computer System. *J. Med. Syst.*, 3(1-2):81–94, 1979.

Y. Fu, H. F. Wang, R. Y. Shi, and J. X. Cheng. Characterization of photodamage in coherent anti-stokes raman scattering microscopy. *Opt. Express*, 14(9):3942–3951, 2006.

Y. Fu, H. Wang, T. B. Huff, R. Shi, and J.-X. Cheng. Coherent anti-stokes raman scattering imaging of myelin degradation reveals a calcium-dependent pathway in lyso-ptdcho-induced demyelination. *J. Neurosci. Res.*, 85(13):2870–2881, 2007a.

Y. Fu, H. Wang, T. B. Huff, R. Shi, and J.-X. Cheng. Coherent anti-Stokes Raman scattering imaging of myelin degradation reveals a calcium-dependent pathway in lyso-PtdCho-induced demyelination. *J. Neurosci. Res.*, 85(13):2870–2881, Oct. 2007b.

Y. Fu, T. B. Huff, H.-W. Wang, H. Wang, and J.-X. Cheng. Ex vivo and in vivo imaging of myelin fibers in mouse brain by coherent anti-stokes raman scattering microscopy. *Opt. Express*, 16(24):19396–19409, 2008.

Y. Fu, T. J. Frederick, T. B. Huff, G. E. Goings, S. D. Miller, and J.-X. Cheng. Paranodal myelin retraction in relapsing experimental autoimmune encephalomyelitis visualized by coherent anti-Stokes Raman scattering microscopy. *J. Biomed. Opt.*, 16(10):106006, Oct. 2011.

F. Ganikhanov, S. Carrasco, X. S. Xie, M. Katz, W. Seitz, and D. Kopf. Broadly tunable dual-wavelength light source for coherent anti-stokes raman scattering microscopy. *Opt. Lett.*, 31:1292–1294, 2006a.

F. Ganikhanov, C. L. Evans, B. G. Saar, and X. S. Xie. High-sensitivity vibrational imaging with frequency modulation coherent anti-stokes raman scattering (FM cars) microscopy. *Opt. Lett.*, 31:1872–1874, 2006b.

E. T. Garbacik, J. L. Herek, C. Otto, and H. L. Offerhaus. Rapid identification of heterogeneous mixture components with hyperspectral coherent anti-Stokes Raman scattering imaging. *Journal Of Raman Spectroscopy*, 43(5):651–655, May 2012.

A. Ghazaryan, H. F. Tsai, G. Hayrapetyan, W.-L. Chen, Y.-F. Chen, M. Y. Jeong, C.-S. Kim, S.-J. Chen, and C.-Y. Dong. Analysis of collagen fiber domain organization by Fourier second harmonic generation microscopy. *J. Biomed. Opt.*, 18(3):31105, Mar. 2013.

M. Gierthmuehlen, T. M. Freiman, K. Haastert-Talini, A. Mueller, J. Kaminsky, T. Stieglitz, and D. T. T. Plachta. Computational tissue volume reconstruction of a peripheral nerve using high-resolution light-microscopy and reconstruct. *PLOS ONE*, 8(6):e66191, 2013.

A. F. H. Goetz, G. Vane, J. E. Solomon, and B. N. Rock. Imaging Spectrometry for Earth Remote Sensing. *Science*, 228(4704):1147–1153, June 1985.

A. Gowen, C. Odonnell, P. Cullen, G. Downey, and J. Frias. Hyperspectral imaging – an emerging process analytical tool for food quality and safety control. *Trends in Food Science & Technology*, 18(12):590–598, Dec. 2007.

R. C. Haggitt. Barrett's esophagus, dysplasia, and adenocarcinoma. *Hum. Pathol.*, 25(10): 982–993, 1994.

J. Hagmar, C. Brackmann, T. Gustavsson, and A. Enejder. Image analysis in nonlinear microscopy. *J. Opt. Soc. Am. A Opt. Image Sci. Vis.*, 25(9):2195–2206, 2008.

A. S. Haka, K. E. Shafer-Peltier, M. Fitzmaurice, J. Crowe, R. R. Dasari, and M. S. Feld. Diagnosing breast cancer by using raman spectroscopy. *Proc. Natl. Acad. Sci. U. S. A.*, 102(35): 12371–12376, 2005.

A. A. Hammoudi, F. Li, L. Gao, Z. Wang, M. J. Thrall, Y. Massoud, and S. T. C. Wong. Automated Nuclear Segmentation of Coherent Anti-Stokes Raman Scattering Microscopy Images by Coupling Superpixel Context Information with Artificial Neural Networks. In K. Suzuki, F. Wang, D. Shen, and P. Yan, editors, *Machine Learning in Medical Imaging*, volume 7009 of *Lecture Notes in Computer Science*, pages 317–325. Springer Berlin Heidelberg, Berlin, Heidelberg, 2011.

T. Haraguchi, T. Shimi, T. Koujin, N. Hashiguchi, and Y. Hiraoka. Spectral imaging fluorescence microscopy. *Genes to Cells*, 7(9):881–887, 2002.

R. M. Haralick, K. Shanmugam, and I. Dinstein. Textural Features for Image Classification. *IEEE Trans. Syst., Man, Cybern.,Syst*, 3(6):610–621, 1973.

M. Hashimoto, T. Minamikawa, and T. Araki. High-speed CARS spectral imaging using acousto optic tunable filter. In *Multiphoton Microscopy in the Biomedical Sciences X*, page 11, Feb. 2010.

M. Hashimoto, J. Iwatsuka, H. Niioka, and T. Araki. High-speed spectral tuning cars microscopy using aotf laser. In *Proc. SPIE*, volume 8226, page 82261N, 2012.

T. Hellerer, A. M. K. Enejder, and A. Zumbusch. Spectral focusing: High spectral resolution spectroscopy with broad-bandwidth laser pulses. *Appl. Phys. Lett.*, 85(1):25–27, 2004.

F. P. Henry, D. Côté, M. A. Randolph, E. A. Z. Rust, R. W. Redmond, I. E. Kochevar, C. P. Lin, and J. M. Winograd. Real-time in vivo assessment of the nerve microenvironment with coherent anti-stokes raman scattering microscopy. *Plast. Reconstr. Surg.*, 123(2S):123S–130S, 2009.

D. W. Hetzner. *Comparing binary image analysis measurements-euclidean geometry, centroids and corners*. Microscopy Today, 2008.

M.-K. Hu. Visual pattern recognition by moment invariants. *IEEE Trans. Inf. Theory*, 8(2): 179–187, Feb. 1962.

T. B. Huff and J.-X. Cheng. In vivo coherent anti-stokes raman scattering imaging of sciatic nerve tissue. *J. Microsc.*, 225:175–82, 2007.

D. A. Hunter, A. Moradzadeh, E. L. Whitlock, M. J. Brenner, T. M. Myckatyn, C. H. Wei, T. H. H. Tung, and S. E. Mackinnon. Binary imaging analysis for comprehensive quantitative histomorphometry of peripheral nerve. *J. Neurosci. Meth.*, 166(1):116–124, Oct. 2007.

J. Hutchings, C. Kendall, B. Smith, N. Shepherd, H. Barr, and N. Stone. The potential for histological screening using a combination of rapid raman mapping and principal component analysis. *J Biophotonics*, 2(1-2):91–103, 2009.

T. Ideguchi, S. Holzner, B. Bernhardt, G. Guelachvili, N. Picqué, and T. W. Hänsch. Coherent Raman spectro-imaging with laser frequency combs. *Nature*, 502(7471):355–358, Oct. 2013.

J. Imitola, D. C. Côté, S. Rasmussen, X. S. Xie, Y. Liu, T. Chitnis, R. L. Sidman, C. P. Lin, and S. J. Khoury. Multimodal coherent anti-Stokes Raman scattering microscopy reveals microglia-associated myelin and axonal dysfunction in multiple sclerosis-like lesions in mice. *J. Biomed. Opt.*, 16(2):021109, 2011.

E. Jurrus, A. R. C. Paiva, S. Watanabe, J. R. Anderson, B. W. Jones, R. T. Whitaker, E. M. Jorgensen, R. E. Marc, and T. Tasdizen. Detection of neuron membranes in electron microscopy images using a serial neural network architecture. *Med. Image Anal.*, 14(6):770–783, Dec. 2010.

H. Kano and H.-O. Hamaguchi. Ultrabroadband (>2500 cm-1) multiplex coherent anti-Stokes Raman scattering microspectroscopy using a supercontinuum generated from a photonic crystal fiber. *Appl. Phys. Lett.*, 86:1211–1213, 2005a.

H. Kano and H.-O. Hamaguchi. Near-infrared coherent anti-stokes raman scattering microscopy using supercontinuum generated from a photonic crystal fiber. *Appl. Phys. B*, 80: 243–246, 2005b.

M. Kass, A. Witkin, and D. Terzopoulos. Snakes: Active contour models. *Int. J. Comput. Vision*, 1(4):321–331, 1988.

T. W. Kee and M. T. Cicerone. Simple approach to one-laser, broadband coherent anti-stokes raman scattering microscopy. *Opt. Lett.*, 29:2701–2703, 2004.

C. Kendall, N. Stone, N. Shepherd, K. Geboes, B. Warren, R. Bennett, and H. Barr. Raman spectroscopy, a potential tool for the objective identification and classification of neoplasia in barrett's oesophagus. *J. Pathol.*, 200:602–609, 2003.

C. Kendall, M. Isabelle, F. Bazant-Hegemark, J. Hutchings, L. Orr, J. Babrah, R. Baker, and N. Stone. Vibrational spectroscopy: a clinical tool for cancer diagnostics. *Analyst*, 134(6): 1029–45, 2009.

I. L. King, T. L. Dickendesher, and B. M. Segal. Circulating Ly-6C+ myeloid precursors migrate to the CNS and play a pathogenic role during autoimmune demyelinating disease. *Blood*, 113(14):3190–3197, Apr. 2009.

K. Knutsen, J. Johnson, A. Miller, P. Petersen, and R. Saykally. High spectral resolution multiplex CARS spectroscopy using chirped pulses. *Chemical Physics Letters*, 387(4-6):436–441, Jan. 2004.

K. P. Knutsen, B. M. Messer, R. M. Onorato, and R. J. Saykally. Chirped coherent anti-stokes Raman scattering for high spectral resolution spectroscopy and chemically selective imaging. *Journal Of Physical Chemistry B*, 110(12):5854–5864, Mar. 2006.

S. Koljenovic, T. C. Bakker Schut, R. Wolthuis, B. de Jong, L. Santos, P. J. Caspers, J. M. Kros, and G. J. Puppels. Tissue characterization using high wave number raman spectroscopy. *J. Biomed. Opt.*, 10(3):031116, 2005a.

S. Koljenovic, T. B. Schut, A. Vincent, J. M. Kros, and G. J. Puppels. Detection of meningioma in dura mater by raman spectroscopy. *Anal. Chem.*, 77(24):7958–7965, 2005b.

L. Kong, M. Ji, G. R. Holtom, D. Fu, C. W. Freudiger, and X. S. Xie. Multicolor stimulated Raman scattering microscopy with a rapidly tunable optical parametric oscillator. *Opt. Lett.*, 38(2):145–147, Jan. 2013.

C. Krafft, S. B. Sobottka, G. Schackert, and R. Salzer. Near infrared raman spectroscopic mapping of native brain tissue and intracranial tumors. *Analyst*, 130(7):1070–1077, 2005.

C. Krafft, A. A. Ramoji, C. Bielecki, N. Vogler, T. Meyer, D. Akimov, P. Rosch, M. Schmitt, B. Dietzek, I. Petersen, A. Stallmach, and J. Popp. A comparative raman and cars imaging study of colon tissue. *J Biophotonics*, 2(5):303–312, 2009a.

C. Krafft, G. Steiner, C. Beleites, and R. Salzer. Disease recognition by infrared and raman spectroscopy. *Journal of Biophotonics*, 2(1-2):13–28, 2009b.

C. Krafft, G. Steiner, C. Beleites, and R. Salzer. Disease recognition by infrared and raman spectroscopy. *J Biophotonics*, 2(1-2):13–28, 2009c.

K. K. Kumar, A. Arland, M. V. P. Chowdary, Keerthi, J. Kurien, C. M. Krishna, and S. Mathew. Discrimination of normal and malignant stomach mucosal tissues by raman spectroscopy: A pilot study. *Vib. Spectrosc.*, 44(2):382–387, 2007.

W. Langbein, I. Rocha-Mendoza, and P. Borri. Single source coherent anti-Stokes Raman microspectroscopy using spectral focusing. *Appl. Phys. Lett.*, 95(8):081109, Jan. 2009.

S. Lankton and A. Tannenbaum. Localizing region-based active contours. *IEEE Trans. Image Processing*, 17(11):2029–2039, Nov. 2008.

T. T. Le, C. W. Rehrer, T. B. Huff, M. B. Nichols, I. G. Camarillo, and J.-X. Cheng. Nonlinear optical imaging to evaluate the impact of obesity on mammary gland and tumor stroma. *Mol. Imaging*, 6(3):205–211, 2007.

T. T. Le, T. B. Huff, and J.-X. Cheng. Coherent anti-stokes raman scattering imaging of lipids in cancer metastasis. *BMC Cancer*, 9(1):42, 2009.

Q. Li, Z. Chen, X. He, Y. Wang, H. Liu, and Q. Xu. Automatic identification and quantitative morphometry of unstained spinal nerve using molecular hyperspectral imaging technology. *Neurochem. Int.*, 61(8):1375–1384, Dec. 2012.

S. Li and T. Chan. Electrical wavelength-tunable actively mode-locked fiber ring laser with a linearly chirped fiber Bragg grating. *IEEE Photon. Technol. Lett.*, 10(6):799–801, June 1998.

H. Liang. Advances in multispectral and hyperspectral imaging for archaeology and art conservation. *Applied Physics A*, 106(2):309–323, 2012.

J. S. Lim. *Two-dimensional signal and image processing*. Prentice Hall, Englewood Cliffs, 1990.

C.-Y. Lin, J. L. Suhalim, C. L. Nien, M. D. Miljkovic, M. Diem, J. V. Jester, and E. O. Potma. Picosecond spectral coherent anti-Stokes Raman scattering imaging with principal component analysis of meibomian glands. *Journal of Biomedical Optics*, 16(2):021104, 2011.

G. Lu and B. Fei. Medical hyperspectral imaging: a review. *Journal of Biomedical Optics*, 19 (1):010901–010901, Jan. 2014.

F. M. Lyng, E. O. Faolain, J. Conroy, A. D. Meade, P. Knief, B. Duffy, M. B. Hunter, J. M. Byrne, P. Kelehan, and H. J. Byrne. Vibrational spectroscopy for cervical cancer pathology, from biochemical analysis to diagnostic tool. *Exp. Mol. Pathol.*, 82(2):121–129, 2007.

P. D. Maker and R. W. Terhune. Study of Optical Effects Due to an Induced Polarization Third Order in the Electric Field Strength. *Phys. Rev.*, 137(3A):801–A818, Feb. 1965.

P. Matteini, F. Ratto, F. Rossi, R. Cicchi, C. Stringari, D. Kapsokalyvas, F. S. Pavone, and R. Pini. Photothermally-induced disordered patterns of corneal collagen revealed by SHG imaging. *Opt. Express*, 17(6):4868–4878, Mar. 2009.

M. A. Matthews. An electron microscopic study of the relationship between axon diameter and the initiation of myelin production in the peripheral nervous system. *Anat. Rec.*, 161 (3):337–351, 1968.

A. Medyukhina, T. Meyer, M. Schmitt, B. F. M. Romeike, B. Dietzek, and J. Popp. Towards automated segmentation of cells and cell nuclei in nonlinear optical microscopy. *J. Biophotonics*, 5(11-12):878–888, Nov. 2012.

A. Medyukhina, T. Meyer, S. Heuke, N. Vogler, B. Dietzek, and J. Popp. Automated seeding-based nuclei segmentation in nonlinear optical microscopy. *Appl. Opt.*, 52(28):6979–6994, Oct. 2013.

E. Meijering. Cell Segmentation: 50 Years Down the Road [Life Sciences]. *IEEE Signal Processing Mag.*, 29(5):140–145, 2012.

P. Mezin, C. Tenaud, J. L. Bosson, and P. Stoebner. Morphometric analysis of the peripheral nerve: advantages of the semi-automated interactive method. *J. Neurosci. Meth.*, 51(2):163–169, Mar. 1994.

E. Mix, H. Meyer-Rienecker, H.-P. Hartung, and U. K. Zettl. Animal models of multiple sclerosis–potentials and limitations. *Prog. Neurobiol.*, 92(3):386–404, Nov. 2010.

H. L. More, J. Chen, E. Gibson, J. M. Donelan, and M. F. Beg. A semi-automated method for identifying and measuring myelinated nerve fibers in scanning electron microscope images. *J. Neurosci. Meth.*, 201(1):149–158, Sept. 2011.

M. Müller and J. M. Schins. Imaging the Thermodynamic State of Lipid Membranes with Multiplex CARS Microscopy. *J. Phys. Chem. B*, 106(14):3715–3723, Apr. 2002.

D. Mumford and J. Shah. Optimal approximations by piecewise smooth functions and associated variational problems. *Comm. Pure Appl. Math.*, 42(5):577–685, 1989.

P. Nandakumar, A. Kovalev, and A. Volkmer. Vibrational imaging based on stimulated raman scattering microscopy. *New Journal of Physics*, 11:033026, 2009.

K.-A. Nave. Myelination and the trophic support of long axons. *Nat. Rev. Neurosci.*, 11(4): 275–283, Apr. 2010.

A. Nijssen, T. C. Bakker Schut, F. Heule, P. J. Caspers, D. P. Hayes, M. H. A. Neumann, and G. J. Puppels. Discriminating basal cell carcinoma from its surrounding tissue by raman spectroscopy. *J. Invest. Dermatol.*, 119(1):64–69, 2002.

M. S. Nixon and A. S. Aguado. *Feature Extraction & Image Processing for Computer Vision*. Academic Press, 3rd edition, 2012.

K. Nose, Y. Ozeki, T. Kishi, K. Sumimura, N. Nishizawa, K. Fukui, Y. Kanematsu, and K. Itoh. Sensitivity enhancement of fiber-laser-based stimulated Raman scattering microscopy by collinear balanced detection technique. *Opt. Express*, 20(13):13958–13965, June 2012.

M. Okuno, H. Kano, P. Leproux, V. Couderc, J. P. R. Day, M. Bonn, and H.-o. Hamaguchi. Quantitative CARS molecular fingerprinting of single living cells with the use of the maximum entropy method. *Angewandte Chemie (International ed. in English)*, 49(38):6773–6777, Sept. 2010.

R. M. Onorato, N. Muraki, K. P. Knutsen, and R. J. Saykally. Chirped coherent anti-stokes raman scattering as a high-spectral- and spatial-resolution microscopy. *Opt. Lett.*, 32:2858–2860, 2007.

S. Osher and J. A. Sethian. Fronts Propagating with Curvature-Dependent Speed: Algorithms Based on Hamilton-Jacobi Formulations. *Journal of Computational Physics*, 79(1): 12–49, Nov. 1988.

Y. Ozeki, F. Dake, S. Kajiyama, K. Fukui, and K. Itoh. Analysis and experimental assessment of the sensitivity of stimulated raman scattering microscopy. *Opt. Express*, 17(5):3651–3658, 2009.

S. H. Parekh, Y. J. Lee, K. A. Aamer, and M. T. Cicerone. Label-free cellular imaging by broadband coherent anti-Stokes Raman scattering microscopy. *Biophysical Journal*, 99(8): 2695–2704, Oct. 2010.

A. F. Pegoraro, A. Ridsdale, D. J. Moffatt, Y. Jia, J. P. Pezacki, and A. Stolow. Optimally chirped multimodal cars microscopy based on a single ti: sapphire oscillator. *Opt. Express*, 17(4):2984–2996, 2009.

R. A. Perley, F. R. Schwab, and A. H. Bridle, editors. *Synthesis imaging in radio astronomy*, volume 6 of *Astronomical Society of the Pacific Conference Series*, 1989.

G. I. Petrov and V. V. Yakovlev. Enhancing red-shifted white-light continuum generation in optical fibers for applications in nonlinear raman microscopy. *Opt. Express*, 13:1299–1306, 2005.

J. P. Pezacki, J. A. Blake, D. C. Danielson, D. C. Kennedy, R. K. Lyn, and R. Singaravelu. Chemical contrast for imaging living systems: molecular vibrations drive CARS microscopy. *Nat. Chem. Biol.*, 7(3):137–145, Mar. 2011.

E. Ploetz, S. Laimgruber, S. Berner, W. Zinth, and P. Gilch. Femtosecond stimulated raman microscopy. *Applied Physics B-Lasers and Optics*, 87(3):389–393, 2007.

T. A. Pologruto, B. L. Sabatini, and K. Svoboda. Scanimage: flexible software for operating laser scanning microscopes. *Biomed. Eng. Online*, 2(1):13, May 2003.

E. O. Potma and X. S. Xie. Detection of single lipid bilayers with coherent anti-stokes raman scattering (cars) microscopy. *J. Raman Spectrosc.*, 34:642–650, 2003.

E. O. Potma, W. P. de Boeij, and D. A. Wiersma. Nonlinear coherent four-wave mixing in optical microscopy. *Journal of the Optical Society of America B-Optical Physics*, 17(10):1678–1684, 2000.

E. O. Potma, D. J. Jones, J.-X. Cheng, X. S. Xie, and J. Ye. High-sensitivity coherent anti-stokes raman scattering microscopy with two tightly synchronized picosecond lasers. *Opt. Lett.*, 27(13):1168–1170, 2002.

S. Preibisch, S. Saalfeld, and P. Tomancak. Globally optimal stitching of tiled 3D microscopic image acquisitions. *Bioinformatics*, 25(11):1463–1465, June 2009.

G. J. Puppels, F. F. M. de Mul, C. Otto, J. Greve, M. Robert-Nicoud, D. J. Arndt-Jovin, and T. M. Jovin. Studying single living cells and chromosomes by confocal Raman microspectroscopy. *Nature*, 347(6290):301–303, 1990.

R. A. Rao, M. R. Mehta, and K. C. Toussaint. Fourier transform-second-harmonic generation imaging of biological tissues. *Opt. Express*, 17(17):14534–14542, 2009.

H. A. Rinia, K. N. J. Burger, M. Bonn, and M. Müller. Quantitative label-free imaging of lipid composition and packing of individual cellular lipid droplets using multiplex cars microscopy. *Biophys. J.*, 95(10):4908–4914, 2008.

A. Robichaux-Viehoever, E. Kanter, H. Shappell, D. Billheimer, H. r. Jones, and A. Mahadevan-Jansen. Characterization of raman spectra measured in vivo for the detection of cervical dysplasia. *Appl. Spectrosc.*, 61(9):986–993, 2007.

I. Rocha-Mendoza, W. Langbein, and P. Borri. Coherent anti-Stokes Raman microspectroscopy using spectral focusing with glass dispersion. *Applied Physics Letters*, 93(20): 201103, Jan. 2008.

E. Romero, O. Cuisenaire, J. F. Denef, J. Delbeke, B. Macq, and C. Veraart. Automatic morphometry of nerve histological sections. *J. Neurosci. Meth.*, 97(2):111–122, Apr. 2000.

P. L. Rosin. Measuring shape: ellipticity, rectangularity, and triangularity. *Mach. Vis. Appl.*, 14(3):172–184, 2003.

M. Ross and W. Pawlina. *Histology*. Lippincott Williams & Wilkins, 2006.

W. A. H. Rushton. A theory of the effects of fibre size in medullated nerve. *J. Physiol.*, 115(1): 101–122, Sept. 1951.

A. Savitzky and M. J. Golay. Smoothing and differentiation of data by simplified least squares procedures. *Anal. Chem.*, 36(8):1627–1639, 1964.

R. Selm, M. Winterhalder, A. Zumbusch, G. Krauss, T. Hanke, A. Sell, and A. Leitenstorfer. Ultrabroadband background-free coherent anti-stokes raman scattering microscopy based on a compact er:fiber laser system. *Opt. Lett.*, 35(19):3282–4, 2010.

J. A. Sethian. *Level Set Methods & Fast Marching Methods : Evolving Interfaces in Computational Geometry, Fluid Mechanics, Computer Vision, and Materials Science*. Cambridge University Press, 1999.

M. Sezgin and B. Sankur. Survey over image thresholding techniques and quantitative performance evaluation. *Journal of Electronic Imaging*, 13(1):146–165, Jan. 2004.

K. E. Shafer-Peltier, A. S. Haka, M. Fitzmaurice, J. Crowe, J. Myles, R. R. Dasari, and M. S. Feld. Raman microspectroscopic model of human breast tissue: implications for breast cancer diagnosis in vivo. *J. Raman Spectrosc.*, 33(7):552–563, 2002.

G. Shetty, C. Kendall, N. Shepherd, N. Stone, and H. Barr. Raman spectroscopy: elucidation of biochemical changes in carcinogenesis of oesophagus. *Brit J Cancer*, 94:1460–1464, 2006.

Y. Shi, D. Zhang, T. B. Huff, X. Wang, R. Shi, X.-M. Xu, and J.-X. Cheng. Longitudinal in vivo coherent anti-Stokes Raman scattering imaging of demyelination and remyelination in injured spinal cord. *J. Biomed. Opt.*, 16(10):106012, Oct. 2011.

M. N. Slipchenko, T. T. Le, H. Chen, and J.-X. Cheng. High-Speed Vibrational Imaging and Spectral Analysis of Lipid Bodies by Compound Raman Microscopy. *J. Phys. Chem. B*, 113 (21):7681–7686, 2009.

N. Stone, M. C. H. Prieto, P. Crow, J. Uff, and A. W. Ritchie. The use of raman spectroscopy to provide an estimation of the gross biochemistry associated with urological pathologies. *Anal. Bioanal. Chem.*, 387(5):1657–1668, 2007.

J. S. Suri, K. Liu, S. Singh, S. N. Laxminarayan, X. Zeng, and L. Reden. Shape recovery algorithms using level sets in 2-D/3-D medical imagery: a state-of-the-art review. *IEEE Trans. Inf. Technol. Biomed.*, 6(1):8–28, Mar. 2002.

B. A. 't Hart, B. Gran, and R. Weissert. EAE: imperfect but useful models of multiple sclerosis. *Trends Mol. Med.*, 17(3):119–125, Mar. 2011.

W. M. Tolles, J. W. Nibler, J. R. Mc Donald, and A. B. Harvey. A Review of the Theory and Application of Coherent anti-stokes raman spectroscopy (CARS). *Appl. Spectrosc.*, 31(4): 253–271, Jan. 1977a.

W. M. Tolles, J. W. Nibler, J. R. McDonald, and A. B. Harvey. Review of theory and application of coherent anti-stokes raman spectroscopy (cars). *Appl. Spectrosc.*, 31:253–271, 1977b.

V. Tuchin. *Tissue optics: light scattering methods and instruments for medical diagnosis*. SPIE Press, 2 edition, 2007.

S. Uchida. Image processing and recognition for biological images. *Dev. Growth. Differ.*, 55 (4):523–549, May 2013.

F. Urso-Baiarda and A. O. Grobbelaar. Practical nerve morphometry. *J. Neurosci. Meth.*, 156 (1-2):333–341, Sept. 2006.

Y. Usson, S. Torch, and R. Saxod. Morphometry of human nerve biopsies by means of automated cytometry: assessment with reference to ultrastructural analysis. *Anal. Cell. Pathol.*, 3(2):91–102, Mar. 1991.

P. van der Valk and S. Amor. Preactive lesions in multiple sclerosis. *Curr. Opin. Neurol.*, 22 (3):207–213, June 2009.

H.-J. van Manen, Y. M. Kraan, D. Roos, and C. Otto. Single-cell Raman and fluorescence microscopy reveal the association of lipid bodies with phagosomes in leukocytes. *Proc. Natl. Acad. Sci.*, 102(29):10159–10164, July 2005.

E. M. Vartiainen, H. A. Rinia, M. Müller, and M. Bonn. Direct extraction of raman line-shapes from congested cars spectra. *Opt. Express*, 14(8):3622–3630, 2006.

I. Veilleux, J. A. Spencer, D. P. Biss, D. C. Côté, and C. P. Lin. In vivo cell tracking with video rate multimodality laser scanning microscopy. *IEEE J. Select. Topics Quantum Electron.*, 14 (1):10–18, 2008.

L. Vincent. Minimal path algorithms for the robust detection of linear features in gray images . In *Proceedings of the Fourth International Symposium on Mathematical Morphology and Its Applications to Image and Signal Processing*, ISMM '98, pages 331–338. Kluwer Academic Publishers, 1998.

A. Volkmer, J.-X. Cheng, and X. S. Xie. Vibrational imaging with high sensitivity via epidetected coherent anti-stokes raman scattering microscopy. *Phys. Rev. Lett.*, 87:023901, 2001.

A. Volkmer, L. D. Book, and X. S. Xie. Time-resolved coherent anti-stokes raman scattering microscopy: Imaging based on raman free induction decay. *Appl. Phys. Lett.*, 80(9):1505–1507, 2002.

H. Wang. Coherent anti-stokes raman scattering imaging of axonal myelin in live spinal tissues. *Biophys. J.*, 89:581–591, 2005.

H. Wang, Y. Fu, P. Zickmund, R. Shi, and J.-X. Cheng. Coherent Anti-Stokes Raman Scattering Imaging of Axonal Myelin in Live Spinal Tissues. *Biophys. J.*, 89(1):581–591, July 2005.

K. Wang, C. W. Freudiger, J. H. Lee, B. G. Saar, X. S. Xie, and C. Xu. Synchronized time-lens source for coherent Raman scattering microscopy. *Opt. Express*, 18(23):24019–24024, Jan. 2010.

Y.-Y. Wang, Y.-N. Sun, C.-C. K. Lin, and M.-S. Ju. Segmentation of nerve fibers using multi-level gradient watershed and fuzzy systems. *Artif. Intell. Med.*, 54(3):189–200, Mar. 2012.

B. Weyn, M. van Remoortere, R. Nuydens, T. Meert, and G. van de Wouwer. A multiparametric assay for quantitative nerve regeneration evaluation. *J. Microsc.*, 219(Pt 2):95–101, Aug. 2005.

R. T. Whitaker. A Level-Set Approach to 3D Reconstruction from Range Data. *Int. J. Comput. Vision*, 29(3):203–231, 1998.

X. Zhao, Z. Pan, J. Wu, G. Zhou, and Y. Zeng. Automatic identification and morphometry of optic nerve fibers in electron microscopy images. *Comput. Med. Imag. Grap.*, 34(3):179–184, Apr. 2010.

I. R. Zimmerman, J. L. Karnes, P. C. O'Brien, and P. J. Dyck. Imaging system for nerve and fiber tract morphometry: components, approaches, performance, and results. *J. Neuropath. Exp. Neur.*, 39(4):409–419, July 1980.

T. Zimmermann, J. Rietdorf, and R. Pepperkok. Spectral imaging and its applications in live cell microscopy. *FEBS Letters*, 546(1):87–92, July 2003.

K. Zuiderveld. Contrast limited adaptive histogram equalization. In P. S. Heckbert, editor, *Graphics Gems IV*, pages 474–485. Academic Press Professional, Inc., 1994.

A. Zumbusch, G. R. Holtom, and X. S. Xie. Three-dimensional vibrational imaging by coherent anti-Stokes Raman scattering. *Phys. Rev. Lett.*, 82(20):4142–4145, Jan. 1999a.

A. Zumbusch, G. R. Holtom, and X. S. Xie. Three-dimensional vibrational imaging by coherent anti-stokes raman scattering. *Phys. Rev. Lett.*, 82:4142–4145, 1999b.